

Kristoffersen, Aksel

# Guidance and Control System for Dynamic Positioning and Path Following of an AUV exposed to Ocean Currents

Masteroppgave i Cybernetics and Robotics

Veileder: Fossen, Thor Inge

Juni 2021



Kristoffersen, Aksel

# **Guidance and Control System for Dynamic Positioning and Path Following of an AUV exposed to Ocean Currents**

Masteroppgave i Cybernetics and Robotics  
Veileder: Fossen, Thor Inge  
Juni 2021

Norges teknisk-naturvitenskapelige universitet  
Fakultet for informasjonsteknologi og elektroteknikk  
Institutt for teknisk kybernetikk



Kunnskap for en bedre verden



# Abstract

Fully actuated AUVs have the potential of performing unmanned underwater tasks and dynamic positioning and path following are both essential scenarios to master in order to achieve close range inspection and intervention tasks.

Models of AUVs have been studied, and this thesis present a guidance and control systems in which design parameters are highly dependent on the model parameters. However, the exposure of unknown ocean currents makes high precision maneuvering and navigation a challenging task. This thesis therefore presents a novel current estimator method using the hydrodynamic model of the vehicle, steady-state evaluation of the control forces and changes in its orientation, to estimate the ocean current velocity and angle. The estimator is verified by computer simulations, and the resulting estimates are able to exclude non-current modelling errors by assuming they are constant in body during steady state sampling.

In addition a novel 3D path following controller is proposed which optimizes the motion of a virtual target by using a control law from the reference model point of view. The control law includes vehicle and actuator constraints, and optimization techniques are then used to maximize the along-track speed of the virtual target. The resulting design parameters of the controller are able to advocate for the desired balance between path following precision versus speed. Finally the guidance and control system, including the path-following controller, is verified by computer simulations which includes ocean currents, and structural and parametric disturbances.



# Sammendrag

Fullt aktiverte AUV-er har potensialet til å utføre ubemannede undervannsoppdrag, og dynamisk posisjonering og stifølgning er begge viktige scenarier å mestre for å oppnå inspeksjons- og intervensjonsoppgaver på nært hold.

Modeller av AUV-er er studert, og denne avhandlingen presenterer et veilednings- og kontrollsystem der designparametere er svært avhengige av modellparametrene. Imidlertid gjør eksponering av ukjente havstrømmer manøvrering og navigering med høy presisjon til en utfordrende oppgave. Denne oppgaven presenterer derfor en ny strømestimator metode som bruker den hydrodynamiske modellen til kjøretøyet, steady-state evaluering av kontrollkreftene og endringer i orienteringen, for å estimere havets strømhastighet og vinkel. Estimatoren bekreftes av datasimuleringer, og de resulterende estimatene er i stand til å ekskludere modelleringsfeil som ikke stammer fra effekter fra havstrømmene, ved å anta at de er konstante i kroppsrammen under prøvetaking i estimeringen.

I tillegg foreslås en ny 3D-stifølgingskontroller som optimaliserer bevegelsen til et virtuelt mål ved å bruke en kontrolllov fra referansemiddellets synspunkt. Kontrollloven inkluderer kjøretøy- og aktuatorbegrensninger, og optimaliseringsteknikker blir deretter brukt for å maksimere hastigheten på det virtuelle målet. De resulterende designparametrene til kontrolleren er i stand til å designe balansen mellom presisjon på banefølgningen versus hastighet. Til slutt blir veilednings- og kontrollsystemet, inkludert stifølgingskontrolleren, bekreftet av datasimuleringer som inkluderer havstrømmer og strukturelle og parametriske forstyrrelser.





# Acknowledgements

I would like to express gratitude towards my supervisor, Professor Thor Inge Fossen, for informative discussions and guidance throughout the project period, as well as for his extensive contributions in much of the theoretical groundwork this thesis is based upon. I would also like to thank my family for their everlasting support during these strange times of this pandemic.

A.K



# Contents

<b>Abstract</b> . . . . .	<b>iii</b>
<b>Sammendrag</b> . . . . .	<b>v</b>
<b>Acknowledgements</b> . . . . .	<b>vii</b>
<b>Contents</b> . . . . .	<b>ix</b>
<b>Figures</b> . . . . .	<b>xi</b>
<b>Tables</b> . . . . .	<b>xiii</b>
<b>1 Introduction</b> . . . . .	<b>1</b>
1.1 Background and Literature Review . . . . .	1
1.1.1 Motion control system architecture . . . . .	1
1.1.2 Dynamic-positioning control and ocean current estimation . . . . .	2
1.1.3 Path-following control for low-speed maneuvering . . . . .	3
1.2 Main Contributions . . . . .	4
1.3 Thesis Outline . . . . .	5
<b>2 Preliminaries</b> . . . . .	<b>7</b>
2.1 Reference Frames . . . . .	7
2.2 Rotation Matrices . . . . .	7
2.3 Path Tangents and Curvature . . . . .	8
<b>3 Mathematical Modelling of Underwater Vehicles</b> . . . . .	<b>11</b>
3.1 Underwater Vehicle Dynamics . . . . .	11
3.1.1 Kinematics . . . . .	12
3.1.2 Kinetics . . . . .	14
3.2 Simplified Low-speed Maneuvering Model . . . . .	17
3.3 Thruster Dynamics . . . . .	21
3.3.1 Case study: Modelling the low-level actuator control system for the T200 thrusters . . . . .	22
<b>4 Simulation Testbed and Software</b> . . . . .	<b>27</b>
4.1 Robot Operating System (ROS) . . . . .	27
4.2 The UUV Simulator . . . . .	28
4.3 Navigation System . . . . .	29
4.4 Beluga NTNU . . . . .	30
<b>5 Control System</b> . . . . .	<b>31</b>
5.1 Control Allocation . . . . .	32

5.1.1	Case study: Modelling the control allocation system for Beluga NTNU	33
5.1.2	Control force error optimization	35
5.1.3	Case study: Optimizing the control force error for Beluga NTNU	39
5.2	Motion Control	39
5.2.1	SISO PID pole-placement algorithm	40
5.2.2	Dynamic-positioning control	42
5.3	Horizontal Ocean Current Estimator	44
5.4	Case Study: Simulation of the Control System and Current Estimator using Beluga NTNU	48
<b>6</b>	<b>Guidance System</b>	<b>55</b>
6.1	Reference Model	55
6.1.1	Reference model dynamics	56
6.1.2	Case Study: Trajectory generation and tracking using Beluga NTNU	58
6.2	3D Path Following	59
6.2.1	Path definitions	61
6.2.2	Path representations	62
6.2.3	Path-following control based on controlling a virtual target	65
6.2.4	Case Study: 3D path following using Beluga NTNU	71
<b>7</b>	<b>Case Study: Simulation of the Guidance and Control System</b>	<b>77</b>
7.1	Simulation Setup and Parameters	77
7.2	Simulation Results	80
7.3	Conclusion of Case Study	82
<b>8</b>	<b>Conclusions and Recommendation for Further Work</b>	<b>83</b>
8.1	Conclusions	83
8.2	Recommendations for Further Work	84
	<b>Bibliography</b>	<b>87</b>
<b>A</b>	<b>Beluga NTNU Parameters</b>	<b>91</b>
<b>B</b>	<b>Model Parametric Differences for the Case Study in Section 7</b>	<b>93</b>
<b>C</b>	<b>Master's Thesis Project Description</b>	<b>95</b>

# Figures

1.1	The GNC motion control system architecture . . . . .	2
2.1	Illustration of the a path-tangential angle . . . . .	8
2.2	Change in path-tangential angle for a circular path . . . . .	9
3.1	The NED frame and the body-fixed frame . . . . .	12
3.2	Low-level actuator control . . . . .	22
3.3	Illustration of the thruster frames $\{p_i\}$ . . . . .	22
3.4	Curve fit on the performance data for the T200 Thruster . . . . .	24
3.5	A low-level actuator control system for thrusters . . . . .	25
4.1	Illustration of the integration of the simulation testbed . . . . .	27
4.2	The visual model of Beluga NTNU in Gazebo . . . . .	30
5.1	Illustration of the Control System . . . . .	31
5.2	Control allocation when saturation on the control inputs are active . . . . .	36
5.3	Control allocation by optimizing the control force error . . . . .	40
5.4	PID control of a second-order linear system . . . . .	41
5.5	Illustration of different values of $f(\Delta\psi)$ . . . . .	48
5.6	Illustration of the ocean current estimator implementation . . . . .	48
5.7	Illustration of the step change in the desired pose $\eta_d$ . . . . .	50
5.8	Step response under the influence of unknown ocean currents . . . . .	51
5.9	Current estimation using different values of $\Delta\psi$ . . . . .	52
5.10	Step response using ocean current feed-forward control . . . . .	53
6.1	Illustration of the guidance system . . . . .	55
6.2	Trajectory generation using the reference model . . . . .	59
6.3	Trajectory tracking using ocean current and reference feed-forward control . . . . .	60
6.4	Path consisting of only straight lines . . . . .	63
6.5	Path consisting of straight lines and curved arcs . . . . .	64
6.6	Illustration of the virtual target reference frame . . . . .	65
6.7	Illustration of two different choices of heading angle for the virtual target . . . . .	66

6.8	Illustration of how to find the time derivative of a heading angle guided by a point in the horizontal plane . . . . .	68
6.9	Illustration of the path following mission . . . . .	72
6.10	$G^0$ path following using $\omega_b = [1.0, 1.0, 1.0, 0.0, 0.0, 2.0]$ . . . . .	74
6.11	$G^0$ path following using $\omega_b = [0.5, 0.5, 0.5, 0.0, 0.0, 1.0]$ . . . . .	75
6.12	$G^1$ path following result using $\omega_b = [0.5, 0.5, 0.5, 0.0, 0.0, 1.0]$ . . . . .	76
7.1	Illustration of the final guidance and control system architecture . . . . .	77
7.2	The resulting ocean current estimates . . . . .	81
7.3	The resulting path following performance . . . . .	81

# Tables

2.1	Overview of the different reference frames . . . . .	7
4.1	Parameters required for the UUV Simulator thruster plugin . . . . .	28
4.2	Parameters required UUV Simulator vehicle dynamics . . . . .	29
4.3	The state estimates which is assumed available for the guidance and control system . . . . .	30
5.1	Numerical values for the locations of the thrusters for Beluga NTNU	34
7.1	The parameters of the UUV Simulator . . . . .	78
7.2	The design parameters of control allocation system . . . . .	78
7.3	The design parameters of the motion control system . . . . .	79
7.4	The design parameters of the current estimator . . . . .	79
7.5	The design parameters of the reference model . . . . .	79
7.6	The design parameters of the path-following controller . . . . .	80
A.1	Beluga NTNU thruster locations . . . . .	92
B.1	Representation of model parametric differences . . . . .	93
B.2	Parametric differences in the Beluga NTNU thruster locations . . . . .	94





# Chapter 1

## Introduction

### 1.1 Background and Literature Review

Autonomous underwater vehicles have for the last decades grasped the attention of researchers for their potential of performing unmanned labor in marine environments. Recent gain in computing power, control methods, navigation and sensor systems have led to AUVs being associated with operations such as exploration, data collection [1], intervention tasks [2], environmental inspection and surveillance. Mathematical models of underwater vehicle have been studied [3], and a couple of model properties are worth taking notice of before considering the motion control aspects. Torpedo-shaped AUVs holds a large share of the AUV market as they offer a good balance between speed and stability. They are often equipped with a main propeller, control surfaces [4], and sometimes transverse tunnel thrusters to achieve the desired degree of actuation. However transverse tunnel thrusters lose their efficiency at high speeds [5], whereas control surfaces lose efficiency in low speeds. Therefore motion control systems for underwater vehicles are often designed according to maneuvering speeds. This thesis will mainly emphasize the fully-actuated case using thrusters in the regime of low-speed maneuvering.

#### 1.1.1 Motion control system architecture

Before introducing the conventional motion control system architecture for AUVs, it is useful to distinguish between three different motion control scenarios. The simplest form is setpoint regulation where the control targets are constant. The second scenario is trajectory tracking where the control targets are varying and time dependent. The third control scenario considered is path following, where the control targets are a predefined path of positional configurations invariant of time. Here the control objective is to converge to and follow the path.

Motion control system for AUVs can become very complex, and it is possible to

construct an advanced and tightly coupled end-to-end system. However this approach can be impractical when software modules increase in complexity or have strong dependencies, making the system less modular. It is therefore useful to simplify the process of software development and maintenance by dividing the system into subsystems. Consequently this thesis will adopt the guidance, navigation and control (GNC) system as in [3]. The typical information flow of the GNC system is illustrated in Figure 1.1.

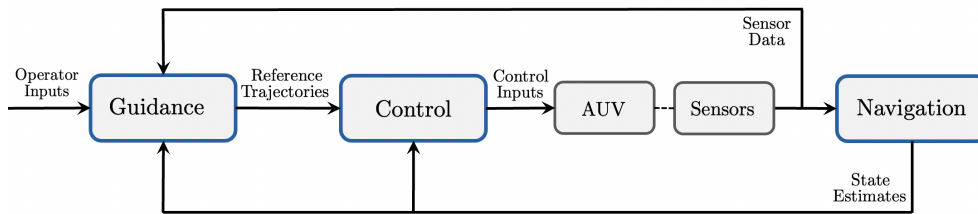


**Figure 1.1:** The GNC motion control system architecture

**Navigation System:** The objective of the navigation systems is to determine the state estimates of the vehicle. The absence of Global Navigation Satellite Systems (GNSS) makes underwater navigation a challenging task, and navigation methods are typically divided into three categories. There are dead-reckoning and inertial navigation, acoustic navigation and geophysical navigation [6]. This thesis will not go in depth regarding the navigation system, however some assumptions will be made for what state estimates are available for feedback control.

**Control System:** The control system is to determine the control inputs for the control plant. The control objectives is usually limited to trajectory tracking and/or setpoint regulation. The control system is often divided into a cascaded structure of a motion control system for determining the desired control forces and a control allocation system to determine the control inputs. A low-level actuator control system for regulating the states of the actuators can also include in this category [7].

**Guidance System:** The guidance system represents a basic methodology concerned with the transient motion behavior associated with the achievement of motion control objectives [8]. Put in simpler terms the guidance system for this thesis is to generate trajectory references to be used in the underlying control system. The guidance system can be divided into subsystems for path planning, obstacle avoidance, guidance control and reference models.

### 1.1.2 Dynamic-positioning control and ocean current estimation

Dynamic Positioning (DP) is the action of maintaining a marine craft in a fixed position or on a pre-determined track exclusively by means of active thrusters.

In regards to the control system, the presumably simplest and well documented method is using a multivariable-PID controller in cascade with a control allocation system [9]. This is also typically regarded as the industry standard for feed-back control for DP. Also more complex controllers have been studied to counter significant non-linearities and disturbances in the marine environment. However for underwater vehicles in the regime of low-speed maneuvering, the dynamics of the system can often be justified as a set of linear equations [3], apposed to high-speed maneuvering models. Also environmental disturbances are often reduced to constant irrotational ocean currents for underwater vehicles, apposed additional wave and wind induced disturbances for surface vehicles. Hence, a multivariable-PID controller, cascaded with a reference model to create the desired reference trajectories, is expected to perform well for low-speed maneuvering of a fully-actuated AUV.

The integral action of the PID controllers aims at compensating for unmodelled dynamics, including the unknown ocean currents. The integral action is typically designed with slow dynamics, hence motion control can presumably be improved if current estimates can be included as feed-forward terms. Estimating the current is however difficult without also unwillingly including the additional non-current unmodelled dynamics in the estimates. However, this thesis proposes that it should be possible to solely use the steady-state integral terms, and the hydrodynamic parameters of the vehicle, to successfully estimate the velocity of a constant irrotational ocean current. To the notion of this thesis this has not been accomplished in previous work. Since ocean current measurements are considered important for other tasks such as navigation optimal path planning and motion control itself [10], the first research question of this thesis is the following.

- R1** Is it possible to use steady-state integral action terms, and changes in the orientation of the vehicle, to estimate the ocean current velocity invariant of additional non-current modelling errors.

### 1.1.3 Path-following control for low-speed maneuvering

So far the two maneuvering scenarios of station keeping and low-speed maneuvering can proposedly be solved using setpoint regulation, trajectory tracking and the cascaded structure of a reference model and a control system. However when the vehicle is to follow a longer distance path, for instance when performing an inspection mission, it can be inconvenient to purely rely on trajectory tracking. Error dynamics are likely to occur along the path, and the objective of trajectory tracking can quickly become infeasible, or poorly defined in regards to successfully completing the mission. Therefore the motion-control scenario of path following is often used for tracking of longer paths when the precision is of higher priority than the time span of the mission. The path following objective is typically solved by applying a guidance controller to provide reference signals to a underly-

ing reference model or control system. Path-following control for marine vehicles have been presented in [11] and [12], where the methods is based on driving the vehicle onto the path by guiding its heading angle. However for low-speed maneuvering of fully actuated AUVs, actuation in sway is also available. Another popular method is to define a virtual target to propagate along the path [13] to guide the vehicles onto the path. Typical challenges have been addressed as reducing the parameter complexity and including vehicle dynamical limitations in the path-following control design. It is also desired that the path following performance is satisfactory even for paths that are generated without taking the dynamical limitations of the vehicle into consideration. Hence the second research question of this thesis is the following.

- R2** Is it possible to develop a 3D path-following controller to include dynamical constraints for a specific underwater vehicle, as well as to include tuning parameters to advocate for different path following behaviors accordingly.

For a guidance and control system it can often be difficult and time consuming to find the initial set of tuning parameters that give a satisfactory response for a specific vehicle. Different vehicles have different dynamical models and actuator configurations. However, the models are often developed regardless for simulation purposes, and it can therefore be convenient to base the parameters of the guidance and control system on the conventional model. This will increase the modularity and flexibility of the system when applying it on different vehicles or when changing the configuration of a vehicle. It can therefore be convenient if the tuning parameters of the system is either quite intuitive or universal, for instance by basing the parameters on conventional model and actuator parameters of the vehicle. Consequently, the third and final research question, is related to the entirety of the guidance and control system architecture.

- R3** Is it possible to develop a guidance and control system where all parameters of the system have intuitive or universal properties, such as using the model parameters of the specific underwater vehicle.

## 1.2 Main Contributions

The main contributions of this thesis have emphasis on low-speed maneuvering of fully-actuated AUVs using thrusters as actuators, and are as follows:

- Introduction and modelling of a low-level actuator control system for thrusters.
- Introduction and modelling of a control allocation system for an AUV using body-fixed thrusters.
- Development of a control allocation module to optimize control forces when exposed to saturation on the control inputs.
- Development of a multivariable-PID controller for dynamic positioning, us-

ing PID-pole placement and including reference and ocean current feed-forward control.

- Development of a novel ocean current estimator using samples of the DP controller steady-state integral action terms, the hydrodynamic model parameters of the vehicle and changes in heading angle, to estimate the constant irrotational ocean currents parameters in the horizontal plane.
- Development of a low-speed maneuvering reference model to include current estimates and actuator limitations.
- Development of a novel 3D path-following guidance controller to include parameters for choosing between path-following precision and speed. The controller also includes vehicle dynamical and actuator limitations, and includes the option of path tangential or 2D point based heading guidance. Hence giving the path-following controller 4 DOFs.
- Verification of the guidance and control system by computer simulation including structural and parametric disturbances.

### 1.3 Thesis Outline

In Section 2 a couple of preliminaries are presented. In Section 3 the conventional method of modelling the dynamics of an underwater vehicle is introduced. This section results in a simplified low-speed maneuvering model and low-level actuator system to be included in the design of the guidance and control system. In Section 4 the simulation testbed and software used in various experiments are introduced. In Section 5 the different modules of the control system are described, modelled and tested. Here the current estimation method is also accounted for and tested in simulations. In Section 6 the reference model and path-following controller is developed and tested. In Section 7 the overall guidance and control system is verified by computer simulations including parametric and structural disturbances. Finally in Section 8 concluding remarks are made and recommendations for further work are given.



## Chapter 2

# Preliminaries

### 2.1 Reference Frames

Table 2.1 gives an overview of the different reference frames used throughout the thesis.

Table 2.1: Overview of the different reference frames

Notation	Description
$\{n\}$	Earth-fixed North East Down (NED) frame
$\{b\}$	Body-fixed vehicle frame
$\{p_i\}$	Actuator frames $i \in \{1, 2, \dots, r\}$
$\{m\}$	Reference model frame
$\{p\}$	Path tangent frame
$\{t\}$	Virtual target frame

### 2.2 Rotation Matrices

A rotation matrix a transformation matrix that is used to perform a rotation in the Euclidean space. The roll, pitch and yaw rotation is a popular way of representing an orientation of frame  $\{j\}$ , relative to frame  $\{i\}$ , in the 3D Euclidean space. The rotation consists of a matrix multiplication of three following rotations in the following order

$$\mathbf{R}(\Theta_{ij}) = \underbrace{\begin{bmatrix} \cos \psi & -\sin \psi & 0 \\ \sin \psi & \cos \psi & 0 \\ 0 & 0 & 1 \end{bmatrix}}_{R_z(\psi)} \underbrace{\begin{bmatrix} \cos \theta & 0 & \sin \theta \\ 0 & 1 & 0 \\ -\sin \theta & 0 & \cos \theta \end{bmatrix}}_{R_y(\theta)} \underbrace{\begin{bmatrix} 1 & 0 & 0 \\ 0 & \cos \phi & -\sin \phi \\ 0 & \sin \phi & \cos \phi \end{bmatrix}}_{R_x(\phi)} \quad (2.1)$$

consequently

$$\mathbf{R}(\Theta_{ij}) = \begin{bmatrix} c\psi c\theta & -s\psi c\phi + c\psi s\theta s\phi & s\psi s\phi + c\psi c\phi s\theta \\ s\psi c\theta & c\psi c\phi + s\phi s\theta s\psi & -c\psi s\phi + s\theta s\psi c\phi \\ -s\theta & c\theta s\phi & c\theta c\phi \end{bmatrix} \quad (2.2)$$

where  $\Theta_{ij} = [\phi, \theta, \psi]^\top$  is the Euler angles.

**Using unit-quaternions:**

$$\mathbf{R}(\mathbf{q}_j^i) := \mathbf{I}_3 + 2\eta\mathbf{S}(\boldsymbol{\varepsilon}) + 2\mathbf{S}^2(\boldsymbol{\varepsilon}) \quad (2.3)$$

where

$\mathbf{q}_j^i = [\eta, \varepsilon_1, \varepsilon_2, \varepsilon_3]^\top$  is the unit-quaternion orientation of frame  $j$  relative to  $i$ .  
 $\mathbf{I}_3$  is the  $3 \times 3$  identity matrix.

$\mathbf{S}(\cdot)$  is the skew-symmetric matrix.

$\boldsymbol{\varepsilon} = [\varepsilon_1, \varepsilon_2, \varepsilon_3]^\top$  is the complex part of the unit quaternion.

The rotation matrices are considered orthogonal matrices since they have the following properties

$$\mathbf{R}^{-1} = \mathbf{R}^\top, \quad \det \mathbf{R} = \pm 1 \quad (2.4)$$

## 2.3 Path Tangents and Curvature

Path-tangential angles is the angle defined by the tangent of a point on a path relative to an inertial reference frame as illustrated in Figure 2.1.

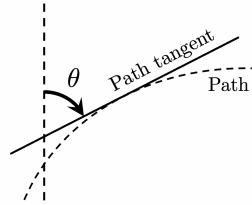


**Figure 2.1:** Illustration of the a path-tangential angle

This will later be used to find the path-tangential angular velocity for a given path curvature and a given along-track speed. This relationship can be found by first look at the circular path example in Figure 2.2.

Here it can be seen that a change in a the path-tangential angle can be expressed as a function of change in arc length and the radius as such

$$\Delta\theta = \frac{1}{R}\Delta s \quad (2.5)$$



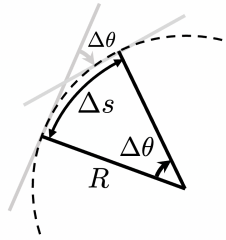


**Figure 2.2:** Change in path-tangential angle for a circular path

By making the system time variant, dividing by  $\Delta t$  on both sides, and introducing the curvature as ( $\kappa = 1/R$ ), one gets

$$\frac{\Delta\theta(t)}{\Delta t} = \kappa \frac{\Delta s(t)}{\Delta t} \quad (2.6)$$

further taking the limit as times goes to zero gives

$$\lim_{t \rightarrow 0} \frac{\Delta\theta(t)}{\Delta t} = \lim_{t \rightarrow 0} \kappa \frac{\Delta s(t)}{\Delta t} \quad (2.7)$$

$$\dot{\theta} = \kappa \dot{s} \quad (2.8)$$

**Remark 1** *In this thesis the sign of the along track speed will be determined by whether the speed yields forward propagation along the path, and the change in angle will be determined by the using the Euler axis. Consequently, in cases where a positive along track speeds yields a negative change in the path-tangential angle the curvature will to be defined as negative when using (2.8).*



## Chapter 3

# Mathematical Modelling of Underwater Vehicles

The research on mathematical modelling of marine crafts have been extensive, and models for the purpose of GNC system design and simulations have proven to be highly useful. Therefore this chapter is dedicated to understand some of the different aspects of this field to be able to apply it in the guidance and control system design. Section 3.1 gives an introduction to the conventional way of modelling the dynamics of underwater vehicles exposed to ocean currents based on [3]. Thereafter a low-speed maneuvering model is derived in Section 3.2, before a low-level actuator control system is modelled in Section 3.3, both to be included in the simulation testbed and in the design of the guidance and control systems described later in this thesis.

### 3.1 Underwater Vehicle Dynamics

The dynamics of underwater vehicles can be parameterized as follows [3]

$$\dot{\boldsymbol{\eta}} = \mathbf{J}_k(\boldsymbol{\eta})(\boldsymbol{v}_r + \boldsymbol{v}_c) \quad (3.1)$$

$$\mathbf{M} \dot{\boldsymbol{v}}_r + \mathbf{C}(\boldsymbol{v}_r) \boldsymbol{v}_r + \mathbf{D}(\boldsymbol{v}_r) \boldsymbol{v}_r + \mathbf{g}(\boldsymbol{\eta}) = \boldsymbol{\tau} \quad (3.2)$$

where

$\boldsymbol{v}_c = [u_c, v_c, w_c, 0, 0, 0]^\top$  is the constant irrotational current velocity vector.  
 $k \in \{\theta, q\}$  denote the Euler angle or unit quaternion representation.

$$\mathbf{M} = \mathbf{M}_{RB} + \mathbf{M}_A \quad (3.3)$$

$$\mathbf{C}(\boldsymbol{v}_r) = \mathbf{C}_{RB}(\boldsymbol{v}_r) + \mathbf{C}_A(\boldsymbol{v}_r) \quad (3.4)$$

$$\mathbf{D}(\boldsymbol{v}_r) = \mathbf{D} + \mathbf{D}_n(\boldsymbol{v}_r) \quad (3.5)$$

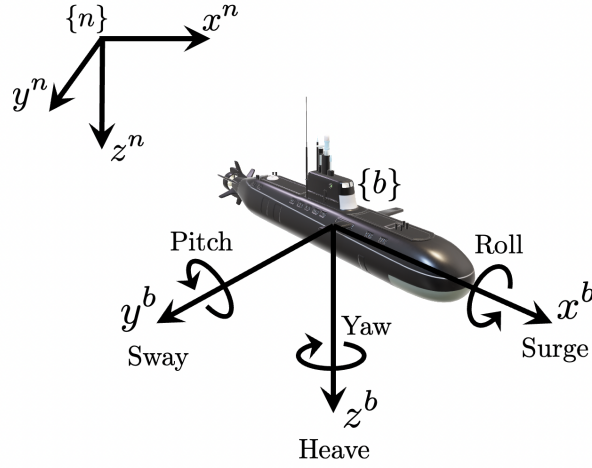


Figure 3.1: Illustration of the NED frame  $\{n\}$ , and the body-fixed frame  $\{b\}$ .

### 3.1.1 Kinematics

#### Reference frames

The motion of the vehicle is described in relation to reference frames. Since AUVs typically operate in small to medium scale operations [14], typically less than 10 km radius, it is convenient to consider local navigation. This means that the inertial reference frame can be decided to coincide with the earth-fixed north east down (NED)-frame. The second frame to be considered is the BODY-fixed frame of the vehicle. Figure 3.1 gives an illustration of these two reference frames.

#### Position and orientation vector

The position of the vehicle ( $CO$ ) is expressed with respect to  $\{n\}$ . The orientation of the vehicle can be expressed as the rotation needed for  $\{n\}$  to coincide with  $\{b\}$ . The most popular representations of the axis angle are unit quaternions and Euler angles. Unit quaternions have the benefits of avoiding singularities and improved numerical stability. Euler angles on the other hand are often preferred when singularities can be avoided and mathematical simplicity is favoured. Consequently, the position and orientation of the vehicle will be defined as follows

$$\text{Using Euler angles: } \boldsymbol{\eta} = \begin{bmatrix} \mathbf{p}_{nb}^n \\ \boldsymbol{\Theta}_{nb} \end{bmatrix} = [x^n, y^n, z^n, \phi, \theta, \psi]^\top \quad (3.6)$$

$$\text{Using unit quaternions: } \boldsymbol{\eta} = \begin{bmatrix} \mathbf{p}_{nb}^n \\ \mathbf{q}_b^n \end{bmatrix} = [x^n, y^n, z^n, \eta, \varepsilon_1, \varepsilon_2, \varepsilon_3]^\top \quad (3.7)$$

where

$\mathbf{p}_{nb}^n = [x^n, y^n, z^n]^\top$  is the position of  $CO$  relative to  $o^n$  expressed in  $\{n\}$ .

$\Theta_{nb} = [\phi, \theta, \psi]^\top$  is the Euler angles of  $\{b\}$  w.r.t.  $\{n\}$ .  
 $\mathbf{q}_b^n = [\eta, \varepsilon_1, \varepsilon_2, \varepsilon_3]^\top$  is the unit quaternions of  $\{b\}$  w.r.t. to  $\{n\}$ .

### Velocity vector

The velocity of the vehicle can be expressed as the time derivative of the position as such

$$\text{Using Euler angles: } \dot{\boldsymbol{\eta}} = \begin{bmatrix} \dot{\mathbf{p}}_{nb}^n \\ \dot{\boldsymbol{\Theta}}_{nb} \end{bmatrix} = [\dot{x}^n, \dot{y}^n, \dot{z}^n, \dot{\phi}, \dot{\theta}, \dot{\psi}]^\top \quad (3.8)$$

$$\text{Using unit quaternions: } \dot{\boldsymbol{\eta}} = \begin{bmatrix} \dot{\mathbf{p}}_{nb}^n \\ \dot{\mathbf{q}}_b^n \end{bmatrix} = [\dot{x}^n, \dot{y}^n, \dot{z}^n, \dot{\eta}, \dot{\varepsilon}_1, \dot{\varepsilon}_2, \dot{\varepsilon}_3]^\top \quad (3.9)$$

When deriving the vehicle kinetics it is however advantageous to express the body velocities vector in  $\{b\}$ . For this the following variables are used

$$\boldsymbol{v} = \begin{bmatrix} \mathbf{v}_{nb}^b \\ \boldsymbol{\omega}_{nb}^b \end{bmatrix} = [u, v, w, p, q, r]^\top \quad (3.10)$$

where

$\mathbf{v}_{nb}^b = [u, v, w]^\top$  is the linear velocity of  $CO$  w.r.t.  $o_n$  expressed in  $\{b\}$ .

$\boldsymbol{\omega}_{nb}^b = [p, q, r]^\top$  is the angular velocity of  $\{b\}$  w.r.t.  $\{n\}$  expressed in  $\{b\}$ .

### Generalized forces and moments

To easily express forces acting on the body-fixed frame, the forces and moment acting on the vehicle will also be expressed in  $\{b\}$ . Consequently

$$\boldsymbol{\tau}^b = \begin{bmatrix} \mathbf{f}_b^b \\ \mathbf{m}_b^b \end{bmatrix} = [X, Y, Z, K, N, M]^\top \quad (3.11)$$

where

$\mathbf{f}_b^b = [X, Y, Z]^\top$  is the force with line of action through  $CO$  expressed in  $\{b\}$ .

$\mathbf{m}_b^b = [K, N, M]^\top$  is the moment about  $CO$  expressed in  $\{b\}$ .

### Transformation between BODY and NED

Since it is decided to express the vehicle velocities in  $\{b\}$ , a way of relating the velocities to the time derivative position in  $\{n\}$  is needed. For linear velocities this is done using a rotation matrix, as defined in (2.2-2.3). Consequently

$$\text{Using Euler angles: } \dot{\mathbf{p}}_{nb}^n = \mathbf{R}(\boldsymbol{\Theta}_{nb}) \mathbf{v}_{nb}^b \quad (3.12)$$

$$\text{Using unit quaternions: } \dot{\mathbf{p}}_{nb}^n = \mathbf{R}(\mathbf{q}_b^n) \mathbf{v}_{nb}^b \quad (3.13)$$

For angular velocities this can be done by using the following transformation

$$\text{Using Euler angles: } \dot{\Theta}_{nb} = T(\Theta_{nb}) \omega_{nb}^b \quad (3.14)$$

$$T(\Theta_{nb}) = \begin{bmatrix} 1 & s\phi t\theta & c\phi t\theta \\ 0 & c\phi & -s\phi \\ 0 & s\phi/c\theta & c\phi/c\theta \end{bmatrix} \quad (3.15)$$

$$\text{Using unit quaternion: } \dot{q}_b^n = T(q_b^n) \omega_{nb}^b \quad (3.16)$$

$$T(q_b^n) = \frac{1}{2} \begin{bmatrix} -\varepsilon_1 & -\varepsilon_2 & -\varepsilon_3 \\ \eta & -\varepsilon_3 & \varepsilon_2 \\ \varepsilon_3 & \eta & -\varepsilon_1 \\ -\varepsilon_2 & \varepsilon_1 & \eta \end{bmatrix} \quad (3.17)$$

**Remark 2** From (3.15) it can be seen that the transformation matrix  $T(\Theta_{nb})$  becomes numerically unstable for  $\theta \rightarrow \pm \frac{\pi}{2}$ . Therefore it is not recommended to use the Euler angle representation if the orientation of the vehicle ever operates close to this limit.

Finally the full state kinematic transformation can be defined as such

$$\dot{\eta} = J_k(\eta) \nu \quad (3.18)$$

where  $k \in \{\theta, q\}$

$$\text{Using Euler angles: } J_\theta(\eta) = \begin{bmatrix} R(\Theta_{nb}) & \mathbf{0}_{3 \times 3} \\ \mathbf{0}_{3 \times 3} & T(\Theta_{nb}) \end{bmatrix} \quad (3.19)$$

$$\text{Using unit quaternions: } J_q(\eta) = \begin{bmatrix} R(q_b^n) & \mathbf{0}_{3 \times 3} \\ \mathbf{0}_{4 \times 3} & T(q_b^n) \end{bmatrix} \quad (3.20)$$

### 3.1.2 Kinetics

Now the kinetics of (3.2) will be described. The kinetics are typically divided into rigid-body kinetics, hydrostatics and hydrodynamics.

#### Rigid-body kinetics

The rigid-body kinetics can be expressed as

$$\mathbf{M}_{RB} \dot{\nu}_r + \mathbf{C}_{RB}(\nu_r) \nu_r = \tau_{RB} \quad (3.21)$$

where

$\mathbf{M}_{RB}$  is the rigid-body system inertia matrix.

$\mathbf{C}_{RB}(\nu_r)$  is the rigid-body Coriolis and centripetal matrix.

When deriving the rigid body matrices it is convenient to do so with respect to the center of gravity first, before transforming the matrices to apply to  $\{b\}$ . If the center of gravity is known this transformation can be computed by defining the vector  $\mathbf{r}_{bg}^b$  from  $CO$  to  $CG$ . The unique parametrization of the rigid-body system inertia matrix then can be described as

$$\mathbf{M}_{RB} = \begin{bmatrix} m\mathbf{I}_3 & -m\mathbf{S}(\mathbf{r}_{bg}^b) \\ m\mathbf{S}(\mathbf{r}_{bg}^b) & \mathbf{I}_g^b - m\mathbf{S}^2(\mathbf{r}_{bg}^b) \end{bmatrix} \quad (3.22)$$

where

$m$  is the mass of the vehicle.

$\mathbf{I}_3$  is  $3 \times 3$  the identity matrix.

$\mathbf{S}(\cdot)$  is the skew-symmetric matrix.

$\mathbf{r}_{bg}^b = [x_g, y_g, z_g]^\top$  is the location of  $CG$  relative to  $CO$  expressed in  $\{b\}$ .

$\mathbf{I}_g^b$  is the inertia matrix about  $CG$  expressed in  $\{b\}$ .

The rigid-body Coriolis and centripetal matrix doesn't have a unique parametrization, but can be parameterized such that the matrix becomes skew-symmetric. A Lagrangian parameterization approach can yield the following expression for the rigid-body Coriolis and centripetal matrix

$$\mathbf{C}_{RB}(\mathbf{v}_r) = \begin{bmatrix} \mathbf{0}_{3 \times 3} & -m\mathbf{S}(\mathbf{v}_{r1}) - m\mathbf{S}(\mathbf{S}(\mathbf{v}_{r2})\mathbf{r}_{bg}^b) \\ -m\mathbf{S}(\mathbf{v}_{r1}) - m\mathbf{S}(\mathbf{S}(\mathbf{v}_{r2})\mathbf{r}_{bg}^b) & m\mathbf{S}(\mathbf{S}(\mathbf{v}_{r1})\mathbf{r}_{bg}^b) - \mathbf{S}(\mathbf{I}_g^b\mathbf{v}_{r2}) \end{bmatrix} \quad (3.23)$$

where

$$\mathbf{v}_{r1} = [u_r, v_r, w_r]^\top$$

$$\mathbf{v}_{r2} = [p_r, q_r, r_r]^\top$$

### Hydrostatics

The gravitational and buoyancy forces acting on a marine craft are called the restoring forces. The gravitational force acts through  $CG$  defined by the vector  $\mathbf{r}_{bg}^b$ , and the buoyancy force acts through the center of buoyancy  $CB$  defined by the vector  $\mathbf{r}_{bb}^b$ , both described relative to  $\{b\}$ .

The magnitude of the restoring forces can be expressed

$$W = mg, \quad B = \rho g \nabla \quad (3.24)$$

where

$m$  is the mass of the vehicle.

$g$  is the acceleration of gravity.

$\rho$  is the water density.

$\nabla$  is the volume of fluid displaced by the vehicle.

Both forces acts in the vertical plane of {n} and can therefore expressed on the following vector form

$$\mathbf{f}_g^n = \begin{bmatrix} 0 \\ 0 \\ W \end{bmatrix}, \quad \mathbf{f}_b^n = - \begin{bmatrix} 0 \\ 0 \\ B \end{bmatrix} \quad (3.25)$$

Rotating to the vectors to {b} yields

$$\begin{aligned} \mathbf{f}_g^b &= \mathbf{R}^\top(\Theta_{nb}) \mathbf{f}_g^n \\ \mathbf{f}_b^b &= \mathbf{R}^\top(\Theta_{nb}) \mathbf{f}_b^n \end{aligned} \quad (3.26)$$

Now that the restoring forces are expressed in {b}, the generalized restoring forces can be expressed. Note that the restoring forces are defined on the left hand side of (3.5), therefore the sign must be corrected accordingly.

$$\begin{aligned} \mathbf{g}(\boldsymbol{\eta}) &= - \begin{bmatrix} \mathbf{f}_g^b + \mathbf{f}_b^b \\ \mathbf{r}_{bg}^b \times \mathbf{f}_g^b + \mathbf{r}_{bb}^b \times \mathbf{f}_b^b \end{bmatrix} \\ &= - \begin{bmatrix} \mathbf{R}^\top(\Theta_{nb}) (\mathbf{f}_g^n + \mathbf{f}_b^n) \\ \mathbf{r}_{bg}^b \times \mathbf{R}^\top(\Theta_{nb}) \mathbf{f}_g^n + \mathbf{r}_{bb}^b \times \mathbf{R}^\top(\Theta_{nb}) \mathbf{f}_b^n \end{bmatrix} \end{aligned} \quad (3.27)$$

where

$$\begin{aligned} \mathbf{r}_{bb}^b &= [x_b, y_b, z_b]^\top \text{ is the location of } CB \text{ relative to } CO \text{ expressed in } \{b\}. \\ \mathbf{r}_{bg}^b &= [x_g, y_g, z_g]^\top \text{ is the location of } CG \text{ relative to } CO \text{ expressed in } \{b\}. \end{aligned}$$

### Hydrodynamics

The forces due to hydrodynamic can be expressed as

$$\mathbf{M}_A \dot{\boldsymbol{\nu}}_r + \mathbf{C}_A(\boldsymbol{\nu}_r) \boldsymbol{\nu}_r + \mathbf{D}(\boldsymbol{\nu}_r) \boldsymbol{\nu}_r = -\boldsymbol{\tau}_{hyd} \quad (3.28)$$

where

$$\begin{aligned} \mathbf{M}_A &\text{ is the added mass matrix.} \\ \mathbf{C}_A(\boldsymbol{\nu}_r) &\text{ is the hydrodynamic Coriolis-centripetal matrix.} \\ \mathbf{D}(\boldsymbol{\nu}_r) &= \mathbf{D} + \mathbf{D}_n(\boldsymbol{\nu}_r) \text{ is a nonlinear damping matrix.} \end{aligned}$$

The motion of an underwater vehicle moving at high relative speed will be highly nonlinear and coupled. However, for underwater vehicles moving at low speeds and with three planes of symmetry, the off-diagonal elements of  $\mathbf{M}_A$  is typically neglected. The diagonal structure is rarely used since it is time consuming to determine the off-diagonal elements from experiments as well as from theory. In practice, the constant diagonal approximation is found to be quite good for many applications. This is due to the fact that the off-diagonal elements of a positive inertia matrix will be much smaller than their diagonal counterparts [3]. Hence, the added mass is chosen as the constant diagonal matrix

$$\mathbf{M}_A = -\text{diag} \{X_{\dot{u}}, Y_{\dot{v}}, Z_{\dot{w}}, K_{\dot{p}}, M_{\dot{q}}, N_{\dot{r}}\} \quad (3.29)$$



where the diagonal elements are added mass along the different axes.

The hydrodynamic Coriolis–centripetal matrix does not have unique parameterization. However, it can always be parameterized such that it is skew-symmetric and one representation is

$$\mathbf{C}_A(\mathbf{v}_r) = \begin{bmatrix} \mathbf{0}_{3 \times 3} & -\mathbf{S}(\mathbf{A}_{11} \mathbf{v}_{r1} + \mathbf{A}_{12} \mathbf{v}_{r2}) \\ -\mathbf{S}(\mathbf{A}_{11} \mathbf{v}_{r1} + \mathbf{A}_{12} \mathbf{v}_{r2}) & -\mathbf{S}(\mathbf{A}_{21} \mathbf{v}_{r1} + \mathbf{A}_{22} \mathbf{v}_{r2}) \end{bmatrix} \quad (3.30)$$

where  $\mathbf{A}_{ij} \in \mathbb{R}^{3 \times 3}$  is defined as

$$\mathbf{M}_A := \begin{bmatrix} \mathbf{A}_{11} & \mathbf{A}_{12} \\ \mathbf{A}_{21} & \mathbf{A}_{22} \end{bmatrix} \quad (3.31)$$

Consequently, the hydrodynamic Coriolis–centripetal matrix becomes

$$\mathbf{C}_A(\mathbf{v}_r) = \begin{bmatrix} 0 & 0 & 0 & 0 & -Z_{\dot{w}} w_r & Y_{\dot{v}} v_r \\ 0 & 0 & 0 & Z_{\dot{w}} w_r & 0 & -X_{\dot{u}} u_r \\ 0 & 0 & 0 & -Y_{\dot{v}} v_r & X_{\dot{u}} u_r & 0 \\ 0 & -Z_{\dot{w}} w_r & Y_{\dot{v}} v_r & 0 & -N_{\dot{r}} r & M_{\dot{q}} q \\ Z_{\dot{w}} w_r & 0 & -X_{\dot{u}} u_r & N_{\dot{r}} r & 0 & -K_{\dot{p}} p \\ -Y_{\dot{v}} v_r & X_{\dot{u}} u_r & 0 & -M_{\dot{q}} q & K_{\dot{p}} p & 0 \end{bmatrix} \quad (3.32)$$

The damping terms for marine vehicles can also be highly complicated and nonlinear. One representation of the damping is using both a linear and quadratic term. Assuming an underwater vehicle with symmetry in three planes, and where the contributions from the off-diagonal elements are small compared to the diagonal elements, the damping term can be expressed as a diagonal. Consequently

$$\mathbf{D}(\mathbf{v}_r) = -\underbrace{\text{diag}\{X_u, Y_v, Z_w, K_p, M_q, N_r\}}_D - \underbrace{\text{diag}\{X_{|u|u}|u_r|, Y_{|v|v}|v_r|, Z_{|w|w}|w_r|, K_{|p|p}|p|, M_{|q|q}|q|, N_{|r|r}|r|\}}_{D_N(\mathbf{v}_r)} \quad (3.33)$$

## 3.2 Simplified Low-speed Maneuvering Model

For low-speed maneuvering the relative velocities can be assumed to be small during operations as long as the current velocity is reasonably bounded. Hence, it can be justified to reduce the equation of motions of (3.2) to disregard second order terms of  $\mathbf{v}_r$ . This includes the Coriolis, centripetal and nonlinear damping terms. Consequently the simplified low-speed maneuvering model can be expressed as

$$\dot{\boldsymbol{\eta}} = \mathbf{J}_k(\boldsymbol{\eta})(\mathbf{v}_r + \mathbf{v}_c) \quad (3.34)$$

$$\mathbf{M} \dot{\mathbf{v}}_r + \mathbf{D} \mathbf{v}_r + \mathbf{g}(\boldsymbol{\eta}) = \boldsymbol{\tau} \quad (3.35)$$

where  $\mathbf{M} = \mathbf{M}_{RB} + \mathbf{M}_A$ .

### Rigid-body Kinetics

By assuming that the design center ( $CO$ ) is defined close to the center of gravity ( $CG$ ) such that  $r_{bg}^b \approx [0, 0, 0]$ , the rigid-body system inertia matrix can be seen to reduce to a diagonal matrix by using (3.22). Consequently

$$M_{RB} = \begin{bmatrix} m & 0 & 0 & 0 & 0 & 0 \\ 0 & m & 0 & 0 & 0 & 0 \\ 0 & 0 & m & 0 & 0 & 0 \\ 0 & 0 & 0 & I_{xx}^b & 0 & 0 \\ 0 & 0 & 0 & 0 & I_{yy}^b & 0 \\ 0 & 0 & 0 & 0 & 0 & I_{zz}^b \end{bmatrix} \quad (3.36)$$

### Hydrostatics

By assuming that the underwater vehicle is zero-mean stabilized in roll and pitch, further simplifications can be made. This can be done by ensuring that the center of buoyancy ( $CB$ ) is located vertically above the center of gravity, such that  $r_{bb}^b = [0, 0, z_b]$ . The restoring forces can then be expressed as

$$\mathbf{g}(\boldsymbol{\eta}) = \begin{bmatrix} (W - B) \sin(\theta) \\ -(W - B) \cos(\theta) \sin(\phi) \\ -(W - B) \cos(\theta) \cos(\phi) \\ -z_b B \cos(\theta) \sin(\phi) \\ -z_b B \sin(\theta) \\ 0 \end{bmatrix} \quad (3.37)$$

It is known that  $z_b$  and  $B$  can be designed to stabilize the vehicle about  $\phi = 0$  and  $\theta = 0$ , for  $z_b < 0$ . This self stabilizing design will ensure open-loop stability of a zero-mean roll and pitch angle. Hence, by applying this assumption, the restoring forces will be approximated as the following for the simplified model

$$\mathbf{g}(\boldsymbol{\eta}) \approx \begin{bmatrix} 0 \\ 0 \\ -(W - B) \\ 0 \\ 0 \\ 0 \end{bmatrix} \quad (3.38)$$

where  $W = mg$ , and  $B = \rho g \nabla$ .

### Hydrodynamics

There exist different methods for determining hydrodynamic coefficients for underwater vehicles. There are empirical methods where one can use knowledge of the geometrical shape of the vehicle, numerical methods like computational fluid

dynamics (CFD), system identification and experimental methods. Assuming low-speed maneuvering it can be justified to simplify the hydrodynamic coefficient into a linear damping matrix as the second order terms gets small in comparison ( $\mathbf{D}_N(\mathbf{v}_r)\mathbf{v}_r \approx 0$ ). For the low-speed maneuvering model, the hydrodynamic coefficients will therefore be regarded as follows

$$\mathbf{M}_A = -\text{diag}\{X_{\dot{u}}, Y_{\dot{v}}, Z_{\dot{w}}, K_{\dot{p}}, M_{\dot{q}}, N_{\dot{r}}\} \quad (3.39)$$

$$\mathbf{D} = -\text{diag}\{X_u, Y_v, Z_w, K_p, M_q, N_r\} \quad (3.40)$$

### Transformations using zero-mean roll and pitch assumptions

Designing the restoring forces as in (3.37), presumably zero-mean stabilizes the roll and pitch dynamics. Consequently further simplifications can be made. By using the approximations ( $\psi \approx 0$ ) and ( $\theta \approx 0$ ), the rotation matrix can be approximated to

$$\mathbf{R}(\Theta_{nb}) \approx \begin{bmatrix} \cos(\psi) & -\sin(\psi) & 0 \\ \sin(\psi) & \cos(\psi) & 0 \\ 0 & 0 & 1 \end{bmatrix} \quad (3.41)$$

In accordance with Remark 2, the Euler angle representation will be used for the rest of this thesis for simplicity. Consequently the simplified velocity transformation matrix will be described using Euler angles and approximated as follows

$$\mathbf{T}(\Theta_{nb}) \approx \begin{bmatrix} 1 & 0 & 0 \\ 0 & 1 & 0 \\ 0 & 0 & 1 \end{bmatrix} \quad (3.42)$$

and consequently

$$\mathbf{J}_\theta(\boldsymbol{\eta}) \approx \begin{bmatrix} \cos(\psi) & -\sin(\psi) & 0 & 0 & 0 & 0 \\ \sin(\psi) & \cos(\psi) & 0 & 0 & 0 & 0 \\ 0 & 0 & 1 & 0 & 0 & 0 \\ 0 & 0 & 0 & 1 & 0 & 0 \\ 0 & 0 & 0 & 0 & 1 & 0 \\ 0 & 0 & 0 & 0 & 0 & 0 \end{bmatrix} \quad (3.43)$$

### Irrotational Constant Ocean Currents using zero-mean roll and pitch assumptions

As mentioned, the irrotational constant ocean currents can be expressed as three constant linear velocities w.r.t. the inertial frame as such

$$\mathbf{v}_c^n = [\dot{x}_c^n, \dot{y}_c^n, \dot{z}_c^n]^\top \quad (3.44)$$

$$\dot{\mathbf{v}}_c^n = [0, 0, 0]^\top \quad (3.45)$$

Rotating the current velocities to the body frame, and using the zero-mean roll and pitch assumptions from (3.41), gives

$$\begin{aligned}
\mathbf{v}_c^b &= \mathbf{R}(\Theta_{nb})^\top \mathbf{v}_c^n \\
&= \begin{bmatrix} \cos(\psi) & \sin(\psi) & 0 \\ -\sin(\psi) & \cos(\psi) & 0 \\ 0 & 0 & 1 \end{bmatrix} \begin{bmatrix} \dot{x}_c^n \\ \dot{y}_c^n \\ \dot{z}_c^n \end{bmatrix} \\
&= \begin{bmatrix} \cos(\psi)\dot{x}_c^n + \sin(\psi)\dot{y}_c^n \\ -\sin(\psi)\dot{x}_c^n + \cos(\psi)\dot{y}_c^n \\ \dot{z}_c^n \end{bmatrix}
\end{aligned} \tag{3.46}$$

Transforming to amplitude-phase form gives

$$\mathbf{v}_c^b = \begin{bmatrix} U_c \cos(\chi_c - \psi) \\ U_c \sin(\chi_c - \psi) \\ \dot{z}_c^n \end{bmatrix} \tag{3.47}$$

where  $U_c = \sqrt{\dot{x}_c^{n2} + \dot{y}_c^{n2}}$  is the amplitude of the current velocities in the horizontal plane, and  $\chi_c$  is the horizontal course angle of the current. Further [3] shows that the current linear accelerations in the body frame can be expressed as

$$\dot{\mathbf{v}}_c^b = -\mathbf{S}(\boldsymbol{\omega}_{nb}^b) \mathbf{v}_c^b \tag{3.48}$$

Again, assuming zero-mean roll and pitch dynamics, and inserting (3.47), gives

$$\dot{\mathbf{v}}_c^b = \begin{bmatrix} rU_c \sin(\chi_c - \psi) \\ -rU_c \cos(\chi_c - \psi) \\ 0 \end{bmatrix} \tag{3.49}$$

Now the simplified 6 DOF current velocities and accelerations in the body frame can be expressed as

$$\mathbf{v}_c = \begin{bmatrix} u_c \\ v_c \\ w_c \\ 0 \\ 0 \\ 0 \end{bmatrix} = \begin{bmatrix} U_c \cos(\chi_c - \psi) \\ U_c \sin(\chi_c - \psi) \\ \dot{z}_c^n \\ 0 \\ 0 \\ 0 \end{bmatrix} \tag{3.50}$$

$$\dot{\mathbf{v}}_c = \begin{bmatrix} \dot{u}_c \\ \dot{v}_c \\ \dot{w}_c \\ 0 \\ 0 \\ 0 \end{bmatrix} = \begin{bmatrix} rU_c \sin(\chi_c - \psi) \\ -rU_c \cos(\chi_c - \psi) \\ 0 \\ 0 \\ 0 \\ 0 \end{bmatrix} \tag{3.51}$$

### Equations of motion using zero-mean roll and pitch assumptions

By including the simplified irrotational constant currents in the kinetic equation from (3.35), the final simplified slow-speed maneuvering model using the zero-mean roll and pitch simplifications can be expressed as

$$\dot{\eta} = J_{\theta}(\eta)\nu \quad (3.52)$$

$$\text{diag} \left\{ \underbrace{\begin{bmatrix} m - X_{\dot{u}} \\ m - Y_{\dot{v}} \\ m - Z_{\dot{w}} \\ I_{xx}^b - K_{\dot{p}} \\ I_{yy}^b - M_{\dot{q}} \\ I_{zz}^b - N_{\dot{r}} \end{bmatrix}}_M \right\} (\dot{\nu} - \dot{\nu}_c) + \text{diag} \left\{ \underbrace{\begin{bmatrix} -X_u \\ -Y_v \\ -Z_w \\ -K_p \\ -M_q \\ -N_r \end{bmatrix}}_D \right\} (\nu - \nu_c) + \underbrace{\begin{bmatrix} 0 \\ 0 \\ -(W - B) \\ 0 \\ 0 \\ 0 \end{bmatrix}}_{g(\eta)} = \tau \quad (3.53)$$

where

$$J_{\theta}(\eta) \leftarrow (3.43).$$

$$\nu_c \leftarrow (3.50).$$

$$\dot{\nu}_c \leftarrow (3.51).$$

The above equations will further be the design basis for the guidance and control system considered later in this thesis.

### 3.3 Thruster Dynamics

Thrusters are the popular choice for achieving actuation in the regime of low-speed maneuvering for underwater vehicles. The type and configuration of thrusters are therefore a main contributor for determining the dynamical limitations for the specific vehicle. It is therefore highly relevant to consider the models and limitations for the actuation achieved by thrusters. To directly measure the force contribution of each individual thrusters in real time is however difficult, and it is therefore usual to define a force model based on its propeller revolution which can easily be controlled using Electronic Speed Controllers (ESCs). In a general sense this is regraded as low-level actuator control and is illustrated in Figure 3.2. Even though this kind of system requires feedback control for the propeller revolution, the closed-loop dynamics are relatively fast compared to the vehicle dynamics and are can therefore be regarded as a zero-order system when observing it from the higher level motion control systems. Further in this section a low-level actuator control system will be modelled to be included in the simulation testbed, but also to define the control input constraints to be included in the guidance and control system.

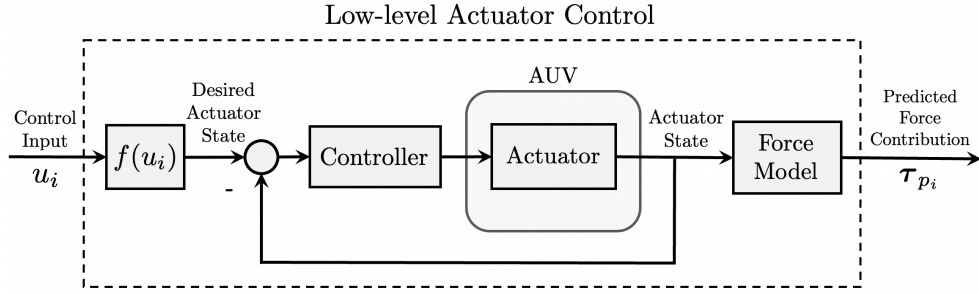


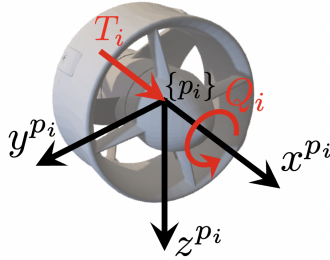
Figure 3.2: Low-level actuator control

### 3.3.1 Case study: Modelling the low-level actuator control system for the T200 thrusters

This case study aims at modelling a low-level control system for thrusters equipped with a fast Electronic Speed Controller (ESC). For sake of reference the T200 BlueROV2 thruster from Blue Robotics will be modelled.

#### Force model for the T200 thrusters

When describing the force models for each thruster it is convenient to do so in relative reference frames. The reference frames will be denoted  $\{p_i\}$  for  $i = 1, 2, \dots, r$ , where  $r$  is the number of thrusters. The the relative location of the thruster frames are illustrated in Figure 3.3.

Figure 3.3: Illustration of the thruster frames  $\{p_i\}$ 

The thrust  $T$  and torque  $Q$  of the thrusters can be approximated to the following bilinear form according to [3]

$$T = T_{|n|n}|n|n - T_{|n|u_a}|n|u_a \quad (3.54)$$

$$Q = Q_{|n|n}|n|n - Q_{|n|u_a}|n|u_a \quad (3.55)$$

where

$n$  (rpm) is the thruster revolution.

$u_a$  is the speed of the water in the wake of the hull (advance speed).  
 $T_{|n|n}$  and  $T_{|n|u_a}$  are linear coefficients.

The advance speed  $u_a$  is equal to the linear velocity vector of the vehicle decomposed along the  $x$  axis of the thruster frame. It is possible to continuously calculate this for each thruster, but since the advance speed in the regime of low-speed maneuvering case is small,  $u_a$  will be approximated equal to zero for simplicity. The effects of the torques on the vehicle are also expected to be small, hence will the torque components also be neglected ( $Q \approx 0$ ). Consequently, the approximated thrust model becomes similar to [15]

$$T(n_i) = T_{|n|n}|n_i|n_i \quad (3.56)$$

The force model can then be expressed in the thruster frames as such

$$\tau_i^{P_i} = [T(n_i), 0, 0, 0, 0, 0]^T \quad \text{for } i = 1, 2, \dots, r \quad (3.57)$$

#### Finding the linear coefficient $T_{|n|n}$

The numerical value for the linear coefficient  $T_{|n|n}$  can be found by performing a curve fit on performance data for the specific thruster under bollard-pull conditions ( $u_a = 0$ ). For the T200 thruster, this data set is already provided by the manufacturers, and can be found at <https://bluerobotics.com/store/thrusters/t100-t200-thrusters/t200-thruster-r2-rp/>. The function to be approximated is (3.56), and the linear coefficient  $T_{|n|n}$  will be found by using the fit-function on the performance data in Matlab. The final result can be seen in Figure 3.4. By inspection one can see that the bilinear model with ( $T_{|n|n} = 3.64 \cdot 10^{-6}$ ) is a reasonable approximation when comparing to the performance data. Consequently the linear coefficient was chosen as

$$T_{|n|n} = 3.64 \cdot 10^{-6} \quad (3.58)$$

#### Actuator dynamics

As mentioned, the revolution of each thruster is assumed to be controlled by Electronic Speed Controllers (ESC). The closed-loop system is assumed to approximate a first-order system as such

$$\frac{n_i}{n_{id}}(s) = \frac{1}{Ts + 1} \quad (3.59)$$

where

$n_{id}$  [rpm] is the desired thruster revolution.

$n_i$  [rpm] is the actual thruster revolution.

$T$  [s] is the time constant of the closed-loop system.

The time constant could be found by performing step responses on the actual system. However since real-life experiments has a low priority for the scope of

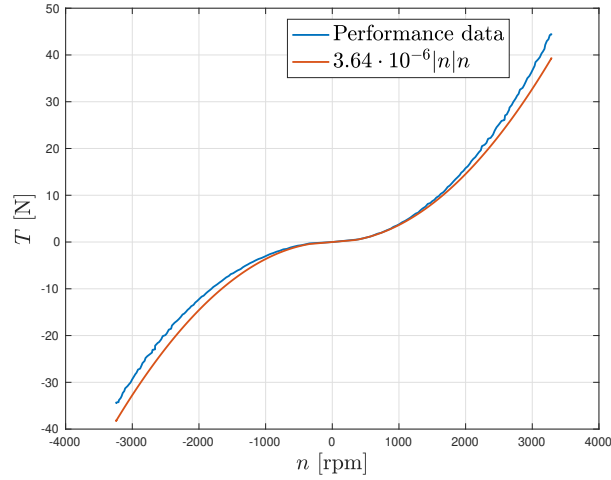


Figure 3.4: Curve fit on the performance data for the T200 Thruster

this thesis, the time constant will be roughly estimated. For small thrusters as the T200, small time constants can be expected. Therefore the time constant for the T200 will be approximated as follows for the sake of convenience.

$$T = 0.2 \text{ [s]} \quad (3.60)$$

### Defining the conversion function $f(u_i)$

When observing the low-level actuator control system from a higher level control system perspective it can be convenient if the low-level actuator control system becomes as simple as possible when observing it from input to output. Hence a conversion function will be defined for this purpose. By using (3.56-3.57), and including the actuator dynamics from (3.59), it can be seen that the low-level control system so far can be expressed as

$$\tau_i^{P_i}(s) = \frac{T|n|n}{Ts + 1} [ |n_{id}|n_{id}, 0, 0, 0, 0, 0 ]^T \quad (3.61)$$

By defining the actuator control inputs as

$$u_i = T|n|n|n_{id}|n_{id} \quad (3.62)$$

it can be seen that the closed-loop low-level actuator control system can be expressed as follows

$$\frac{\tau_i^{P_i}}{u_i}(s) = \frac{1}{Ts + 1} [1, 0, 0, 0, 0, 0]^T \quad (3.63)$$



Hence by solving (3.62) for the desired actuator state, the conversion function can be chosen as

$$n_{id} = \underbrace{\text{sgn}(u_i) \sqrt{\frac{|u_i|}{T_{|n|n}}}}_{f(u_i)} \quad (3.64)$$

Consequently, the final low-level actuator control system when using  $n$  numbers of thrusters becomes the equivalent systems as illustrated in Figure 3.5.

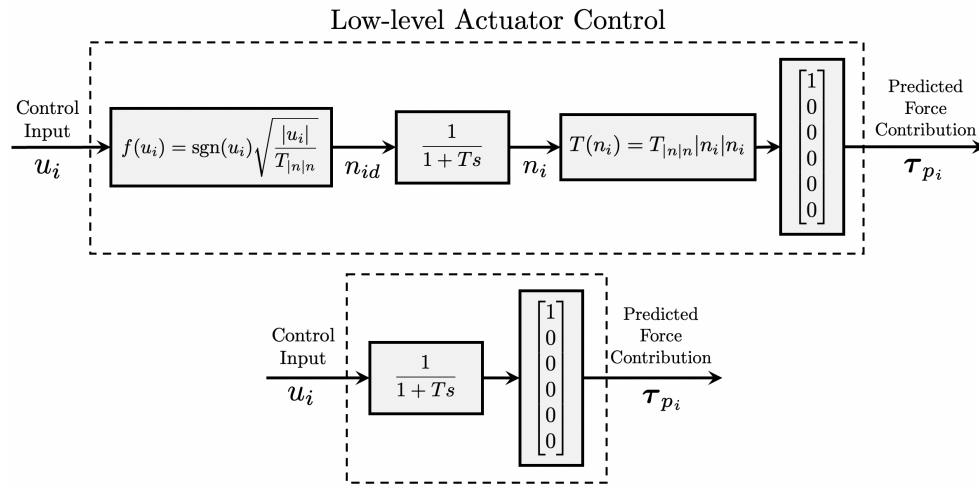


Figure 3.5: A low-level actuator control system for thrusters

### Defining the range of feasible control inputs

Finally it is also convenient to know the saturation limits for the low-level actuator control inputs when designing the higher level control systems. The saturation limits may vary with type of actuator, the range where the force model is expected to be valid, electronic limitation of the system, and so forth. Assuming there are no electrical limitation, the constraints of the T200 thrusters will be set to the range where the binomial model of (3.56) is a good approximation. By observing Figure 3.4, the thruster saturation limits will be set to  $n_i \in [-1700, 1700]$  for the sake of example. By combining (3.62) and (3.58), the control input saturation limits can then be defined as follows

$$u_i \in [-10.5, 10.5] \quad (3.65)$$



## Chapter 4

# Simulation Testbed and Software

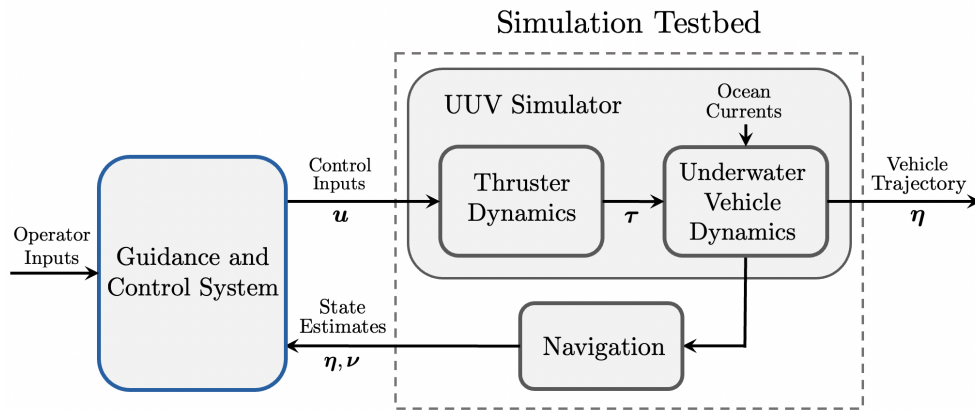


Figure 4.1: Illustration of the integration of the simulation testbed

A simulation testbed is required to verify guidance and control system in a realistic manner. Figure 4.1 shows how a simulation testbed will be integrated together with the guidance and control system. It is worth noticing that this type of interface makes it easy to replace the simulation testbed with an actual vehicle at a later occasion. This chapter will further account for the different modules depicted in the simulation testbed, as well as for the software used to integrate the systems.

### 4.1 Robot Operating System (ROS)

The software to be used for integrating the different modules is Robot Operating System (ROS) [16]. ROS is an open source robotics middleware suite providing libraries and tools for software developers to create robot applications. The software provides hardware abstraction, device drivers, libraries, visualizers, message-

passing, package management, and more [17].

ROS is compatible with several programming languages such as Python, C++, MATLAB, Java and more. To enable fast implementation of the different modules of the guidance and control system, the "high-productive" language of Python is used in the majority of the experiments.

## 4.2 The UUV Simulator

Simulation experiments will be performed using the UUV Simulator [18]. The UUV Simulator is chosen for its neat API for initialization and simulation of underwater vehicle and thruster dynamics. The UUV simulator integrates both ROS and Gazebo for its simulations, where Gazebo is an open source physics engine to accurately and efficiently simulate robots in 3D [19].

### Thruster dynamics

The UUV Simulator provides several plugins simulating actuator models for underwater vehicles in Gazebo. This thesis will use the thruster plugin, which can be initialized by specifying the thrusters body-fixed poses, and the desired type of force model and dynamic response. As described in Section 3.3.1, the quadratic force model of (3.56), and first-order dynamics of (3.59) will be included in the simulator. Hence the required parameters for the thruster plugin are given in Table 4.1.

**Table 4.1:** Parameters required for the UUV Simulator thruster plugin

Notation	Description
$T_{ n n}$	Thrust coefficient
$T$	First-order time constant
$p_{bt_i}^b$	Positions of the thrusters w.r.t the body frame
$\Theta_{bt_i}$	Orientations of the thrusters w.r.t the body frame

### Underwater vehicle dynamics

The thruster plugin eventually produces a set of forces and moments acting on the rigid-body. The UUV Simulator integrates this with the same equations of motions as described in Section 3.1, hence simulation will be performed in 6 DOF. It is also possible to include constant and irrotational ocean currents w.r.t. the inertial frame in the simulation. Consequently the required parameters for simulating the underwater vehicle dynamics are given in Table 4.2.

**Remark 3** *During experiments with the UUV simulator there was discovered a undesirable coupled motion between the linear velocity and a moment acting in yaw for*

the vehicle. The source of the coupling was not found, hence this inconsistency will be regarded as a structural disturbance for the simulations.

**Table 4.2:** Parameters required UUV Simulator vehicle dynamics

Notation	Description
$m$	Mass of the vehicle
$I_g^b$	Inertia of the vehicle
$\nabla$	The volume of fluid displaced by the vehicle
$r_{bb}^b$	Location of center of buoyancy
$r_{bg}^b$	Location of center of gravity
$M_A$	Added mass matrix
$D$	Linear damping matrix
$D_n(\mathbf{v}_r)$	Quadratic damping matrix
$\mathbf{v}_c^n$	Linear ocean current velocities w.r.t. the inertial frame

### 4.3 Navigation System

The objective of the navigation systems is to determine the state estimates of the vehicle. The absence of Global Navigation Satellite Systems (GNSS) makes underwater navigation a challenging task, and the methods are typically divided into three categories. There are dead-reckoning and inertial navigation, acoustic navigation and geophysical navigation [6]. This thesis will not go in depth regarding the navigation system, but since motion control is highly dependent on the state estimates it is only reasonable to cover what state estimates are presumably available.

Most AUV applications are able to achieve reliable short term estimations using dead-reckoning and inertial navigation systems (INS) [20]. They are often based on the Inertial Measurement Units (IMU) which uses a combination of accelerometers and gyroscopes to estimate the vehicle's orientation, velocity, and gravitational forces [20]. However these methods are often prone to positional drift and requires external sensors to aid their position and velocity estimates to prevent error growth. This approach is called Aided Inertial Navigation System (A-INS). Doppler Velocity Logs (DVLs), which transmits acoustic pulses onto the seabed and measures the Doppler shifted returns, are able to obtain a 3D velocity vector of the vehicle. Compasses can be used to measure the heading of the vehicle, and pressure sensors are able to measure the depth. Hence by applying sensor fusion methods on the above sensors it is reasonable to assume successful estimations of the depth, heading and velocity of the vehicle are possible to obtain. However there still is a lack of the ability to estimate the horizontal position without suffering positional error as time increases. Therefore methods to achieve positional aiding measurements using acoustic communication and Simultaneous Localization and Mapping (SLAM) are popular research topics regarding underwater naviga-

tion. Even though it seems like these methods needs to be formalized and tested better, the recent advances also seems to progress this field at an unprecedented rate [21]. Given that the A-INS either have low positional error growth, or that acoustic communication or SLAM methods are able to obtain the position of the vehicle, the state estimates given in Table 4.3 will be regarded as available for the scope of this thesis (remember that the roll and pitch dynamics are assumed zero-mean stable). The measurements will simply be obtained by using the ground truth values provided by the UUV Simulator.

**Table 4.3:** The state estimates which is assumed available for the guidance and control system

Notation	Description
$x^n$	Position in north
$y^n$	Position in east
$z^n$	Depth
$\psi$	Heading angle
$u$	Linear velocity in surge
$v$	Linear velocity in sway
$w$	Linear velocity in heave
$r$	Angular velocity in yaw

#### 4.4 Beluga NTNU

Beluga NTNU is an AUV recently developed by the independent student organization, Vortex NTNU in Trondheim, Norway. This AUV will serve as the test application for the case studies in which requires a model of a vehicle. The AUV acquires eight body-fixed t200 thrusters where their locations w.r.t. the body frame are known. All necessary parameters to simulate the vehicle can be found in Appendix A, and are all compatible with the parameter setup for the UUV Simulator. Figure 4.2 shows the visual model of Beluga NTNU in Gazebo.

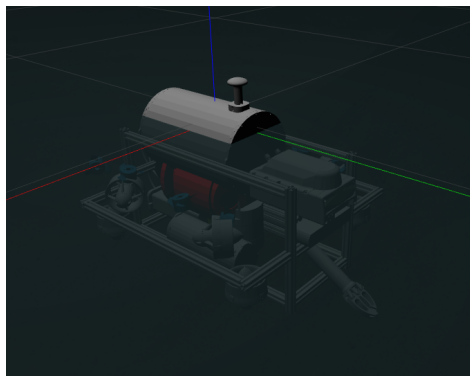


**Figure 4.2:** The visual model of Beluga NTNU in Gazebo

## Chapter 5

# Control System

Figure 5.1 illustrates the architecture of the control system to be modelled in this section. The goal of the system is for the underwater vehicle to be able to track smooth trajectories enabled by the means of its thrusters. A low-level actuator control system for thrusters have already been described and modelled in Section 3.3.1. Hence this section will only consider the motion control and control allocation modules.

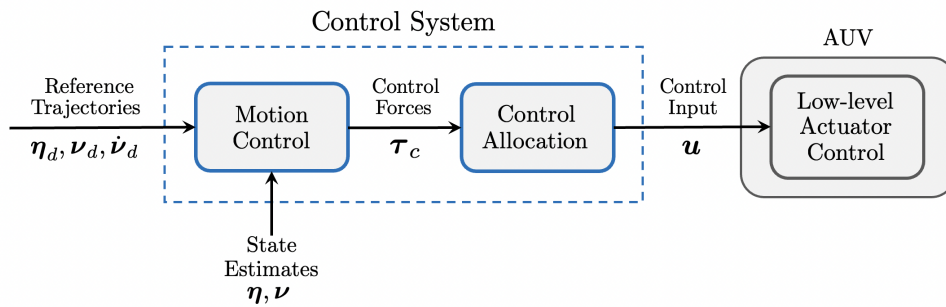


Figure 5.1: Illustration of the Control System

**Motion Control:** As previously shown, the kinetics of a rigid-body underwater vehicle can be reduced to a total of six degrees of freedom. In the regime of low-speed maneuvering it has also been shown that one can expect a low degree of coupling with this representation. Both these observations makes it convenient to design a motion control system to compute control forces to apply in the body-fixed frame. The space of controllable forces produced by the actuators are however rarely identical to the Euclidean space of the body frame. Hence there is a need for control allocation when choosing this design methodology.

**Control Allocation:** The objective of control allocation is to efficiently distribute control inputs to the different actuators, such that the resultant forces pro-

duced by the effectors replicates the control forces given as input. Achieving this successfully further requires that the relationship between control input and the individual force vectors produced by the effectors are known. In fact this is the objective of low-level actuator control.

**Low-level Actuator Control:** Low-level actuator control is about regulating the actuator states such that there is a well defined relationship between the control inputs of each actuator, and the expected force generated by the respective effectors. In a general sense this includes for instance rpm control of a propeller, or the angle of a rudder. The low-level control subsystem is often approximated to a zero-order system when observed from the higher-level motion control system. This approximation typically holds when there is a sufficient control bandwidth separation between two closed-loop systems.

## 5.1 Control Allocation

The objective of the control allocation system is to map control forces  $\tau_c$ , to control inputs  $u$ , such that the sum of forces acting on the rigid body is equivalent to one another. A survey of state-of-the art methods for marine craft, aircraft and automotive systems can be found in [7]. In this section a step-by-step procedure to find the control allocation mapping for an underwater vehicles using body-fixed thrusters will be presented and demonstrated. In addition a module to optimize the control forces when saturation on the control inputs are active will be proposed.

1. **Express the force component for each thruster as a function of the actuator inputs**

$$\tau_i^{p_i} = f(u_i) \quad \text{for } i = 1, 2, \dots, r \quad (5.1)$$

2. **Define the location of each thruster relative to the body frame**

$$\begin{bmatrix} \mathbf{p}_{b p_i}^b \\ \boldsymbol{\theta}_{b p_i} \end{bmatrix} = \begin{bmatrix} x_{p_i}^b, y_{p_i}^b, z_{p_i}^b, \phi_{p_i}, \theta_{p_i}, \psi_{p_i} \end{bmatrix}^\top \quad \text{for } i = 1, 2, \dots, r \quad (5.2)$$

**Remark 4** For azimuth thrusters, the thruster frames can also be defined as a function of actuator inputs steering the relative angles of the thrusters.

3. **Transform the force component expressed in each thruster frame to apply in the body frame**

Since the moment component expressed in each thruster frame is regarded as small, i.e.,  $\mathbf{T}_i^{p_i} \approx 0$ , only the linear force component  $\mathbf{F}_i^{p_i}$  will be taken into account for this transformation. The resultant force acting on the rigid body will be found by first rotating the force component to  $\{b\}$  as such



$$\mathbf{F}_i^b = \mathbf{R}(\Theta_{bp_i})\mathbf{F}_i^{p_i} \quad (5.3)$$

Thereafter vectorial mechanics will be used to describe how the force components affects  $\{b\}$ , as if the forces lines of action was defined in  $CO$  as such

$$\boldsymbol{\tau}^b = \begin{bmatrix} \mathbf{F}^b \\ \mathbf{T}^b \end{bmatrix} = \begin{bmatrix} \sum_{i=1}^N \mathbf{F}_i^b \\ \sum_{i=1}^N (\mathbf{p}_{bp_i}^b \times \mathbf{F}_i^b) \end{bmatrix} \quad (5.4)$$

where

- $\mathbf{R}(\Theta_{bp_i})$  is the Euler-angle rotation from  $\{p_i\}$  to  $\{b\}$  expressed in  $\{b\}$ .
- $\mathbf{p}_{bp_i}^b$  is the translation from  $\{b\}$  to  $\{p_i\}$  expressed in  $\{b\}$ .
- $\mathbf{F}^b$  is the resultant force component in  $\{b\}$ .
- $\mathbf{T}^b$  is the resultant moment component in  $\{b\}$ .

#### 4. Find the inverse mapping from resultant forces expressed in the body frame to the control inputs

If the above steps are followed correctly it should now be possible to express the mapping from control inputs to control forces as follows

$$\boldsymbol{\tau}^b = \mathbf{B}(\mathbf{u}) \quad (5.5)$$

If the mapping is nonlinear in the control inputs, nonlinear optimization techniques might be required to find the inverse mapping. However if the mapping is linear in the control inputs, and the system is over actuated, that is

$$\boldsymbol{\tau}^b = \mathbf{B}\mathbf{u} \quad (5.6)$$

$$\text{where } \boldsymbol{\tau}^b \in \mathbb{R}^{n=6}, \quad \mathbf{u} \in \mathbb{R}^r \quad (5.7)$$

$$\text{and } r > n = 6 \quad (5.8)$$

the inverse mapping can finally be defined using the Moore–Penrose pseudoinverse as such

$$\mathbf{u} = \mathbf{B}^\dagger \boldsymbol{\tau}_c \quad \text{where } \mathbf{B}^\dagger = \mathbf{B}^\top (\mathbf{B}\mathbf{B}^\top)^{-1} \quad (5.9)$$

where  $\boldsymbol{\tau}_c$  are the control forces and  $\mathbf{B}^\dagger$  is the Moore–Penrose pseudoinverse of the input matrix.

### 5.1.1 Case study: Modelling the control allocation system for Beluga NTNU

In this case study a control allocation system for an underwater vehicle using body-fixed thrusters will be modelled using the procedure described in the previous section. The vehicle to be modelled is the Beluga NTNU, where the model parameters can be found in Appendix A.

1. **Express the force component for each thruster as a function of the actuator inputs**

Beluga NTNU acquires eight T200 thrusters. The force component of the T200 thrusters have already been defined in the case study done in Section 3.3.1. Consequently

$$\boldsymbol{\tau}_i^{p_i} = \begin{bmatrix} \mathbf{F}_i^{p_i} \\ \mathbf{T}_i^{p_i} \end{bmatrix} = \frac{1}{T_S + 1} [1, 0, 0, 0, 0, 0]^\top u_i \quad \text{for } i = 1, 2, \dots, 8 \quad (5.10)$$

2. **Define the location of each thruster relative to the body frame**

The location of each thruster w.r.t the body frame is already known for Beluga NTNU and their numerical values are provided in Table 5.1.

**Table 5.1:** Numerical values for the locations of the thrusters for Beluga NTNU

Thruster nr.	$\mathbf{p}_{bt_i}^b$ [m]	$\boldsymbol{\Theta}_{bt_i}$ [rad]
1	$[0.238, 0.220, -0.065]^\top$	$[0, 0, \frac{3\pi}{4}]^\top$
2	$[0.120, 0.220, -0.065]^\top$	$[0, \pi, 0]^\top$
3	$[-0.120, 0.220, -0.065]^\top$	$[0, \pi, 0]^\top$
4	$[-0.240, 0.220, -0.065]^\top$	$[0, 0, \frac{\pi}{4}]^\top$
5	$[-0.240, -0.220, -0.065]^\top$	$[0, 0, -\frac{\pi}{4}]^\top$
6	$[-0.120, -0.220, -0.065]^\top$	$[0, \pi, 0]^\top$
7	$[0.120, -0.220, -0.065]^\top$	$[0, \pi, 0]^\top$
8	$[0.238, -0.220, -0.065]^\top$	$[0, 0, -\frac{3\pi}{4}]^\top$

3. **Transform the force component expressed in each thruster frame to apply in the body frame**

Using (5.3-5.4), and inserting the numerical values from (5.10), gives

$$\boldsymbol{\tau}^b = \sum_{i=1}^N \frac{1}{T_S + 1} \begin{bmatrix} c\psi_{p_i} c\theta_{p_i} \\ s\psi_{p_i} c\theta_{p_i} \\ -s\theta_{p_i} \\ -y_{p_i}^b s\theta_{p_i} - z_{p_i}^b s\psi_{p_i} c\theta_{p_i} \\ z_{p_i}^b c\psi_{p_i} c\theta_{p_i} + x_{p_i}^b s\theta_{p_i} \\ x_{p_i}^b s\psi_{p_i} c\theta_{p_i} - y_{p_i}^b c\psi_{p_i} c\theta_{p_i} \end{bmatrix} u_i \quad (5.11)$$

By inserting the numerical values of the location of each thruster from Table 5.1, it can be seen that the system can be written on the following equivalent

form

$$\tau^b = \frac{1}{Ts + 1} \underbrace{\begin{bmatrix} -0.71 & 0.00 & 0.00 & 0.71 & 0.71 & 0.00 & 0.00 & -0.71 \\ 0.71 & 0.00 & 0.00 & 0.71 & -0.71 & 0.00 & 0.00 & -0.71 \\ 0.00 & -1.00 & -1.00 & 0.00 & 0.00 & -1.00 & -1.00 & 0.00 \\ 0.05 & -0.22 & -0.22 & 0.05 & -0.05 & 0.22 & 0.22 & -0.05 \\ 0.05 & 0.12 & -0.12 & -0.05 & -0.05 & -0.12 & 0.12 & 0.05 \\ 0.32 & 0.00 & 0.00 & -0.33 & 0.33 & 0.00 & 0.00 & -0.32 \end{bmatrix}}_{\mathbf{B}} \mathbf{u} \quad (5.12)$$

where  $\mathbf{B}$  is the input matrix, and  $\mathbf{u} = [u_1, u_2, \dots, u_8]^T$  are the control inputs.

#### 4. Find the inverse mapping from resultant forces expressed in the body frame to the control inputs

If one neglects the first-order dynamic term, it can be seen that (5.12) fulfills all the requirements of (5.6-5.8). Hence the inverse mapping can be found by using (5.9), and the final control allocation system for Beluga NTNU consequently becomes

$$\mathbf{u} = \underbrace{\begin{bmatrix} -0.35 & 0.35 & 0.00 & 0.00 & 0.00 & 0.77 \\ 0.14 & 0.07 & -0.25 & -1.14 & 2.10 & 0.00 \\ -0.14 & 0.07 & -0.25 & -1.14 & -2.10 & 0.00 \\ 0.35 & 0.35 & 0.00 & 0.00 & 0.00 & -0.77 \\ 0.35 & -0.35 & 0.00 & 0.00 & 0.00 & 0.77 \\ -0.14 & -0.07 & -0.25 & 1.14 & -2.10 & 0.00 \\ 0.14 & -0.07 & -0.25 & 1.14 & 2.10 & 0.00 \\ -0.35 & -0.35 & 0.00 & 0.00 & 0.00 & -0.77 \end{bmatrix}}_{\mathbf{B}^\dagger} \tau_c \quad (5.13)$$

### 5.1.2 Control force error optimization

Complications might occur if one carelessly tries to use the inverse mapping of the control allocation system without considering the control input limitations. One such situation can be demonstrated by the following example.

Lets consider the control input limits are defined as  $u_i \in [-10.5, 10.5] \forall i$ , identical to (3.65). Now lets assume that the higher-level control system tries to pass the following control forces through the control allocation system of (5.13), as such

$$\underbrace{\begin{bmatrix} -27.6 \\ 13.7 \\ -13.7 \\ 27.7 \\ 43.1 \\ -13.7 \\ 13.7 \\ -43.0 \end{bmatrix}}_{\mathbf{u}_{\text{unsat}}} = \underbrace{\begin{bmatrix} -0.35 & 0.35 & 0.00 & 0.00 & 0.00 & 0.77 \\ 0.14 & 0.07 & -0.25 & -1.14 & 2.10 & 0.00 \\ -0.14 & 0.07 & -0.25 & -1.14 & -2.10 & 0.00 \\ 0.35 & 0.35 & 0.00 & 0.00 & 0.00 & -0.77 \\ 0.35 & -0.35 & 0.00 & 0.00 & 0.00 & 0.77 \\ -0.14 & -0.07 & -0.25 & 1.14 & -2.10 & 0.00 \\ 0.14 & -0.07 & -0.25 & 1.14 & 2.10 & 0.00 \\ -0.35 & -0.35 & 0.00 & 0.00 & 0.00 & -0.77 \end{bmatrix}}_{\mathbf{B}^\dagger} \underbrace{\begin{bmatrix} 100.0 \\ 0.0 \\ 0.0 \\ 0.0 \\ 0.0 \\ 0.0 \\ 10.0 \end{bmatrix}}_{\tau_c} \quad (5.14)$$

Here one can see that the resulting control inputs clearly violates the control input limitations as defined above. The actual values of the control inputs given to the

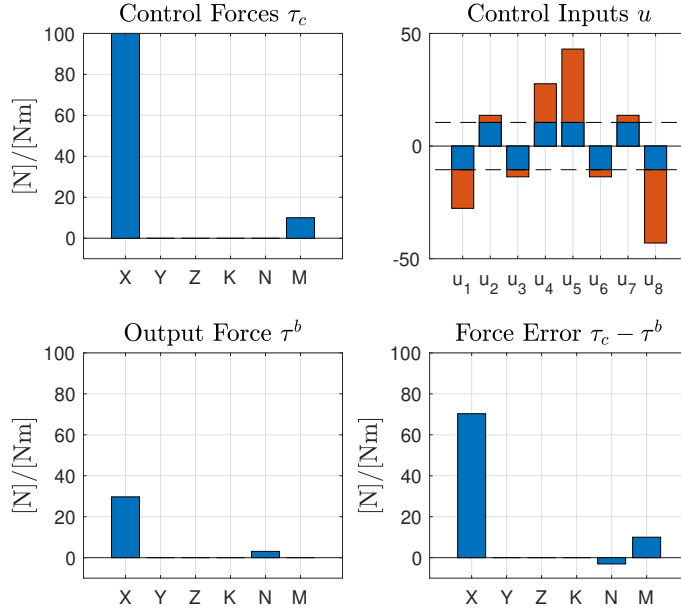


Figure 5.2: Control allocation when saturation on the control inputs are active

low-level actuator control system are therefore expected to be saturated by their saturation limits. By saturating the control inputs, and computing the expected output force gives the following result

$$\underbrace{\begin{bmatrix} 29.7 \\ 0 \\ 0 \\ 0 \\ 0 \\ 3.07 \\ 0 \end{bmatrix}}_{\tau^b} = \underbrace{\begin{bmatrix} -0.71 & 0.00 & 0.00 & 0.71 & 0.71 & 0.00 & 0.00 & -0.71 \\ 0.71 & 0.00 & 0.00 & 0.71 & -0.71 & 0.00 & 0.00 & -0.71 \\ 0.00 & -1.00 & -1.00 & 0.00 & 0.00 & -1.00 & -1.00 & 0.00 \\ 0.05 & -0.22 & -0.22 & 0.05 & -0.05 & 0.22 & 0.22 & -0.05 \\ 0.05 & 0.12 & -0.12 & -0.05 & -0.05 & -0.12 & 0.12 & 0.05 \\ 0.32 & 0.00 & 0.00 & -0.33 & 0.33 & 0.00 & 0.00 & -0.32 \end{bmatrix}}_B \underbrace{\begin{bmatrix} -10.5 \\ 10.5 \\ -10.5 \\ 10.5 \\ 10.5 \\ -10.5 \\ 10.5 \\ -10.5 \end{bmatrix}}_{u^{sat}} \tag{5.15}$$

These steps are also visually demonstrated in Figure 5.2. It is not surprising that the force output is different from the control force ( $\tau_c \neq \tau_b$ ). However the resulting error values are worth noticing. Even though a moment is desired in yaw, the output force gives no moment in yaw. In addition there is a moment given in pitch which might be undesirable when maneuvering based on zero-mean pitch assumptions. Consequently, this thesis will propose an optimization setup that enables prioritizing entities of the control force such that undesirable errors can partially be avoided.

### Proposition

For this part, let's denote the desired control forces from the higher-level control system as  $\boldsymbol{\tau}_{inf}$  (infeasible), and a set of feasible control forces as  $\boldsymbol{\tau}_f$  (feasible). A quadratic program can then be formulated as finding a set of feasible control forces that minimizes a weighted squared error between the input control forces and the feasible control forces, where the feasible control forces are subject to the bounds on the control inputs. That is

$$\text{minimize } \frac{1}{2} (\boldsymbol{\tau}_f - \boldsymbol{\tau}_{inf})^\top \mathbf{W} (\boldsymbol{\tau}_f - \boldsymbol{\tau}_{inf}) \quad (5.16)$$

$$\text{subject to } \mathbf{u}_{min} \leq \mathbf{B}^\dagger \boldsymbol{\tau}_f \leq \mathbf{u}_{max} \quad (5.17)$$

where

$\boldsymbol{\tau}_f \in \mathbb{R}^{n=6}$  are the feasible control forces.

$\boldsymbol{\tau}_{inf} \in \mathbb{R}^{n=6}$  are the input control forces.

$\mathbf{W} \in \mathbb{R}^{n \times n=6 \times 6}$  is a diagonal matrix with weights on the control force error.

$\mathbf{u}_{min} \in \mathbb{R}^r$  are the lower bounds on the control inputs.

$\mathbf{u}_{max} \in \mathbb{R}^r$  are the upper bounds on the control inputs.

$\mathbf{B}^\dagger \in \mathbb{R}^{r \times n}$  are Moore–Penrose pseudoinverse of the control input matrix.

This program has similarities to a quadratic program. However, to be able to use standardized QP solvers the problem needs to be converted to a standardized quadratic program on the form

$$\min_{\mathbf{x}} \frac{1}{2} \mathbf{x}^\top \mathbf{P} \mathbf{x} \quad (5.18)$$

$$\text{subject to } \mathbf{A} \mathbf{x} \leq \mathbf{b} \quad (5.19)$$

$$\mathbf{x} \geq 0 \quad (5.20)$$

### Transforming to a standard QP

First we notice that the difference between the control forces in (5.16) is unconstrained in sign, i.e., can be positive or negative. However on standard form we need the decision variables to be strictly non-negative. Therefore we start by defining the difference of the control forces as the difference of two non-negative variables as such

$$\mathbf{y} - \mathbf{w} = \boldsymbol{\tau}_f - \boldsymbol{\tau}_{inf} \quad (5.21)$$

where  $\mathbf{y}, \mathbf{w} \geq 0$

The objective function can now be rewritten as

$$\text{minimize } \frac{1}{2} (\mathbf{y} - \mathbf{w})^\top \mathbf{W} (\mathbf{y} - \mathbf{w}) \quad (5.22)$$

Now by defining the decision variable as  $\mathbf{x} = [\mathbf{y}^\top, \mathbf{w}^\top]^\top$ , it can be seen that the objective function can be transformed into standard form as such

$$\text{minimize } \frac{1}{2} \mathbf{x}^\top \mathbf{P} \mathbf{x} \quad (5.23)$$

where

$$\mathbf{P} = \begin{bmatrix} \mathbf{W}^{6 \times 6} & -\mathbf{W}^{6 \times 6} \\ -\mathbf{W}^{6 \times 6} & \mathbf{W}^{6 \times 6} \end{bmatrix} \in \mathbb{R}^{12 \times 12} \quad (5.24)$$

The inequality in (5.17) also needs a transformation to fit the standard form. First, one can see that the inequality can be extended to include the input control forces as such

$$\mathbf{u}_{min} - \mathbf{u}_{inf} \leq \mathbf{B}^\dagger (\boldsymbol{\tau}_f - \boldsymbol{\tau}_{inf}) \leq \mathbf{u}_{max} - \mathbf{u}_{inf} \quad (5.25)$$

where

$\mathbf{u}_{inf} \in \mathbb{R}^r$  are the control inputs as a result of the infeasible control force.

Now by first multiplying the right-hand side inequality with  $-1$ , and using the decision variables defined in (5.21), the transformed inequality can be deduced as such

$$\mathbf{u}_{min} - \mathbf{u}_{inf} \leq \mathbf{B}^\dagger (\boldsymbol{\tau}_f - \boldsymbol{\tau}_{inf}) \leq \mathbf{u}_{max} - \mathbf{u}_{inf} \quad (5.26)$$

$\Leftrightarrow$

$$\begin{aligned} \mathbf{B}^\dagger (\boldsymbol{\tau}_f - \boldsymbol{\tau}_{inf}) &\leq \mathbf{u}_{max} - \mathbf{u}_{inf} \\ -\mathbf{B}^\dagger (\boldsymbol{\tau}_f - \boldsymbol{\tau}_{inf}) &\leq -(\mathbf{u}_{min} - \mathbf{u}_{inf}) \end{aligned} \quad (5.27)$$

$\Leftrightarrow$

$$\begin{aligned} \mathbf{B}^\dagger \mathbf{y} - \mathbf{B}^\dagger \mathbf{w} &\leq \mathbf{u}_{max} - \mathbf{u}_{inf} \\ -\mathbf{B}^\dagger \mathbf{y} + \mathbf{B}^\dagger \mathbf{w} &\leq -\mathbf{u}_{min} + \mathbf{u}_{inf} \end{aligned} \quad (5.28)$$

Following (5.21-5.28) it can now be seen that the quadratic program in (5.16-5.17) can be written on standard form as such

$$\min_{\mathbf{x}} \quad \frac{1}{2} \mathbf{x}^\top \mathbf{P} \mathbf{x} \quad (5.29)$$

$$\text{subject to} \quad \mathbf{A} \mathbf{x} \leq \mathbf{b} \quad (5.30)$$

$$\mathbf{x} \geq 0 \quad (5.31)$$

where

$$\mathbf{x} := [\mathbf{y}^\top, \mathbf{w}^\top]^\top \in \mathbb{R}^{12}$$

$$\mathbf{P} := \begin{bmatrix} \mathbf{W}^{6 \times 6} & -\mathbf{W}^{6 \times 6} \\ -\mathbf{W}^{6 \times 6} & \mathbf{W}^{6 \times 6} \end{bmatrix} \in \mathbb{R}^{12 \times 12}$$

$$\mathbf{A} := \begin{bmatrix} \mathbf{B}^\dagger & -\mathbf{B}^\dagger \\ -\mathbf{B}^\dagger & \mathbf{B}^\dagger \end{bmatrix} \in \mathbb{R}^{2r \times 12}$$

$$\mathbf{b} := [(\mathbf{u}_{max} - \mathbf{u}_{inf}), (-\mathbf{u}_{min} + \mathbf{u}_{inf})]^\top \in \mathbb{R}^{2r}$$

The program formulated in (5.29-5.31) can now be solved using a standard QP solver such as *quadprog*. The solution can then be used to find the feasible control forces by using (5.21). Consequently

$$\boldsymbol{\tau}_f = \boldsymbol{\tau}_{inf} + \mathbf{y} - \mathbf{w} \quad (5.32)$$

### 5.1.3 Case study: Optimizing the control force error for Beluga NTNU

To be able to apply the program of (5.29-5.31) to Beluga NTNU, the inputs of the program needs to be decided on. Beluga NTNU uses eight T200 thrusters ( $r=8$ ) and their control input saturation limits  $\mathbf{u}_{min}, \mathbf{u}_{max}$  have already been defined in (3.65). The inverse of the input matrix  $\mathbf{B}^\dagger$  was defined in (5.13), and the non-constrained input control forces  $\boldsymbol{\tau}_{inf}$  will define the resulting non-constrained control inputs  $\mathbf{u}_{inf}$  as such

$$\mathbf{u}_{inf} = \mathbf{B}^\dagger \boldsymbol{\tau}_{inf} \quad (5.33)$$

where  $\boldsymbol{\tau}_{inf}$  are the input control forces.

Now, the only parameter left to decide on is the diagonal weight matrix  $\mathbf{W}$ . By observing (5.16), one can see that the entries of  $\mathbf{W}$  will decide what control forces are prioritized when the control allocation systems fails to replicate the input control forces. Since Beluga NTNU bases its motion on zero-mean roll and pitch, providing the correct output force in roll and pitch will be of high priority to keep the AUV stable in the horizontal plane. Tracking the desired heading angle will also be prioritized over attempting to fulfill the desired linear forces. Consequently, the following weight matrix will be proposed for Beluga NTNU

$$\mathbf{W} = \text{diag}([0.1, 0.1, 0.1, 10, 10, 1.0]) \quad (5.34)$$

Now that the program is defined, infeasible control forces given as an example in (5.14) will be run through the program. Figure 5.3 illustrates the result after solving the program using *quadprog*. Comparing to Figure 5.2 a couple of observation can be made. There are no longer output errors for pitch or yaw, but the error in surge has increased. One can also see that the control inputs are no longer strictly saturated at the saturation limits.

#### Discussion

The module to optimize the control force output error seems to work as intended for the experiment covered in this case study. However the module was not thoroughly tested, and it is still unknown how the module will perform when exposed to extreme saturation errors or for a different thruster configuration. Therefore it is recommended to carry out more tests before the module is implemented in any system with confidence.

## 5.2 Motion Control

There are plenty of different motion control architectures for underwater vehicles, and different designs can be justified depending on the desired complexity, robustness, the motion control system architecture, motion control scenario and the model of the vehicle. It is also possible to have several control architectures for the same application and switching between modes depending on e.g. different maneuvering regimes or control objectives.

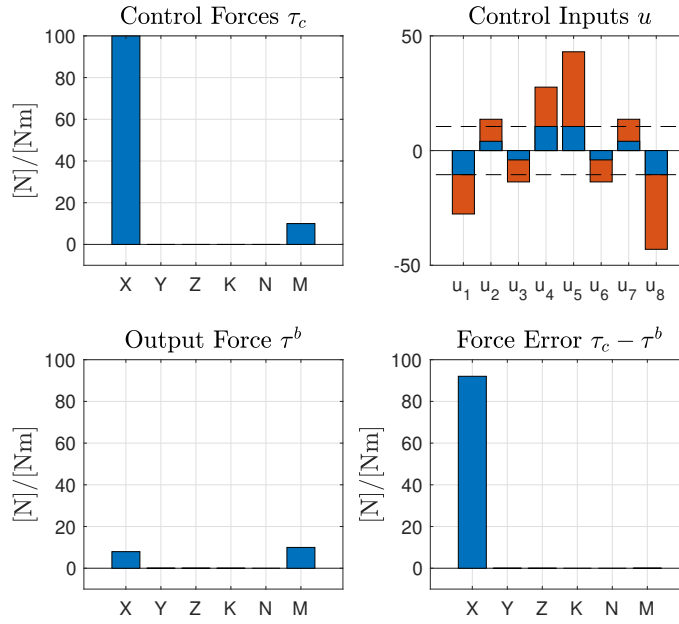


**Figure 5.3:** Control allocation by optimizing the control force error

The motion control system design in this section will be based upon the simplified low-speed maneuvering model derived in Section 3.2. The resulting equations of motion from (3.52-3.53) consist of both decoupled and linear equations w.r.t. the body frame. This opens up for using model-based SISO linear controller for each of the degrees of freedom. Therefore in Section 5.2.1 a PID-pole placement algorithm will be introduced, thereafter a dynamic-positioning controller will be developed based on SISO PID control in Section 5.2.2. Further, the roll and pitch dynamics will be regraded as open-loop stable by the design of the vehicle, thus enabling the possibility of limiting the controllable degrees of freedom to surge, sway, heave and yaw. The controller will also include reference feed-forward terms for velocity and acceleration, and the possibility for a disturbance feed-forward term for current compensation.

### 5.2.1 SISO PID pole-placement algorithm

Consider the second-order linear system

$$m\ddot{x} + d\dot{x} + kx = \tau \quad (5.35)$$

Expressing the system as a transfer function on canonical form gives

$$\frac{x}{\tau}(s) = \frac{\frac{1}{m}}{s^2 + \frac{d}{m}s + \frac{k}{m}} \quad (5.36)$$



where  $m$ ,  $d$  and  $k$  are the second-order system coefficients, and  $\tau$  is the control input.

Consider applying a PID control law with an optional feed-forward term

$$\tau = \tau_{FF} - \underbrace{\left( K_p \tilde{x} + K_d s \tilde{x} + \frac{K_i}{s} \tilde{x} \right)}_{\tau_{PID}} \quad (5.37)$$

where  $\tilde{x} = x - x_d$ .

A block diagram of the system is illustrated in Figure 5.4.

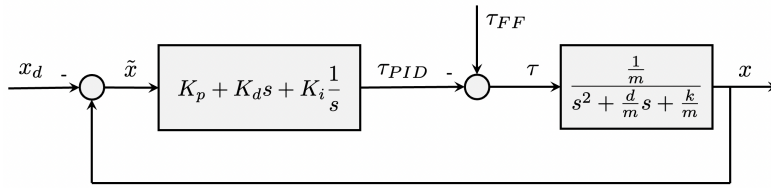


Figure 5.4: PID control of a second-order linear system

For making the closed-loop system easier to analyze the integral effect is chosen to be small and only to compensate for slowly varying disturbances. This allows for the approximation ( $K_i \approx 0$ ), and consequently the closed-loop transfer function can be expressed as

$$G(s) = \frac{x}{x_d} = \frac{\text{forward}}{1 - \text{loop}} = \frac{\left( \frac{\frac{1}{m}(K_p + K_d s)}{s^2 + \frac{d}{m}s + \frac{k}{m}} \right)}{1 - \left( -\frac{\frac{1}{m}(K_p + K_d s)}{s^2 + \frac{d}{m}s + \frac{k}{m}} \right)} = \frac{\frac{1}{m}(K_p + K_d s)}{s^2 + \frac{d + K_d}{m}s + \frac{k + K_p}{m}}. \quad (5.38)$$

By comparing the denominator of the closed-loop system to the canonical second-order system denominator

$$s^2 + 2\zeta\omega_n s + \omega_n^2 = s^2 + \frac{d + K_d}{m}s + \frac{k + K_p}{m} \quad (5.39)$$

$$\Downarrow \quad (5.40)$$

$$2\zeta\omega_n = \frac{d + K_d}{m}, \quad \omega_n^2 = \frac{k + K_p}{m} \quad (5.41)$$

it can be seen that  $K_p$  and  $K_d$  can be written as a function of  $\omega_n$  and  $\zeta$  as such

$$K_p = m\omega_n^2 - k \quad (5.42)$$

$$K_d = 2\zeta\omega_n m - d. \quad (5.43)$$

Hence by knowing the coefficients of the second-order system,  $K_p$  and  $K_d$  can be calculated by specifying the poles of the system. Now the integral action can be added to compensate for slowly varying disturbances. Writing the control law on the equivalent form

$$\tau = -K_p \left( 1 + T_d s + \frac{1}{T_i s} \right) \tilde{x} \quad (5.44)$$

the integral action can be chosen to be ten times slower than the natural frequency as such

$$\frac{1}{T_i} \approx \frac{\omega_n}{10}, \quad K_i = \frac{K_p}{T_i} \quad (5.45)$$

The expression for the integral gain then can be expressed as follows

$$K_i = \frac{\omega_n}{10} K_p = \frac{\omega_n}{10} (m \omega_n^2). \quad (5.46)$$

Further, by using the definition of control bandwidth from of a second-order system with negative unity feedback [3]

$$\omega_b = \omega_n \sqrt{1 - 2\zeta^2 + \sqrt{4\zeta^4 - 4\zeta^2 + 2}} \quad (5.47)$$

and rearranging

$$\omega_n = \frac{\omega_b}{\sqrt{1 - 2\zeta^2 + \sqrt{4\zeta^4 - 4\zeta^2 + 2}}} \quad (5.48)$$

it can be summarized that the PID gains can be decided by specifying the design parameters of the control bandwidth  $\omega_b$  and the relative damping ratio  $\zeta$ .

The PID pole-placement algorithm can now be summarized as in Algorithm 1.

---

**Algorithm 1:** PID-pole-placement algorithm for second-order linear systems

---

**Output:**  $K_p, K_d, K_i$

**Input:**  $m, d, k, \omega_b, \zeta$

$\omega_n \leftarrow$  (Equation 5.48);

$K_p \leftarrow$  (Equation 5.42);

$K_d \leftarrow$  (Equation 5.43);

$K_i \leftarrow$  (Equation 5.46);

---

## 5.2.2 Dynamic-positioning control

As the kinetic equation from (3.52-3.53) is linear, and all matrices have a diagonal structure, it can presumably be justified to use SISO PID controllers for controlling the desired degrees of freedom. The desired pose of the vehicle may however be

given w.r.t. the NED frame, therefore the transformation from (3.43) is needed when computing the error states. Consequently the following PID control law will be used

$$\boldsymbol{\tau}_{PID} = - \left( \mathbf{K}_p \mathbf{J}_\Theta(\boldsymbol{\eta})^\top (\boldsymbol{\eta} - \boldsymbol{\eta}_d) + \mathbf{K}_d (\boldsymbol{v} - \boldsymbol{v}_d) + \mathbf{K}_i \int_0^t \mathbf{J}_\Theta(\boldsymbol{\eta})^\top (\boldsymbol{\eta} - \boldsymbol{\eta}_d) \right) \quad (5.49)$$

where

$\mathbf{K}_p$ ,  $\mathbf{K}_d$  and  $\mathbf{K}_i$  are found using Algorithm 1 and (3.53).

$\mathbf{J}_\Theta(\boldsymbol{\eta}) \leftarrow$  (3.43)

$\boldsymbol{\eta}_d$  and  $\boldsymbol{v}_d$  are reference trajectories.

**Remark 5** *NB! When computing the error state for angles, e.g.,  $\tilde{\psi} = \psi - \psi_d$ , the angle should be mapped from  $-\pi$  to  $\pi$  such that the smallest error angle is the one being regulated.*

Feed-forward terms for desired velocity, acceleration, restoring forces and current compensation will also be included. The former two requires a reference model that generates smooth references which will be introduced later in Section 6.1. A method for estimating the current velocities will be also be proposed in Section 5.3. Consequently, the feed forward control law is chosen as

$$\boldsymbol{\tau}_{FF} = \mathbf{M}(\dot{\boldsymbol{v}}_d - \dot{\boldsymbol{v}}_c) + \mathbf{D}(\boldsymbol{v}_d - \boldsymbol{v}_c) + \mathbf{g}(\boldsymbol{\eta}) \quad (5.50)$$

where

$\mathbf{g}(\boldsymbol{\eta})$ ,  $\mathbf{M}$  and  $\mathbf{D}$  are the model parameters of the vehicle (3.53).

$\boldsymbol{v}_c \leftarrow$  (3.50) and  $\dot{\boldsymbol{v}}_c \leftarrow$  (3.51) are current velocities and accelerations.

$\boldsymbol{v}_d$  and  $\dot{\boldsymbol{v}}_d$  are reference trajectories.

Finally, the combined control law can be expressed as

$$\boldsymbol{\tau}_c = \boldsymbol{\tau}_{PID} + \boldsymbol{\tau}_{FF} \quad (5.51)$$

where

$\boldsymbol{\tau}_{PID} \leftarrow$  (5.49)

$\boldsymbol{\tau}_{FF} \leftarrow$  (5.50)

$\boldsymbol{\tau}_c = [X_c, Y_c, Z_c, K_c, N_c, M_c]^\top$

The roll and pitch angles are assumed to zero-mean stabilized by the restoring forces. Consequently the control force in roll and pitch will be chosen as zero ( $K_c = 0, N_c = 0$ ).

**Remark 6** *All parameters of the DP controller except for the control bandwidth  $\omega_b$ , and relative damping ratio  $\zeta$ , are based on the low-speed maneuvering model of the vehicle. Hence  $\omega_b$  and  $\zeta$  are the only tunable parameters to decide on when the model parameters of the vehicle is available.*

### 5.3 Horizontal Ocean Current Estimator

As we have already seen, the DP control law from (5.50) includes an option for current feed-forward control. The current is not assumed to be directly measured, however it should still be possible to gain information about current to improve motion control. This section proposes a method to estimate the current velocities by analyzing the relationship between change in the orientation of the vehicle, and changes in the steady state integral terms in the DP controller. The method is based on the assumption that the hydrodynamics of the vehicle is known and that the current velocity is constant and irrotational in the NED frame.

#### Proposition

By borrowing (3.47), the current velocity can be expressed w.r.t. the body frame as such

$$\mathbf{v}_c^b = \begin{bmatrix} u_c \\ v_c \\ w_c \end{bmatrix} = \begin{bmatrix} U_c \cos(\chi_c - \psi) \\ U_c \sin(\chi_c - \psi) \\ \dot{\chi}_c^n \end{bmatrix} \quad (5.52)$$

Based on the PID control law from (5.49), the goals of the integral terms are to compensate for unmodelled dynamics in the system. Now consider the system being in steady state without using current feed-forward control. The integral terms for surge, sway and heave fully should now fully reflects the force of the current acting on the vehicle, plus additional unmodelled dynamics  $d$ , as such

$$\mathbf{K}_i \int_0^t \mathbf{J}_\Theta(\boldsymbol{\eta})^\top (\boldsymbol{\eta} - \boldsymbol{\eta}_d) = \begin{bmatrix} -X_u(U_c \cos(\chi_c - \psi)) + d_u \\ -Y_v(U_c \sin(\chi_c - \psi)) + d_v \\ -Z_w \dot{\chi}_c^n + d_w \\ d_p \\ d_q \\ d_r \end{bmatrix} \quad (5.53)$$

The challenge of estimating the current velocity is that it is difficult to separate integral action as a result of current from the other unmodelled disturbances  $d$ . However this thesis proposes a solution to this problem based on assuming that the steady state non-current disturbances  $d$  are invariant and constant for changes in steady state heading angle, i.e., ( $\Delta d \approx 0$ ) for steady state sampling. Consequently, by changing heading angle and acquiring the steady state integral terms, the change in integral action should solely be a consequence of current effects. Hence, current velocities can be estimated invariant of non-current unmodelled dynamics. An attempt to explain this mathematically will now be done. By observing (5.53) and assuming steady state sampling, it can be seen that the heading angle  $\psi$  is the only variable present in the equation. By differentiating (5.53) and linearizing about the midpoint of the change in heading, gives the

following equation

$$\Delta K_i \int_0^t J_{\Theta}(\boldsymbol{\eta})^{\top} (\boldsymbol{\eta} - \boldsymbol{\eta}_d) = \begin{bmatrix} -X_u U_c \sin(\chi_c - \Delta\psi^*) \Delta\psi \\ Y_v U_c \cos(\chi_c - \Delta\psi^*) \Delta\psi \\ 0 \\ 0 \\ 0 \\ 0 \end{bmatrix} \quad (5.54)$$

where

$\Delta\psi$  is the difference in heading angle between two steady state samples.

$\Delta\psi^* := \psi_n - \frac{\Delta\psi}{2}$ , and  $\psi_n$  is the heading angle for the second of the two steady state samples.

To simplify a bit, lets use the following denotations for the difference in steady state samples for surge and sway from here on

$$\Delta(K_i \int \tilde{x}^b) = -X_u U_c \sin(\chi_c - \Delta\psi^*) \Delta\psi \quad (5.55)$$

$$\Delta(K_i \int \tilde{y}^b) = Y_v U_c \cos(\chi_c - \Delta\psi^*) \Delta\psi \quad (5.56)$$

Now it can be seen that the horizontal parameters of the current  $U_c$  and  $\chi_c$  can be expressed explicitly by solving for them in respectively (5.55-5.56). That is

$$U_c = -\frac{\Delta(K_i \int \tilde{x}^b)}{X_u \sin(\chi_c - \Delta\psi^*) \Delta\psi} \quad (5.57)$$

$$\chi_c = \arccos\left(\frac{\Delta(K_i \int \tilde{y}^b)}{Y_v U_c \Delta\psi}\right) + \Delta\psi^* \quad (5.58)$$

Inserting (5.58) into (5.57) gives

$$U_c = -\frac{\Delta(K_i \int \tilde{x}^b)}{X_u \sin\left(\arccos\left(\frac{\Delta(K_i \int \tilde{y}^b)}{Y_v U_c \Delta\psi}\right)\right) \Delta\psi} \quad (5.59)$$

By using the trigonometric identity,  $\sin(\arccos(x)) = \sqrt{1-x^2}$ , one can find the expression for the amplitude of the current velocity in the horizontal plane as

such

$$U_c = -\frac{\Delta(K_i \int \tilde{x}^b)}{X_u \sqrt{1 - \left(\frac{\Delta(K_i \int \tilde{y}^b)}{Y_v U_c \Delta\psi}\right)^2} \Delta\psi} \quad (5.60)$$

$$U_c \sqrt{1 - \left(\frac{\Delta(K_i \int \tilde{y}^b)}{Y_v U_c \Delta\psi}\right)^2} = -\frac{\Delta(K_i \int \tilde{x}^b)}{X_u \Delta\psi} \quad (5.61)$$

$$U_c^2 \left(1 - \left(\frac{\Delta(K_i \int \tilde{y}^b)}{Y_v U_c \Delta\psi}\right)^2\right) = \left(\frac{\Delta(K_i \int \tilde{x}^b)}{X_u \Delta\psi}\right)^2 \quad (5.62)$$

$$U_c^2 \left(1 - \frac{1}{U_c^2} \left(\frac{\Delta(K_i \int \tilde{y}^b)}{Y_v \Delta\psi}\right)^2\right) = \left(\frac{\Delta(K_i \int \tilde{x}^b)}{X_u \Delta\psi}\right)^2 \quad (5.63)$$

$$U_c^2 = \left(\frac{\Delta(K_i \int \tilde{x}^b)}{X_u \Delta\psi}\right)^2 + \left(\frac{\Delta(K_i \int \tilde{y}^b)}{Y_v \Delta\psi}\right)^2 \quad (5.64)$$

$$U_c = \pm \frac{1}{\Delta\psi} \sqrt{\left(\frac{\Delta(K_i \int \tilde{x}^b)}{X_u}\right)^2 + \left(\frac{\Delta(K_i \int \tilde{y}^b)}{Y_v}\right)^2} \quad (5.65)$$

Here the positive solution will be chosen since the current velocity amplitude is always defined as positive. By inserting (5.65) into (5.58) one can also find the expression for the current velocity angle in the horizontal plane as such

$$\chi_c = \arccos \left( \frac{\Delta(K_i \int \tilde{y}^b)}{Y_v \left( \pm \frac{1}{\Delta\psi} \sqrt{\left(\frac{\Delta(K_i \int \tilde{x}^b)}{X_u}\right)^2 + \left(\frac{\Delta(K_i \int \tilde{y}^b)}{Y_v}\right)^2} \right) \Delta\psi} \right) + \Delta\psi^* \quad (5.66)$$

$$= \pm \arccos \left( \frac{\frac{\Delta(K_i \int \tilde{y}^b)}{Y_v}}{\sqrt{\left(\frac{\Delta(K_i \int \tilde{x}^b)}{X_u}\right)^2 + \left(\frac{\Delta(K_i \int \tilde{y}^b)}{Y_v}\right)^2}} \right) + \Delta\psi^* \quad (5.67)$$

Here one can see that the course angle also have two solutions. Choosing the correct sign depends on being able to map the current angle to the correct half of the heading angel circle relative to the angle of estimation. This is because  $\arccos(x)$  only maps angles to  $[0, \pi]$ , whereas  $\chi_c \in [-\pi, \pi]$ . The proposed solution to this problem is to use the signum function for the change integral action for surge, as well as to correct for what direction the change of angle is. For instance, if the integral action for surge increases for a positive change in heading, the course

angle is expected to be in the negative left half circle w.r.t. the body frame. Consequently the following equation was found to provide the correct solution during later testing

$$\chi_c = -\text{sgn}\left(\Delta(K_i \int \tilde{x}^b)\right) \text{sgn}(\Delta\psi) \arccos\left(\frac{\frac{\Delta(K_i \int \tilde{y}^b)}{Y_v}}{\sqrt{\left(\frac{\Delta(K_i \int \tilde{x}^b)}{X_u}\right)^2 + \left(\frac{\Delta(K_i \int \tilde{y}^b)}{Y_v}\right)^2}}\right) + \Delta\psi^* \quad (5.68)$$

During testing another interesting relationship was found. Since the initial equation from (5.54) is based on linearization, it was found that larger changes in heading angle  $\Delta\psi$  gave an offset in the estimated current velocity amplitude from (5.65). After some experimenting, the correct estimates was found by multiplying the change in heading angle with the following function

$$f(\Delta\psi) = \frac{2}{\Delta\psi} \sin\left(\frac{\Delta\psi}{2}\right) \quad (5.69)$$

This function stems from the ratio between arc length and length of inscribed polygon in a circle. Experiments and illustrations of different values for the function are given in Figure 5.5. Further mathematical reasoning for way this seems to give the correct estimates will not be attempted. Nevertheless, the correct equation for estimating the current velocity amplitude was allegedly found to be the following

$$\begin{aligned} U_c &= \frac{1}{f(\Delta\psi)\Delta\psi} \sqrt{\left(\frac{\Delta(K_i \int \tilde{x}^b)}{X_u}\right)^2 + \left(\frac{\Delta(K_i \int \tilde{y}^b)}{Y_v}\right)^2} \\ &= \frac{1}{2 \sin\left(\frac{\Delta\psi}{2}\right)} \sqrt{\left(\frac{\Delta(K_i \int \tilde{x}^b)}{X_u}\right)^2 + \left(\frac{\Delta(K_i \int \tilde{y}^b)}{Y_v}\right)^2} \end{aligned} \quad (5.70)$$

**Remark 7** By comparing (5.70) to (5.65), and backtracking, it seems like  $(\Delta\psi)$  could have been substituted with  $\left(2 \sin\left(\frac{\Delta\psi}{2}\right)\right)$  already back in equation (5.54).

Figure 5.6 shows the implementation of the current estimator with regards to the control system. The desired heading angle will in reality pass through a reference model before it is provided to the control system, but for now this transition is illustrated by a dashed line. Finally, below is a summary of the assumptions for the estimation procedure to be well grounded.

- A1** The non-current unmodelled dynamics needs to approximate a constant value over each sample, i.e.,  $\Delta d_u \approx 0$ ,  $\Delta d_v \approx 0$ .
- A2** The hydrodynamic damping terms  $X_u, Y_v$  needs to be known, and the relative velocity of the vehicle should be within the operation points of the model during the steady state sampling.

**A3** The control forces in surge and sway also needs to accurately reflect the actual force applied on the vehicle.

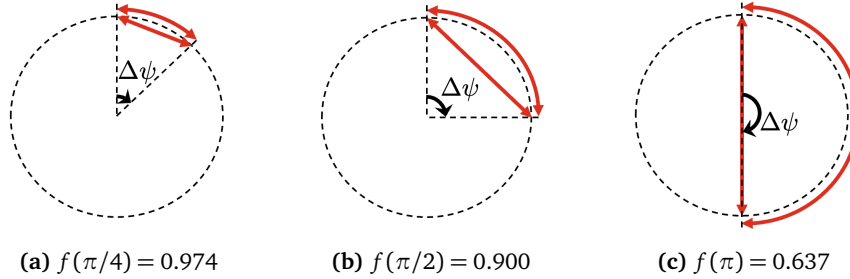


**Figure 5.5:** Illustration of different values of  $f(\Delta\psi)$

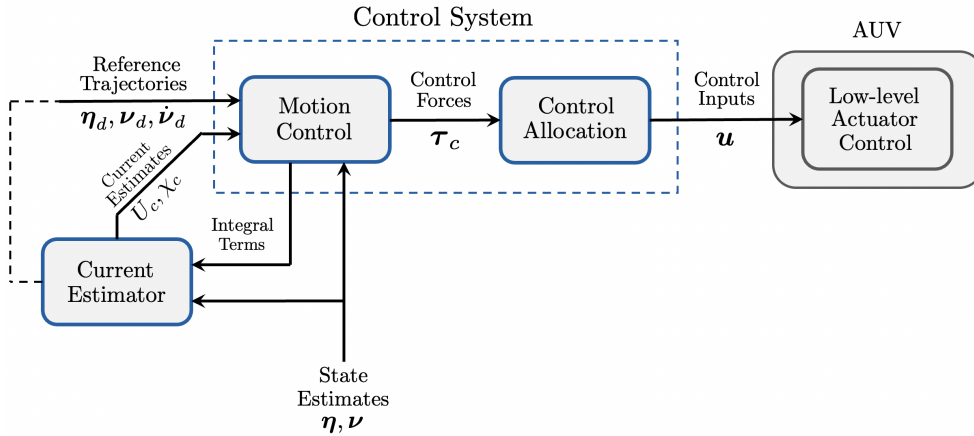


**Figure 5.6:** Illustration of the ocean current estimator implementation

## 5.4 Case Study: Simulation of the Control System and Current Estimator using Beluga NTNU

Since the current estimator requires steady state DP control and changes in heading angle, this case study will serve as both a unit test for the control system described in Section 5.1 and 5.2, and the current estimator described in Section 5.3. The experiments will be performed using the simulation testbed described in Section 4, with the model of Beluga NTNU where model and thruster parameters are attached in Appendix A. Except for irrotational constant ocean current, no model or measurement disturbances are willingly included in the experiments. However Coriolis- and centripetal forces are included in the simulator without being reflected in the control system design. There was also found a coupling between the relative velocity and the angular velocity of the heading angle which was not resolved as noted in Remark 3. Hence some structural and parametric



disturbances are present during simulation. Further, both the control system and current estimator will be blind to the unknown ocean current parameters which are

$$U_c = 0.2 \text{ [m/s]} \quad (5.71)$$

$$\chi_c = \pi/4 \text{ [rad]} \quad (5.72)$$

The parameters of the control system will further be chosen as follows:

**Control allocation system:** Beluga NTNU uses eight body-fixed thruster where the control allocation parameters was found in the case study done in Section 5.1.1.

**Motion control system:** The simplified low-speed maneuvering model parameters for Beluga NTNU is given in Appendix A. According to Remark 6, the only tunable parameters left to decide on are the control bandwidth  $\omega_b$ , and relative damping ratio  $\zeta$ , for defining the PID controller gains. These will be define as follows for the different degrees of freedom

$$\omega_b = [0.6, 0.6, 0.6, 0, 0, 0.6]^\top \quad (5.73)$$

$$\zeta = [1, 1, 1, 0, 0, 1]^\top \quad (5.74)$$

where parameters related to pitch and roll are set to zero for the sake of order.

### Case 1: Dynamic positioning under the influence of unknown ocean currents

A small step change in the desired pose  $\eta_d$  will now be given to the control system. The control system is expected to respond in a sufficiently to small step changes, at the same time as the demand for smooth trajectories can be demonstrated. Consequently the following step in the desired pose is given (also illustrated in Figure 5.7)

$$\eta_d = \begin{cases} [0, 0, 0.5, 0, 0, 0]^\top & \text{if } t < 5[s] \\ [0.25, -0.25, 0.5, 0, 0, \pi/4]^\top & \text{if } t \geq 5[s] \end{cases} \quad (5.75)$$

Figure 5.8 shows the step response of the system under the influence of unknown ocean currents from (5.71-5.72). Here one can see how the control system struggles with regulating the desired position as the relatively slow integral effect has to compensate for all the current effects as the vehicle rotates (see 3.50-3.51). The poor response in the desired position when rotating demonstrates that there is a demand for ocean current feed-forward control for underwater vehicles with rapid changes in orientation. Further one can also see that the response is less damped than the control design parameters impose. This is assumed to be caused by the step in the error states which leads to an undesired influence of the integral

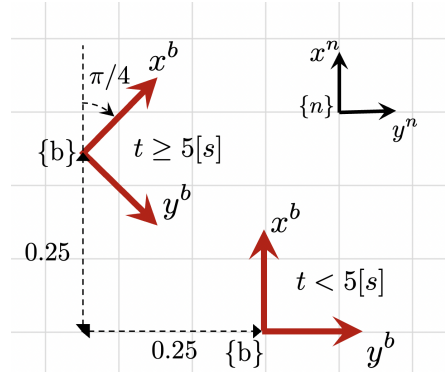


Figure 5.7: Illustration of the step change in the desired pose  $\eta_d$

action during the initial transient of the response. Since the integral action was not included in the pole placement analysis this can nevertheless be expected for step changes in reference. Also, one can observe an undesirable discontinuity in the response of the control forces. This is also a result of the discontinuity in the reference signal. Hence in the next chapter a reference model will be developed to provide smooth trajectories for the control system.

### Case 2: Estimation of the horizontal ocean current velocity

Now that a fully functioning DP-control system has been introduced, the ocean current can allegedly be estimated using (5.68), (5.70), and steady-state sampling of the integral action terms. The damping coefficients can be picked directly from the model parameters of Beluga NTNU, and the non-current integral terms will be given offset values for proof of concept. Consequently

$$X_u = -20 \quad (5.76)$$

$$Y_v = -40 \quad (5.77)$$

$$d_u = 1 \quad (5.78)$$

$$d_v = -1 \quad (5.79)$$

The steady state sampling will be performed by evaluating the Euclidean norm of the error state, and ensuring that it is below a specific threshold for a specified amount of time. More specifically the steady state evaluation criteria will be chosen as

$$\|\eta - \eta_d\|_2 < 0.05 \quad \text{for at least 5 seconds} \quad (5.80)$$

Figure 5.9 shows the results after performing the estimation procedure using four different values of changes in heading angle  $\Delta\psi$ . Here it can be seen that the estimates are quite accurate in mean estimates for different values of change in heading angle. However it can be seen that using greater change in heading angle gives more stable estimates.

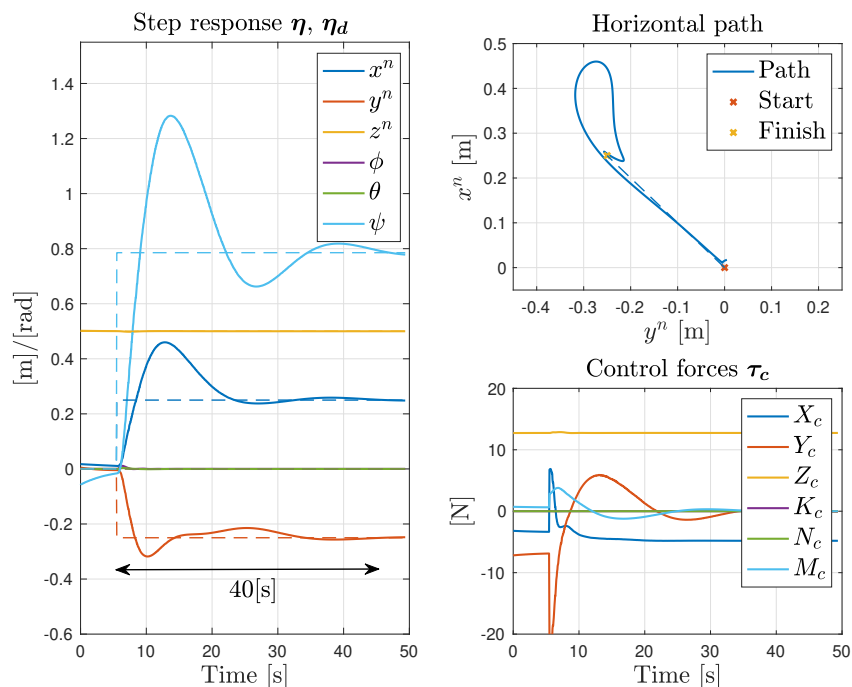


Figure 5.8: Step response under the influence of unknown ocean currents

### Case 3: Dynamic positioning using current feed-forward control

Now that ocean current estimation has been demonstrated, the control system will be simulated once more, but this time with current feed-forward control. The current velocity and acceleration can be expressed in the body frame using (3.50) and (3.51). Hence the current estimations can now be utilized in the DP-controller as described in (5.50). Figure 5.10 shows the step response of the system using current feed-forward control. Compared to the response without feed-forward control in Figure 5.8, one can see an improvement in the positional error as well as the settling time. This is because the control system now can react immediately for changes in current induced forces rather than using with the relatively slower integral effect to compensate.

### Conclusion of the case study

In this case study a DP control system using linear PID controllers and PID-pole placement algorithms for surge, sway, heave and yaw was tested in simulation together with a novel ocean current estimator. In the first experiment the control system was simulated under the influence of unknown ocean currents. Here the disadvantages of not having smooth reference trajectories and current estimations was demonstrated. In the second experiment the ocean current estimator was tested resulting in successful estimates under the circumstances of constant

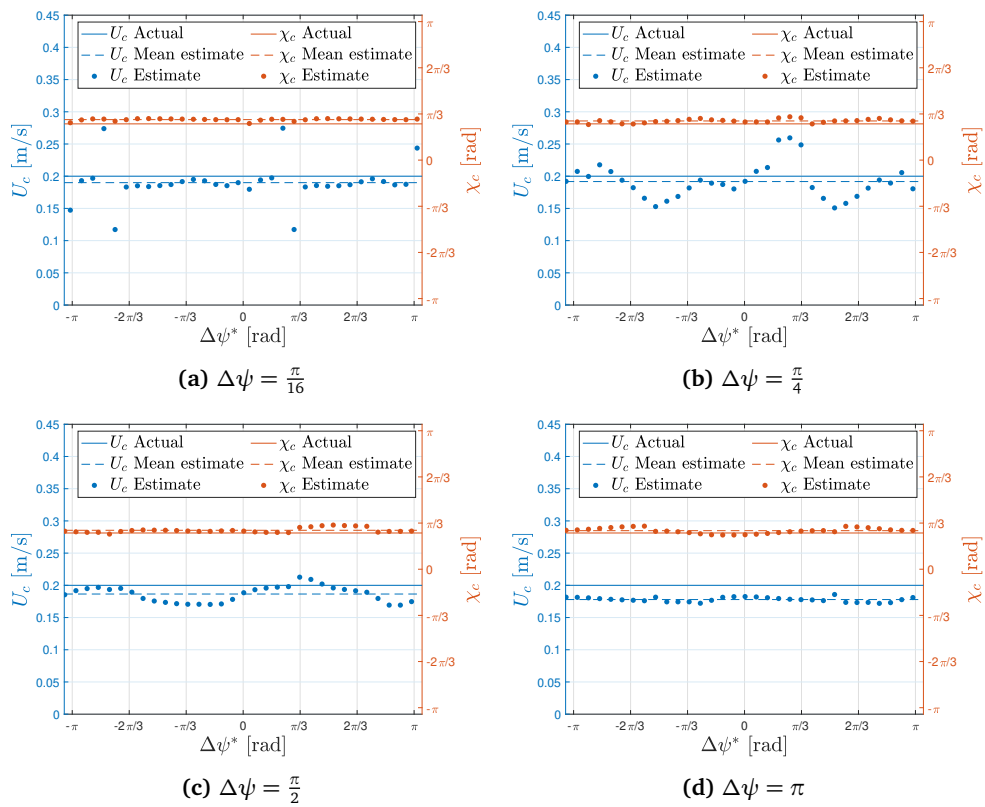


**Figure 5.9:** Current estimation using different values of  $\Delta\psi$

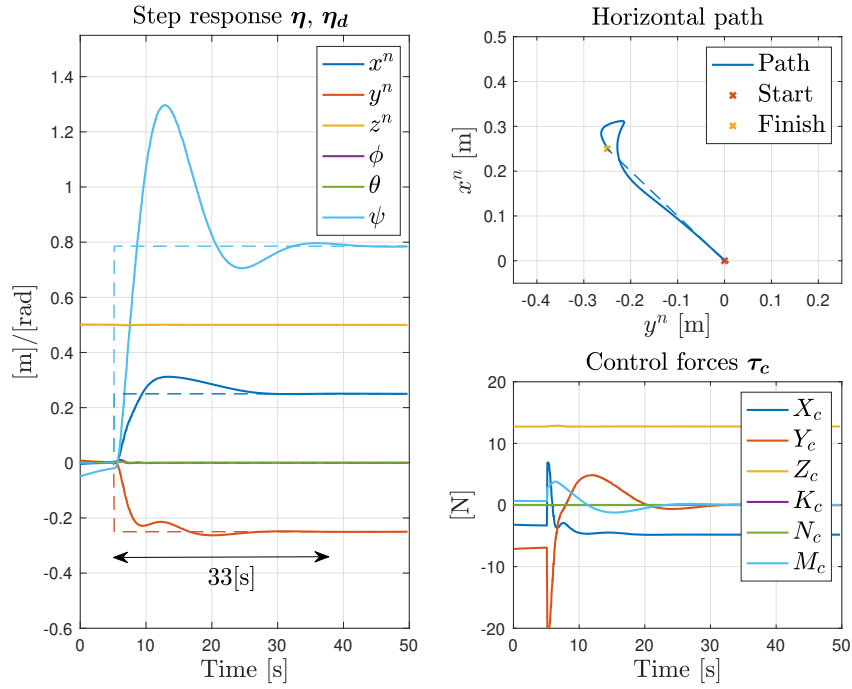


**Figure 5.10:** Step response using ocean current feed-forward control

irrotational ocean currents, sampling of steady state integral action, precise heading measurements and known hydrodynamic damper coefficients. Consequently, Research Question **R1** have been validated, under the assumptions of **A1-A3**. Finally, in the third and final experiment the value of using current feed-forward control was presented with significant improvement compared to the first experiment. Consequently it seems like further testing and usage of the ocean current estimator can provide value for fully actuated AUVs exposed to constant irrotational ocean currents.



## Chapter 6

# Guidance System

The modules of the guidance system to be considered in this chapter is illustrated in Figure 6.1. In Section 6.1, a reference model to generate smooth reference trajectories for the underlying control system will be introduced and tested. Finally in Section 6.2, a novel 3D path following controller will be presented and tested together with the reference model.

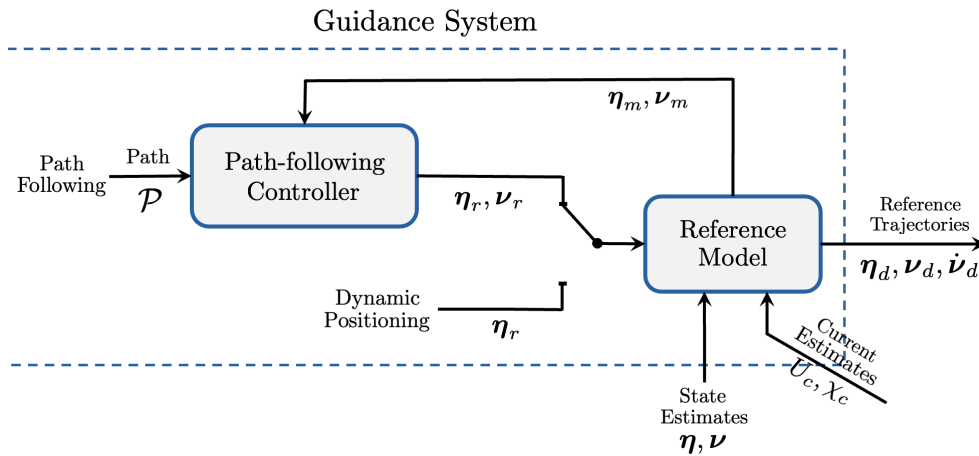


Figure 6.1: Illustration of the guidance system

### 6.1 Reference Model

In the case study done in Section 5.4, some of the implications of providing the control system with infeasible reference signals was demonstrated. It can however be convenient for the operator or higher level guidance modules to delegate kinematic actions rather than having to include trajectory planning in each individual module. Therefore a reference model to generate feasible trajectories will

be presented in Section 6.1.1, before it is tested together with the control system from Section 6.1.2.

### 6.1.1 Reference model dynamics

When generating reference trajectories is desired that the trajectories are feasible in regards to the dynamic limitations of the actual vehicle. To achieve this task it is possible to use a mathematical model of the vehicle for then to apply feasible forces into the dynamical model and use the resulting trajectories as reference. Consequently the reference model of this thesis will adopt the low-speed maneuvering model from (3.52-3.53), where the motion this time is described relative to a reference model frame  $\{m\}$ . Consequently

$$\dot{\boldsymbol{\eta}}_m = \mathbf{J}_\theta(\boldsymbol{\eta}_m) \boldsymbol{\nu}_m \quad (6.1)$$

$$\mathbf{M}(\dot{\boldsymbol{\nu}}_m - \dot{\boldsymbol{\nu}}_c) + \mathbf{D}(\boldsymbol{\nu}_m - \boldsymbol{\nu}_c) + \mathbf{g}(\boldsymbol{\eta}_m) = \boldsymbol{\tau}_c \quad (6.2)$$

where

$$\boldsymbol{\eta}_m = \begin{bmatrix} \mathbf{p}_{nm}^n \\ \boldsymbol{\Theta}_{nm} \end{bmatrix} \quad \boldsymbol{\nu}_m = \begin{bmatrix} \mathbf{v}_{nm}^m \\ \boldsymbol{\omega}_{nm}^m \end{bmatrix} \quad \dot{\boldsymbol{\nu}}_m = \begin{bmatrix} \dot{\mathbf{v}}_{nm}^m \\ \dot{\boldsymbol{\omega}}_{nm}^m \end{bmatrix} \quad (6.3)$$

NB! In this thesis all dynamics in roll and pitch will be constrained to zero. Hence effectively restricting the reference model to 4 DOF.

Now trajectories to achieve a desired pose can be generated by applying control forces to the reference model accordingly. To secure feasibility of the generated control forces the following three steps is proposed:

#### 1. Including a control law

If kinematic references are given as input to the reference model one can for instance use a closed-loop PD controller to create the desired closed-loop dynamics of the system. All terms that are expected to include in the actual control system will be included in the control law. This is so that the control forces can be generated accordingly if the control input saturation limits are in risk of being exceeded for the actual vehicle. In addition an option for open-loop velocity control will be included. Consequently the control law for the reference model will be similar to the control law from (5.49-5.51), except the removal of the integral action since no unmodelled dynamics are present. Consequently

$$\boldsymbol{\tau}_{c, inf} = \mathbf{g}(\boldsymbol{\eta}_m) - \mathbf{M} \dot{\boldsymbol{\nu}}_c + \mathbf{D}(\boldsymbol{\nu}_{ref} - \boldsymbol{\nu}_c) - (\mathbf{K}_p \mathbf{J}_\Theta(\boldsymbol{\eta}_m)^\top (\boldsymbol{\eta}_m - \boldsymbol{\eta}_{ref}) + \mathbf{K}_d (\boldsymbol{\nu}_m - \boldsymbol{\nu}_{ref})) \quad (6.4)$$

where

$\boldsymbol{\tau}_{c, inf}$  are control forces in risk of being infeasible.  
 $\boldsymbol{\eta}_{ref}$  and  $\boldsymbol{\nu}_{ref}$  are arbitrary reference trajectories.



$\mathbf{g}(\boldsymbol{\eta}_m)$ ,  $\mathbf{M}$  and  $\mathbf{D}$  are the model parameters of the vehicle (3.53).

$\mathbf{v}_c \leftarrow$  (3.50) and  $\dot{\mathbf{v}}_c \leftarrow$  (3.51) are current velocities and accelerations.

$\mathbf{K}_p$  and  $\mathbf{K}_d$  are found using Algorithm 1 and the vehicle model (3.53).

The PD gains can be found using the same PID-pole placement algorithm as the actual control system (see Section 5.2.1), but will be designed with slightly slower control bandwidth  $\boldsymbol{\omega}_b$ . This is to assure that the actual control system is able to converge to the trajectory when error dynamics are present during trajectory tracking.

## 2. Optimizing the control force error

To handle infeasible kinematic references where control force error is unavoidable, the method of optimizing the control force error (see Section 5.1.2) will be used. Consequently, after the control forces are calculated, the following program is included

$$\text{minimize } \frac{1}{2} (\boldsymbol{\tau}_{c,f} - \boldsymbol{\tau}_{c,inf})^\top \mathbf{W} (\boldsymbol{\tau}_{c,f} - \boldsymbol{\tau}_{c,inf}) \quad (6.5)$$

$$\text{subject to } \mathbf{u}_{m,min} \leq \mathbf{B}^\dagger \boldsymbol{\tau}_{c,f} \leq \mathbf{u}_{m,max} \quad (6.6)$$

where

$\boldsymbol{\tau}_{c,f}$  are the output of feasible control forces.

$\mathbf{u}_{m,b} := [\mathbf{u}_{m,min}, \mathbf{u}_{m,max}]$  are bounds on the control inputs.

$\mathbf{W}$  is the control force weight matrix.

$\mathbf{B}^\dagger$  is the Moore–Penrose pseudoinverse of the input matrix.

Here the weight matrix  $\mathbf{W}$  and inverse input matrix  $\mathbf{B}^\dagger$  are chosen as the same as for the actual control allocation system, while the control input saturation limits  $\mathbf{u}_{b,ref}$  can be set slightly lower to increase feasibility of the trajectory.

## 3. Adding dynamics to the control force

Finally constraints of the acceleration dynamics will be included by adding a low-pass filter on the control forces. That is

$$\boldsymbol{\tau}_c = \frac{1}{1 + T_{ms}} \boldsymbol{\tau}_{c,f} \quad (6.7)$$

where  $T_{ref}$  is time constant of the low-pass filter. It is recommended to set this greater than the time constant of the actual low-level actuator control system to increase feasibility.

**Remark 8** *Adding first-order dynamics to the control forces, and hence the acceleration, will in fact impact the closed-loop response of the PD controller law from 6.4. However as long as the dynamics of the thrusters are fast compared to the control law, the effect of this will be minimal.*

When using the reference model states for trajectory generation for the DP controller from Section 5.2.2, it is necessary to transform the final velocity and accelerations stated to the body frame. Consequently the desired reference trajectories

fed to the control system is chosen as

$$\boldsymbol{\eta}_d = \boldsymbol{\eta}_m \quad (6.8)$$

$$\boldsymbol{v}_d = \boldsymbol{J}_\Theta(\tilde{\boldsymbol{\eta}})\boldsymbol{v}_m \quad (6.9)$$

$$\dot{\boldsymbol{v}}_d = \boldsymbol{J}_\Theta(\tilde{\boldsymbol{\eta}})\dot{\boldsymbol{v}}_m \quad (6.10)$$

where  $\tilde{\boldsymbol{\eta}} = [0, 0, 0, 0, 0, \psi_m - \psi]^\top$ , and  $\psi_m$  is the heading angle of the reference model.

### 6.1.2 Case Study: Trajectory generation and tracking using Beluga NTNU

This case study serves as an extension of the case study from Section 5.4, but this time including the reference model for smooth trajectory generation. Therefore all parameters regarding the control system will be adopted from the previous section. Therefore only parameters regarding the reference model will be described in this case study.

As mentioned the control bandwidth for the reference model control law from (6.4) will be chosen as slightly slower than the actual control system. Consequently

$$\begin{aligned} \boldsymbol{\omega}_{b,m} &= 0.5\boldsymbol{\omega}_b & \boldsymbol{\omega}_b &\leftarrow (5.73) \\ &= 0.5 \cdot [0.6, 0.6, 0.6, 0, 0, 0.6]^\top & & (6.11) \\ &= [0.3, 0.3, 0.3, 0, 0, 0.3]^\top & & \end{aligned}$$

The relative damping ratio will be designed to make the closed-loop system critically damped. That is

$$\boldsymbol{\zeta}_m = [1, 1, 1, 0, 0, 1]^\top \quad (6.12)$$

The control input saturation limits, and time constant, will be set respectively half and double of the values of the actual system to increase feasibility. Consequently

$$\begin{aligned} \boldsymbol{u}_{b,m} &\in 0.5\boldsymbol{u}_b & \boldsymbol{u}_b &\leftarrow (3.65) \\ &\in 0.5 \cdot [-10.5, 10.5] & & (6.13) \\ &\in [-5.25, 5.25] & & \end{aligned}$$

$$\begin{aligned} T_m &= 2 \cdot T & T &\leftarrow (3.60) \\ &= 2 \cdot 0.2 & & (6.14) \\ &= 0.4 & & \end{aligned}$$

Now the similar step in reference pose from the previous case study (5.75) is provided to the reference model. Figure 6.2 shows the resulting trajectories. As one can tell, all the trajectories now are smooth functions that allegedly are feasible for trajectory tracking for the control system. In fact Figure 6.3 shows the

tracking performance of the control system using reference and current feed-forward control. When comparing to Figure 5.10, one can tell that the resulting response and control inputs has smoother transients more like what was originally desired of the control system. Hence all the problems regarding discontinuous reference signals have been solved using the proposed reference model. In regards to Remark 8, it is worth to notice how the low-pass filter on the acceleration doesn't impact the closed-loop response remarkably. Further, the error dynamics observed in the heading angle are assumed to be mainly caused by the simulation inconsistency from Remark 3.

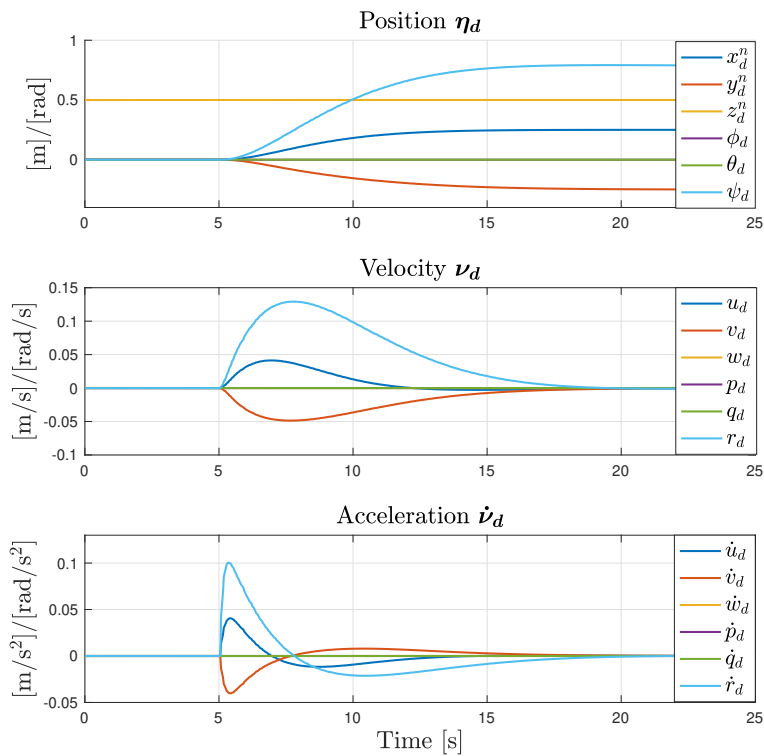
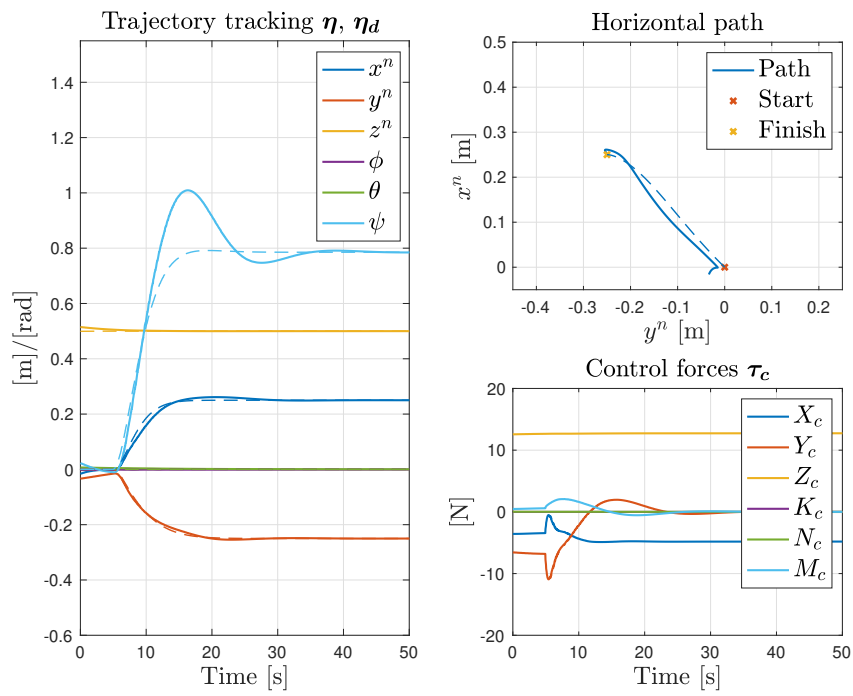


Figure 6.2: Trajectory generation using the reference model

## 6.2 3D Path Following

The last module of the guidance system for the scope of this thesis will be a path-following controller. Path following is a motion control scenario where the control objective is to converge to, and follow a path, without any temporal constraints along the path. The absence of temporal constraints aims to remove possible situations where the vehicle have to catch up to a point on the path, which essentially might be infeasible, or might require a shortcut. Hence, in path following scen-



**Figure 6.3:** Trajectory tracking using ocean current and reference feed-forward control

arios, the objective of staying on the path is usually regarded as the higher priority rather than the time span of the operation.

To solve the path following problem a virtual target will be defined to evolve along the path to provide the reference trajectories for the reference model. Path following can in this case be achieved by having the reference model to converge to the virtual target, which then starts guiding the reference model along the path. Its therefore advantageous if the along-track speed of the virtual target is adaptable such that the dynamical constraints of the actual vehicle is partially reflected in the motion of the virtual target. For instance if the reference model starts to lag behind, it is convenient if the virtual adapts its velocity accordingly.

Now some basic path definitions and representation will be introduced in Section 6.2.1 and 6.2.2, respectively. Thereafter a path following controller based on a virtual target evolving with an optimized along-track speed will be proposed in Section 6.2.3. Finally in Section 6.2.4, a case study testing the path following controller together with the reference model will be presented.

### 6.2.1 Path definitions

A path in three-dimensional Euclidean space is a one-dimensional manifold that can be expressed by the set

$$\mathcal{P} := \{\mathbf{p} \in \mathbb{R}^3 \mid \mathbf{p} = \mathbf{p}_p(\varpi) \forall \varpi \in \mathbb{R}\} \quad (6.15)$$

where  $\varpi$  is the path parameter and  $\mathbf{p}_p(\varpi)$  denotes a point in the three-dimensional Euclidean space belonging to the path. Hence

$$\mathbf{p}_p(\varpi) = \begin{bmatrix} x_p^n(\varpi) \\ y_p^n(\varpi) \\ z_p^n(\varpi) \end{bmatrix} \quad (6.16)$$

For any point along the path, the path-tangential reference frame is rotated a horizontal and a vertical angle relative to NED. The angles can be found using  $\text{atan2}$  on the first derivatives as such

$$\chi_p = \text{atan2}(y_p^n(\varpi)', x_p^n(\varpi)') \quad (6.17)$$

$$\gamma_p = -\text{atan2}(z_p^n(\varpi)', \sqrt{(x_p^n(\varpi)')^2 + (y_p^n(\varpi)')^2}) \quad (6.18)$$

The rotation from the path-tangential reference frame to the NED frame will consequently be defined as

$$\mathbf{R}(\Theta_{np}) := \mathbf{R}_z(\chi_p) \mathbf{R}_y(\gamma_p) \quad (6.19)$$

where  $\Theta_{np} = [\chi_p, \gamma_p, 0]$

Following the definitions in [22],  $\mathbf{p}(\cdot)$  is usually defined as a piecewise-defined function, which reduces the function complexity but demands consideration at the transition points between subpaths. The subpaths will be expressed by the set

$$\mathcal{P}_i := \{\mathbf{p}_i \in \mathbb{R}^3 \mid \mathbf{p}_i = \mathbf{p}_{i,p}(\varpi) \forall \varpi \in \mathcal{I}_i = [\varpi_{i,0}, \varpi_{i,1}] \subset \mathbb{R}\} \quad (6.20)$$

and the path can then finally be expressed as a super set of the sub paths as such

$$\mathcal{P}_s = \bigcup_{i=1}^n \mathcal{P}_i \quad (6.21)$$

## 6.2.2 Path representations

### Straight lines

A path from A to B in its simplest form can be expressed by a straight line. By using the parametric form as in [23], but extending to three dimension, the following straight line parametrization can be used

$$\mathbf{p}_{\text{line}}(\varpi) = \begin{bmatrix} N_0 + L\varpi \cos(\chi_l) \cos(\gamma_l) \\ E_0 + L\varpi \sin(\chi_l) \cos(\gamma_l) \\ D_0 - L\varpi \sin(\gamma_l) \end{bmatrix} \quad (6.22)$$

where

$\mathbf{p}_0 = [N_0, E_0, D_0]$  is the starting point.

$L$  is the length of the line.

$\chi_l$  and  $\gamma_l$  are the tangential angles of the straight line.

Figure 6.4 illustrates a path consisting of only straight lines. A couple of remarks can be made by observing the figure. The path tangential angles are discontinuous, and the curvature cannot be defined at the vertices. Therefore such paths will require a full stop-start maneuver at each vertex to prevent a drift off the path during turning. This type of maneuver is however not energy or time efficient. Despite its path simplicity, straight lines with vertices will therefore likely result in either poor path following precision or high energy consumption. This undesirable trade off motivates for the introduction of curved arcs.

### Curved arcs

Curved arcs can be parametrized for the horizontal dimensions as such

$$\mathbf{p}_{\text{cir}}(\varpi) = \begin{bmatrix} c_N + R_h \cos(\chi_0 + \varpi(\chi_1 - \chi_0)) \\ c_E + R_h \sin(\chi_0 + \varpi(\chi_1 - \chi_0)) \end{bmatrix} \quad (6.23)$$

where

$c_N$  and  $c_E$  are the center of the circle which the arc is a segment of.

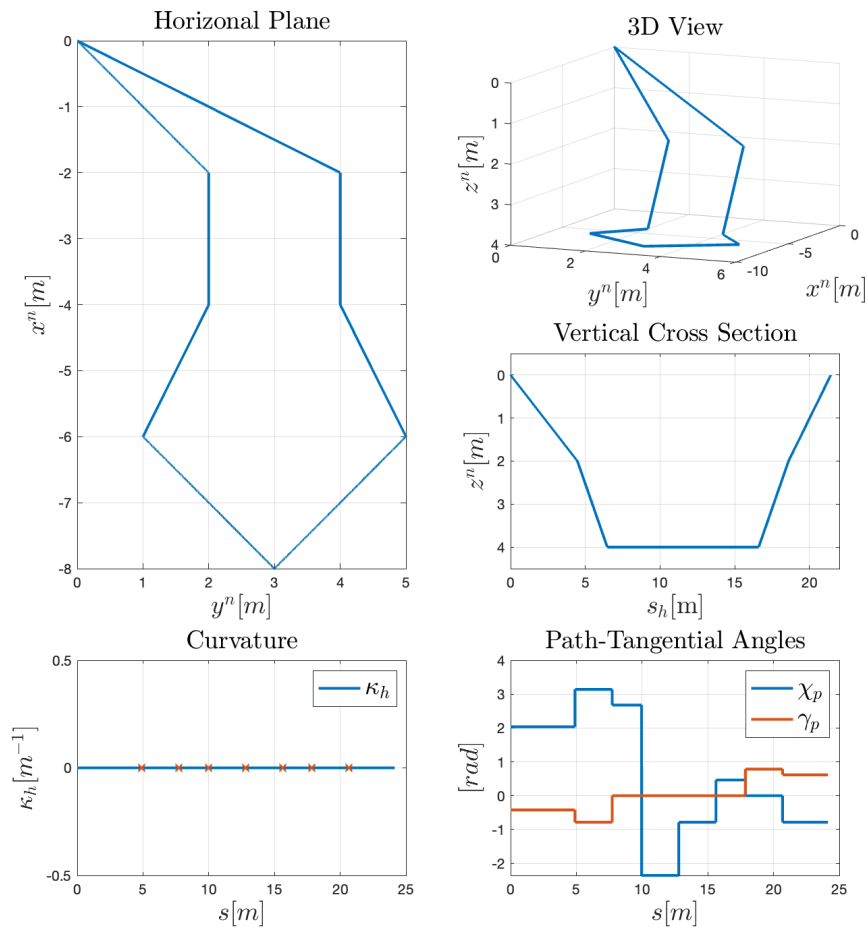


Figure 6.4: Path consisting of only straight lines

$\chi_0$  and  $\chi_1$  are the tangential-angles at which the arc starts and ends.  
 $R_h$  is the radius of the arcs.

The curvature of the arc can be defined by

$$\kappa_h = \frac{1}{R_h} \quad (6.24)$$

and the required acceleration to stay on the curved path with a non-zero velocity vector can be described by [24]

$$|\mathbf{a}| = |\mathbf{u}|^2 \kappa \quad (6.25)$$

where  $\mathbf{a}$  is the lateral acceleration vector, and  $\mathbf{u}$  is the velocity vector.

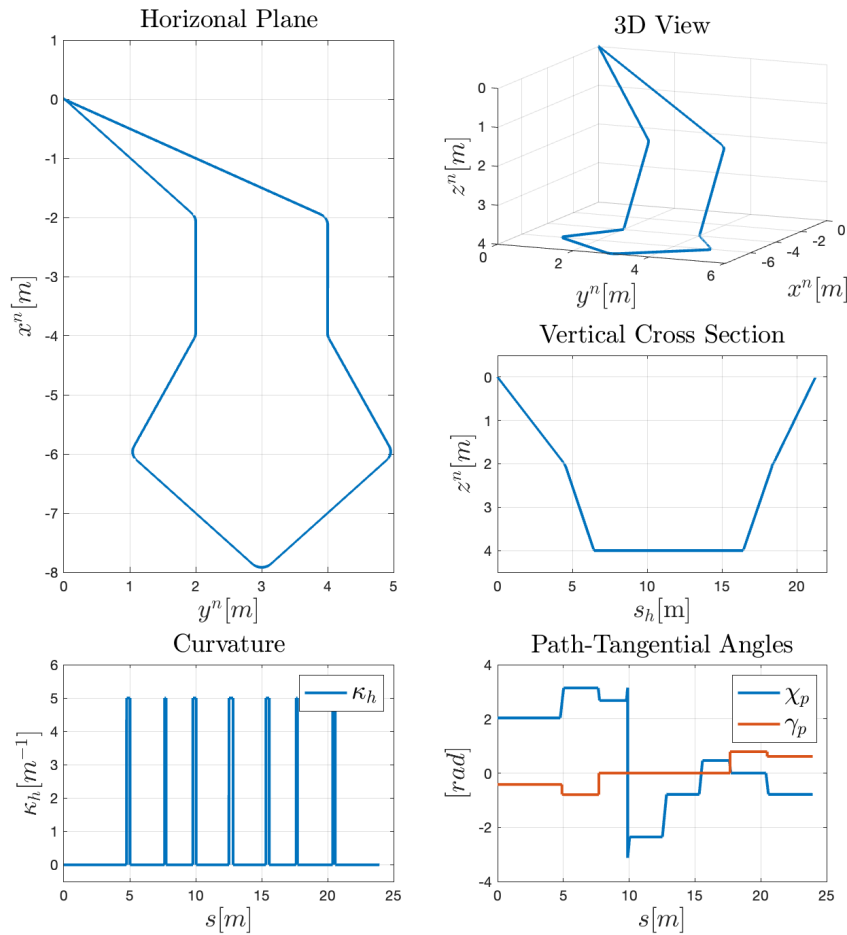


Figure 6.5: Path consisting of straight lines and curved arcs



Since the underwater vehicle considered in this thesis have zero-mean roll and pitch angle, the vertical dimension is only coupled with an heave. Therefore straight lines in the vertical dimension will be regarded as sufficient path smoothness. The horizontal dimensions are however coupled between surge, sway and yaw (see (3.43)), therefore curved path segments can be preferred. Figure 6.5 illustrates a path consisting of straight lines connected by circular arcs in the horizontal plane. Here one can observe that the horizontal path-tangential angle now is continuous, and that the horizontal curvature can be defined at all points along the path. However, it can be seen that the curvature will be discontinuous at the transition between a straight line and a circular arc. Further, (6.25) shows that at these transitions the vehicle needs zero velocity or a discontinuous jump in acceleration for perfect path following precision. However, this is not considered to be a considerable problem for the low-speed maneuvering case. Hence a  $G_1$  path in the horizontal plane will be regarded as sufficient for demonstrating the path-following application in this thesis. For a more thoroughly discussion on path evaluation criteria the reader is referred to [25].

### 6.2.3 Path-following control based on controlling a virtual target

The objective of the virtual target is to provide the reference model with reference trajectories constrained to move along the path. The distance propagated along the path will be denoted  $s$ , and the along-track speed will consequently be denoted  $\dot{s}$ . The virtual target will be provided with a reference frame  $\{t\}$ , where the orientation will be defined with a heading angle, but constrained with zero roll and pitch dynamics. Hence giving the virtual target 4 DOF. Figure 6.6 shows an illustration of the virtual target in the horizontal plane, and in the vertical cross section of the path.

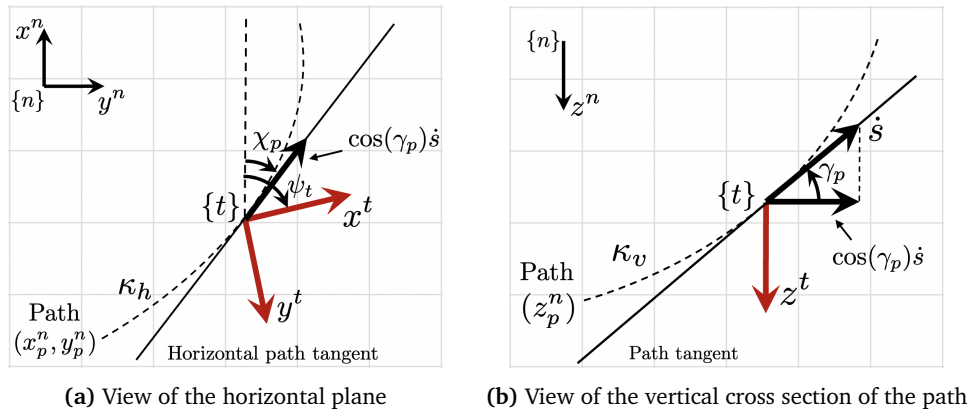


Figure 6.6: Illustration of the virtual target reference frame

Before defining the dynamics of the virtual target it is convenient to first define the path-tangential derivatives. By observing the 6.6, and assuming that the curvature

is defined, one can use (2.8) to define the path-tangential derivatives as such

$$\dot{\chi}_p = \kappa_h \cos(\gamma_p) \dot{s} \quad (6.26)$$

$$\dot{\gamma}_p = \kappa_v \dot{s} \quad (6.27)$$

### Virtual target position and orientation

The position of the virtual target is described w.r.t. the inertial frame, and can naturally be expressed as a point somewhere on the path, i.e.,  $\mathbf{p}_{nt}^n = \mathbf{p}_{np}^n(\varpi)$ . The roll and pitch angles will be chosen equal to zero, while the heading angle can be chosen arbitrarily for a vehicle with actuation in both surge and sway. Consequently the virtual target position and orientation will be described as

$$\boldsymbol{\eta}_t = \begin{bmatrix} \mathbf{p}_{nt}^n \\ \boldsymbol{\Theta}_{nt} \end{bmatrix} = \begin{bmatrix} x_p^n(\varpi) \\ y_p^n(\varpi) \\ z_p^n(\varpi) \\ 0 \\ 0 \\ \psi_t \end{bmatrix} \quad (6.28)$$

where  $\psi_t$  is the virtual target heading angle. Figure 6.7 shows two different choices of heading angle to be demonstrated in this thesis. Defining the heading angle will in fact be of importance when defining its derivative when moving along the path.

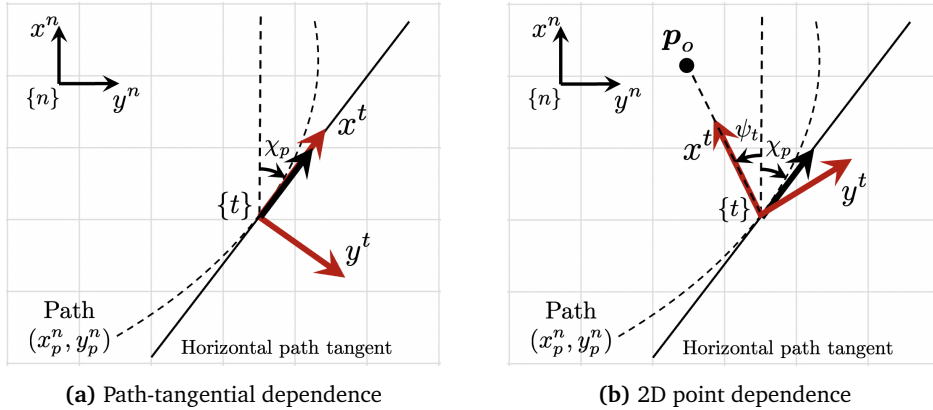


**Figure 6.7:** Illustration of two different choices of heading angle for the virtual target

#### (i) The heading angle is guided by the horizontal path tangent

It is often desired that the heading angle of the vehicle is aligned with the horizontal path-tangential angle, for instance when it is desired to minimize motion in sway, or optimizing the crab angle. This case is illustrated in Figure 6.7a, where the heading angle can be chosen as

$$\psi_t = \chi_p \quad (6.29)$$

(ii) **The heading angle is guided by a point in the horizontal plane**

It can also be desired that the vehicle has its sensors angled toward a point of interest while following the path. This case is illustrated in Figure 6.7b. Here the heading angle will depend on a point relative to the vehicle in the horizontal plane. Here one can see that the heading angle of the virtual target can be found by using the atan2()-function on the horizontal position of the vehicle, and the 2D point, as such

$$\psi_t = \text{atan2}(y_o - y_t, x_o - x_t) \quad (6.30)$$

**Virtual target linear and angular velocities**

Since the virtual target is constrained to move along a one-dimensional manifold, it can be shown that its velocity will only vary with the along track-speed  $\dot{s}$ . The along-track speed is defined along the  $x$  axis of the path tangential reference frame  $\{p\}$ , which is partly illustrated in Figure 6.6b. Therefore a transformation is needed to be able to express the virtual target velocity in the virtual target frame  $\{t\}$ . This can be done by first rotating from  $\{p\}$  to  $\{n\}$ , by using the rotation matrix defined in (6.19). Thereafter a rotation from  $\{n\}$  to  $\{t\}$  can be obtained by using the transpose of the rotation matrix defined by the orientation given in (6.28). The linear velocities of the virtual target can consequently be described as

$$\mathbf{v}_{nt}^t = \mathbf{R}(\Theta_{nt})^\top \mathbf{R}(\Theta_{np}) \begin{bmatrix} 1 \\ 0 \\ 0 \end{bmatrix} \dot{s} \quad (6.31)$$

$$\mathbf{v}_{nt}^t = \begin{bmatrix} (\cos(\psi_t) \cos(\chi_p) + \sin(\psi_t) \sin(\chi_p)) \cos(\gamma_p) \\ (\cos(\psi_t) \sin(\chi_p) - \sin(\psi_t) \cos(\chi_p)) \cos(\gamma_p) \\ -\sin(\gamma_p) \end{bmatrix} \dot{s} \quad (6.32)$$

$$= \begin{bmatrix} \cos(\chi_p - \psi_t) \cos(\gamma_p) \\ \sin(\chi_p - \psi_t) \cos(\gamma_p) \\ -\sin(\gamma_p) \end{bmatrix} \dot{s} \quad (6.33)$$

The angular velocity can be found by using (3.14). Consequently, for zero roll and pitch dynamics this becomes

$$\boldsymbol{\omega}_{nt}^t = \underbrace{\mathbf{T}(\Theta_{nt})^{-1}}_{\mathbf{I}_3} \begin{bmatrix} 0 \\ 0 \\ \dot{\psi}_t \end{bmatrix} = \begin{bmatrix} 0 \\ 0 \\ \dot{\psi}_t \end{bmatrix} \quad (6.34)$$

The derivative of the heading angle depends on the choice of heading angle. Continuing with the two examples from Figure (6.7), their derivatives can be derived as such

(i) **The heading angle is guided by the horizontal path-tangential angle**

By using (6.26), the time derivative can simply be derived as such

$$\dot{\psi}_t = \dot{\chi}_p \quad (6.35)$$

$$= \kappa_h \cos(\gamma_p) \dot{s} \quad (6.36)$$

where

$\kappa_h$  is the horizontal path curvature.

$\gamma_p$  is the vertical path-tangential angle.

$\dot{s}$  is the along-track speed.

(ii) **The heading angle is guided by a point in the horizontal plane**

Figure 6.8 shows how the derivative of the heading angle can be found under the assumption that the approximate Euclidean horizontal distance to the point of interest is known.

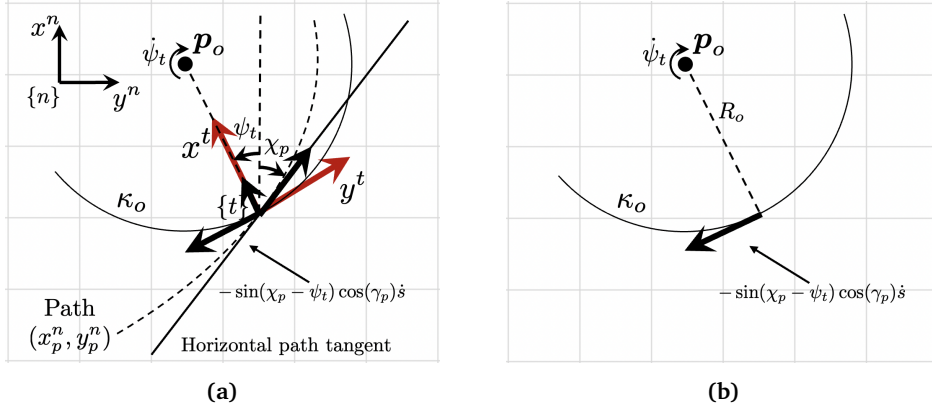


**Figure 6.8:** Illustration of how to find the time derivative of a heading angle guided by a point in the horizontal plane

In (6.8a), a circle is first defined with the point in the center, and a radius equal to the Euclidean horizontal distance between the point and the virtual target. The horizontal tangential speed is decomposed into the tangential speed along the circle illustrated in (6.8b). By using the relationship defined in (2.8), the time derivative of the heading angle can now be expressed as such

$$\dot{\psi}_t = -\kappa_o \sin(\chi_p - \psi_t) \cos(\gamma_p) \dot{s} \quad (6.37)$$

where

$$\kappa_o = \frac{1}{R_o} = \frac{1}{d((x_o, y_o), (x_t, y_t))} \quad (6.38)$$

and  $d((x_o, y_o), (x_t, y_t))$  is the Euclidean distance between the point and the virtual target in the horizontal plane.

The virtual target velocity can now be expressed as

$$\mathbf{v}_t = \begin{bmatrix} \mathbf{v}_{nt}^t \\ \boldsymbol{\omega}_{nt}^t \end{bmatrix} = \begin{bmatrix} \cos(\chi_p - \psi_t) \cos(\gamma_p) \dot{s} \\ \sin(\chi_p - \psi_t) \cos(\gamma_p) \dot{s} \\ -\sin(\gamma_p) \dot{s} \\ 0 \\ 0 \\ \dot{\psi}_t \end{bmatrix} \quad (6.39)$$

Inserting the two different versions of the heading angle gives

$$(i) \mathbf{v}_t = \begin{bmatrix} \mathbf{v}_{nt}^t \\ \boldsymbol{\omega}_{nt}^t \end{bmatrix} = \begin{bmatrix} \cos(\gamma_p) \dot{s} \\ 0 \\ -\sin(\gamma_p) \dot{s} \\ 0 \\ 0 \\ \kappa_h \cos(\gamma_p) \dot{s} \end{bmatrix} \quad (6.40)$$

$$(ii) \mathbf{v}_t = \begin{bmatrix} \mathbf{v}_{nt}^t \\ \boldsymbol{\omega}_{nt}^t \end{bmatrix} = \begin{bmatrix} \cos(\chi_p - \psi_t) \cos(\gamma_p) \dot{s} \\ \sin(\chi_p - \psi_t) \cos(\gamma_p) \dot{s} \\ -\sin(\gamma_p) \dot{s} \\ 0 \\ 0 \\ -\kappa_o \sin(\chi_p - \psi_t) \cos(\gamma_p) \dot{s} \end{bmatrix} \quad (6.41)$$

where  $\psi_t = \text{atan2}(x_o - x_t, y_o - y_t)$

It is also possible to further derive the virtual target acceleration by time differentiating the velocities. This will however not be done for this thesis as the increased complexity is not considered to justify its presumably small effect on the path following performance under low-speed maneuvering.

### Optimizing the along-track speed

The first path-following objective of converging to the path can now simply be achieved by converging to the virtual target. Assuming that convergence is feasible, the second objective can be achieved by ensuring that the virtual target has an along-track speed which its integral with respect to time is positive. Since the virtual target is constrained by the path, and not necessarily constrained by same dynamical constraints as the actual vehicle, convergence might not be feasible by simply setting a constant positive along track speed. In fact, by setting a constant value, the problem becomes a trajectory-tracking scenario rather than a path-following scenario. Therefore a way of optimizing the along-track speed which enables both convergence and forward motion along the path will now be proposed.

### Proposition

The first step in the following proposition will base around defining a virtual control law in the reference model frame to indirect control the along-track speed of the virtual target. By adopting the reference model control law from (6.4), and inserting the virtual model dynamics in the reference model frame  $\{m\}$  gives the following equation

$$\begin{aligned} \boldsymbol{\tau}_c(\dot{s}) = & \mathbf{g}(\boldsymbol{\eta}_m) - \mathbf{M} \dot{\boldsymbol{v}}_c + \mathbf{D}(\boldsymbol{v}_{ref} - \boldsymbol{v}_c) \\ & - (\mathbf{K}_p \mathbf{J}_\Theta(\boldsymbol{\eta}_m))^\top (\boldsymbol{\eta}_m - \boldsymbol{\eta}_{ref}) + \mathbf{K}_d (\boldsymbol{v}_m - \boldsymbol{v}_{ref}) \end{aligned} \quad (6.42)$$

where

$$\boldsymbol{\eta}_{ref} = \boldsymbol{\eta}_t \quad (6.43)$$

$$\boldsymbol{v}_{ref}(\dot{s}) = \mathbf{J}_\Theta(\tilde{\boldsymbol{\eta}}) \boldsymbol{v}_t(\dot{s}) \quad (6.44)$$

and

$\tilde{\boldsymbol{\eta}} = [0, 0, 0, 0, 0, \psi_t - \psi_m]^\top$   
 $\boldsymbol{v}_t(\dot{s})$  is the virtual target velocity.  
 $\boldsymbol{\eta}_t$  is the virtual target position.  
 $\mathbf{K}_p$  and  $\mathbf{K}_d$  are PD gains.

Now this thesis proposes to optimize the along-track speed  $\dot{s}$ , constrained by the the control law from (6.42), and a set of control input saturation limits. That is

$$\text{maximize } \dot{s} \quad (6.45)$$

$$\text{subject to } \mathbf{u}_{b,min} \leq \mathbf{B}^\dagger \boldsymbol{\tau}_c(\dot{s}) \leq \mathbf{u}_{b,max} \quad (6.46)$$

$$\dot{s}_{min} \leq \dot{s} \leq \dot{s}_{max} \quad (6.47)$$

where

$\mathbf{u}_{b,min}$  and  $\mathbf{u}_{b,max}$  are a set of upper and lower bounds on the control inputs.  
 $\mathbf{B}^\dagger$  is the Moore–Penrose pseudoinverse of the input matrix.  
 $\dot{s}_{min}$  and  $\dot{s}_{max}$  are the bounds on the along-track speed.

Transforming the problem to standard form can be done by first rewriting the problem as

$$\text{minimize } -\dot{s} \quad (6.48)$$

$$\text{subject to } \mathbf{B}^\dagger \boldsymbol{\tau}_c(\dot{s}) - \mathbf{u}_{b,max} \leq 0 \quad (6.49)$$

$$-\mathbf{B}^\dagger \boldsymbol{\tau}_c(\dot{s}) + \mathbf{u}_{b,min} \leq 0 \quad (6.50)$$

$$\dot{s}_{min} - \dot{s} \leq 0 \quad (6.51)$$

$$\dot{s} - \dot{s}_{max} \leq 0 \quad (6.52)$$

and then introducing the standard functions for a nonlinear program as such

$$\text{minimize } f(x) \quad (6.53)$$

$$\text{subject to } g_i(x) \leq 0 \text{ for } i \in \{1, 2, 3, 4\} \quad (6.54)$$

where

$$\begin{aligned} f(x) &:= -x \\ g_1(x) &:= \mathbf{B}^\dagger \boldsymbol{\tau}_c(x) - \mathbf{u}_{b,max} \\ g_2(x) &:= -\mathbf{B}^\dagger \boldsymbol{\tau}_c(x) + \mathbf{u}_{b,min} \\ g_3(x) &:= \dot{s}_{min} - x \\ g_4(x) &:= x - \dot{s}_{max} \end{aligned}$$

**Remark 9** *Since the virtual target velocity is linear in the along-track speed (see 6.40 and 6.41), the optimization program can presumably be defined as a Linear Program (LP) if desirable.*

There are two main outcomes from this optimization program. The first is that no solution can be found. This means that no along-track speed can be found which can guarantee the desired asymptotic convergence specified by the PD gains. For this outcome the along-track speed will be set to zero until the reference model has converged to the point in which the optimization program becomes feasible again. The second outcome is that the optimization program finds the greatest along-track speed which also renders the control law feasible. This means that the virtual target will start to move with a speed that is also considered to secure the specified rate of convergence. The specific rate of convergence can be designed by specifying the natural frequency of the PD control law, and will in large part determine the path following behavior of the vehicle. This will be demonstrated in the case study to come.

Finally the virtual target will also be given some additional along-track dynamics that are expected to improve the path-following performance. To avoid discontinuous along-track speeds, and fully start-stop maneuvers, the following low-pass filter will be included on the along-track speed

$$\dot{s} = \frac{1}{1 + Ts} \dot{s}_d \quad (6.55)$$

where

$\dot{s}$  is the actual along-track speed.

$\dot{s}_d$  is the desired along-track speed provided by the optimization program.

$T$  is the time constant of the low-pass filter.

#### 6.2.4 Case Study: 3D path following using Beluga NTNU

In this case study the path-following controller will be demonstrated together with the reference model from Section 6.1. Therefore the parameters for the reference model will directly be borrowed from that section. The paths to be considered will be the same  $G^0$  and  $G^1$  paths from Figure 6.4 and 6.5, respectively. In addition a point to be inspected will be defined at  $(-6, 3, 4)$ , to demonstrate the different heading dependencies. The specific path-following mission, and the two different zones of heading angle dependence, is illustrated in Figure 6.9.

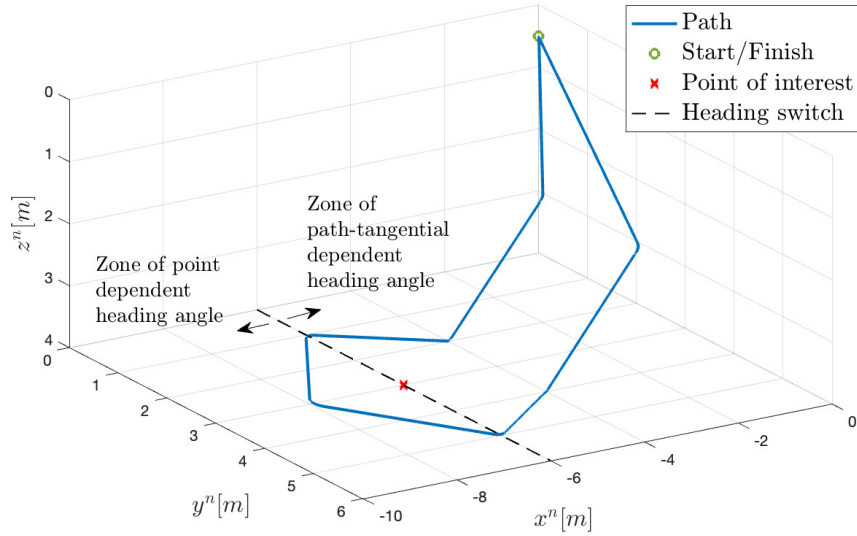


**Figure 6.9:** Illustration of the path following mission

Now the parameters for the path-following controller are to be determined. First is the saturation limits for the along-track speed. These bounds should be placed within the regime of low-speed maneuver, and ideally in accordance with the curvature of the path (see 6.25). For this case study the curvature will however be ignored, and the saturation limits will be chosen as the following constant values

$$\dot{s}_{min} = -0.25 \quad (6.56)$$

$$\dot{s}_{max} = 0.25 \quad (6.57)$$

The control input saturation limits for the virtual control law will be chosen as the same as what was used in the reference model (6.13). Consequently

$$\mathbf{u}_b \in [-5.25, 5.25] \quad (6.58)$$

The PD gains will allegedly determine the rate of convergence that is necessary before positive along track speed is allowed. It can for instance be desired to secure fast convergence of the heading angle such that the vehicle limits its velocity in sway during path-tangential dependent heading, and performs precise heading tracking during point dependent heading. Therefore the required convergence for the heading angle will be set higher than for the linear degrees of freedom. The PD gains will again be designed using the PID-pole placement algorithm in 1, where the relative damping ratios is set equal to one. This way the only tunable parameter is the desired natural frequency virtual control law response.



The optimization program of (6.53-6.54) will be solved using the nonlinear solver *scipy.optimize.minimize*, which its documentation can be found at <https://docs.scipy.org/doc/scipy/reference/generated/scipy.optimize.minimize.html>.

Figure 6.10 and 6.11 shows the trajectory of the reference model using two different sets of design natural frequencies for virtual control law. As one can tell, a greater required rate of convergence gives more precise, but slow path following performance, and opposite otherwise. Both the previous figures applied the control law on the straight line path. Comparing Figure 6.11 and 6.12 it is possible to observe the effects of using curved path segments at the vertices. It is difficult to see any significant differences in the path following precision for the two cases. However the time span of operation using curved path segments can be seen to be approximately 14% faster.

### Conclusion of the case study

In this case study a novel path-following controller was designed to optimize the along-track speed of a virtual target to also consider vehicle dynamics and actuator constraints. The solution was based on designing a control law in the frame of the reference model with the intention of controlling the the motion of the virtual. The designing the desired convergence rate for the controller have been shown to balance for the property of path following precision vs. speed. Also choosing different saturation limits for the along-track speed is can expected to affect the path following behavior. Hence Research Question R2 have been validated. Recommendations for further work is online tuning of some of these parameters. Since the controller is guiding the reference model, it is in fact possible to simulate several time steps ahead which enables evaluation of different variations of parameters for some metric. For instance can the error dynamics at vertices be improved by simulation ahead, and choosing the parameters that minimizes e.g. the path error or energy consumption.

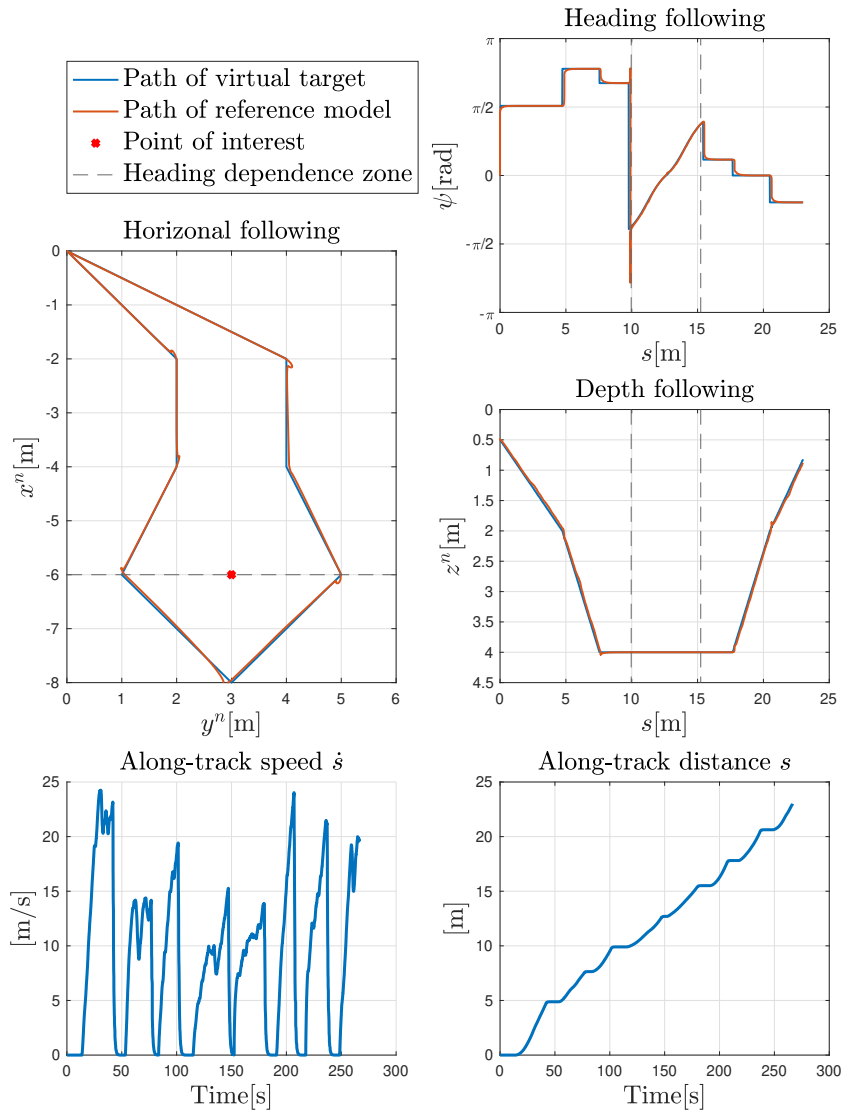


Figure 6.10:  $G^0$  path following using  $\omega_b = [1.0, 1.0, 1.0, 0.0, 0.0, 2.0]$

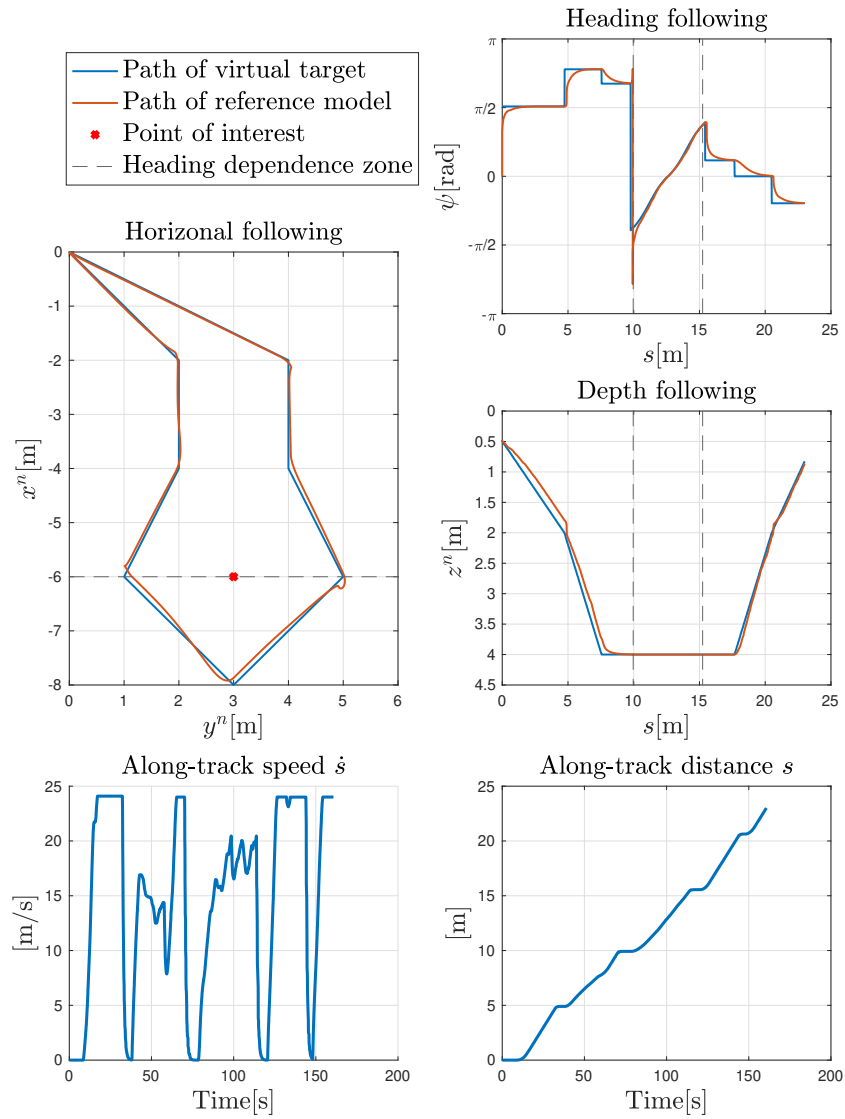


Figure 6.11:  $G^0$  path following using  $\omega_b = [0.5, 0.5, 0.5, 0.0, 0.0, 1.0]$

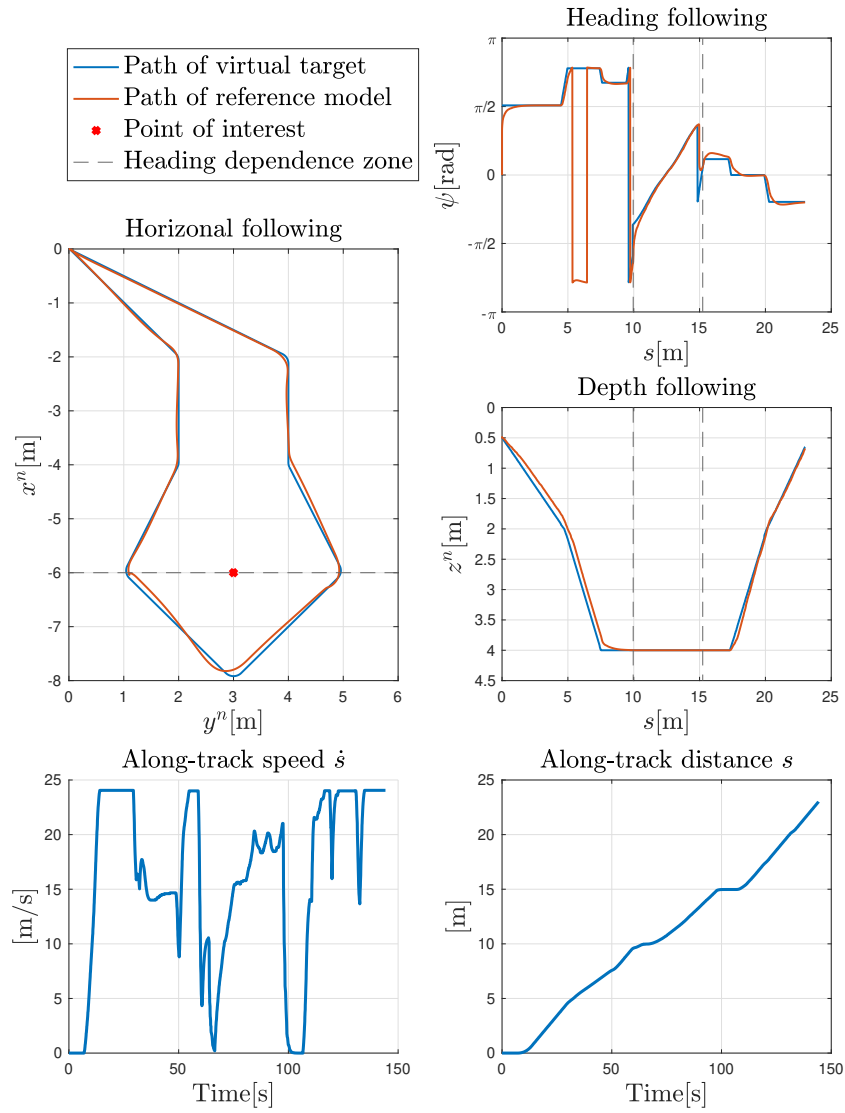


Figure 6.12:  $G^1$  path following result using  $\omega_b = [0.5, 0.5, 0.5, 0.0, 0.0, 1.0]$

## Chapter 7

# Case Study: Simulation of the Guidance and Control System

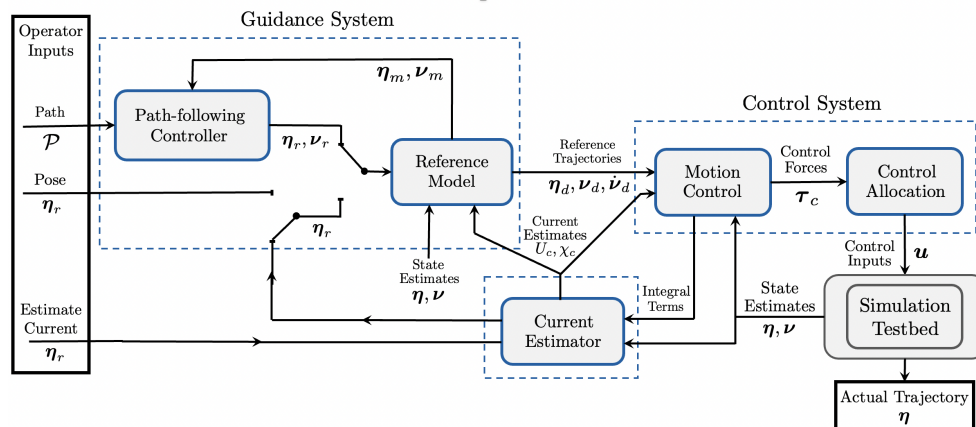


Figure 7.1: Illustration of the final guidance and control system architecture

Now the entirety of the guidance and control system will be simulated from operator inputs to output trajectory, as illustrated in Figure 7.1. A description of the simulation setup and mission objectives will be provided in Section 7.1. In Section 7.2 the simulation results are presented, and thereafter concluded in Section 7.3.

### 7.1 Simulation Setup and Parameters

All the sub modules shown in Figure 7.1 partly rely its parameters on the model parameters of the vehicle. However it is rarely possible to perfectly model a vehicle without including some degree of modelling error. Therefore this case study will simulate some parametric and structural disturbances by using different parameters for the guidance and control system and the UUV Simulator. The model

parametric differences to be included are shown in detail in Appendix B. This section will now only consider described the design parameters that are not exclusively model dependent. This means that the remaining parameters relying on the vehicle model will extract its values in accordance with the provided appendix.

### UUV Simulator

In this case study the UUV Simulator from Section 4, will be provided with a different set of model parameters than the rest of the system. The model differences will include both parametric and structural disturbances are described in detail in Appendix B. The parameters of the ocean currents are shown in Table 7.1.

**Table 7.1:** The parameters of the UUV Simulator

Notation	Value	Design Description
$U_c$	0.2	The amplitude velocity of the horizontal ocean current
$\chi_c$	$\pi/8$	The course angle of the horizontal ocean current

### Control allocation

The control allocation system from 5.1, requires a thruster configuration to compute its input matrix. This is only dependent on the vehicle model. The only design parameter for the module to optimize the control force error is the weight matrix for the control forces. This leaves the control allocation with a single parameter as shown in Table 7.2.

**Table 7.2:** The design parameters of control allocation system

Notation	Value	Design Description
$W$	$[0.1, 0.1, 0.1, 100, 100, 1]^T$	Priority weights on the control forces

### Motion control

The motion control system from Section 5.2, requires a set control bandwidths and relative damping ratios to design the closed-loop response of the system. The remaining parameters are purely based on the vehicle model, hence the only design parameters for the motion control system are given in Table 7.3.

### Ocean current estimator

The Ocean Current Estimator from Section 5.3, acquires the hydrodynamic damping parameters for surge and sway. The number of estimates and change in heading angle can however be regarded as design parameters. For sake of example,

**Table 7.3:** The design parameters of the motion control system

Notation	Value	Design Description
$\omega_b$	$[0.6, 0.6, 0.6, 0, 0, 0.6]^T$	Control bandwidths for surge, sway, heave and yaw.
$\zeta$	$[1, 1, 1, 0, 0, 1]^T$	Relative damping ratios for surge, sway, heave and yaw.

three samples will be desired, where the final estimate is chosen as the mean of the three samples. Further, the estimator appeared to provide quite stable and precise estimates for the maximum change in heading angle. Consequently the design parameters of the current estimator is chosen according to Table 7.4.

**Table 7.4:** The design parameters of the current estimator

Notation	Value	Design Description
$\Delta\psi$	$\pi$	Change in heading angle
N	3	Number of estimate samples

## Reference model

The reference model from Section 6.1 heavily depends its parameters on the vehicle model. The remaining design parameters are somewhat dependent on the parameters of the motion control system, as well as the thruster dynamics. The design choice of these parameters are given in Table 7.5.

**Table 7.5:** The design parameters of the reference model

Notation	Value	Design Description
$\omega_b$	$[0.3, 0.3, 0.3, 0, 0, 0.3]^T$	Control bandwidths for surge, sway, heave and yaw (chosen as half of the motion control bandwidths)
$\zeta$	$[1, 1, 1, 0, 0, 1]^T$	Relative damping ratios for surge, sway, heave and yaw
$W$	$[0.1, 0.1, 0.1, 100, 100, 1]^T$	Priority weights on the control forces
$[u_{min}, u_{max}]$	$[-5.25, 5.25]$	Control input saturation limits (chosen as half of the modelled values)
$T$	0.4	First-order time constant of the low-pass filtered control forces (chosen as double of the modelled value)

### Path-following controller

The path-following controller from Section 6.2.3 also includes model parameters in the control design. Table 7.6 gives an overview of the remaining tunable design parameters and their design values.

**Table 7.6:** The design parameters of the path-following controller

Notation	Value	Design Description
$\omega$	$[0.75, 0.75, 0.75, 0, 0, 1.5]^T$	Virtual controller bandwidths (Tuning parameters for precision vs. speed)
$[u_{min}, u_{max}]$	$[-5.25, 5.25]$	Control input saturation limits (chosen similar to the values in the reference model)
$[\dot{s}_{min}, \dot{s}_{max}]$	$[-0.2, 0.2]$	Along-track speed saturation limits (should ideally be tuned in accordance with low-speed maneuvering, path curvature and specific application)
$T$		First-order time constant for the low-pass filtered along-track speed

### Mission objective and operator inputs

The mission objective will be the same as the path-following mission illustrated in Figure 6.9. However, this time the ocean current are to be estimated pre operation as well. This imposes the following simple operator for completing the mission.

1. Estimate the ocean current at the current pose  $\eta_r \leftarrow \eta$
2. Follow the path  $\mathcal{P}$  (in Figure 6.9)

## 7.2 Simulation Results

Figure 7.2 shows the ocean current estimation performance during the pre phase of the mission. As one can see the the all current estimates have a small offsets in the course angle of the current, which can be expected as the hydrodynamic damping coefficients includes parametric disturbances.

Figure 7.3 shows the resulting trajectory of the vehicle throughout the mission. As one can tell the vehicle tracks the path with a good accuracy and only suffers small deviations at some of the vertices and during the zone where the heading angle is point dependent.



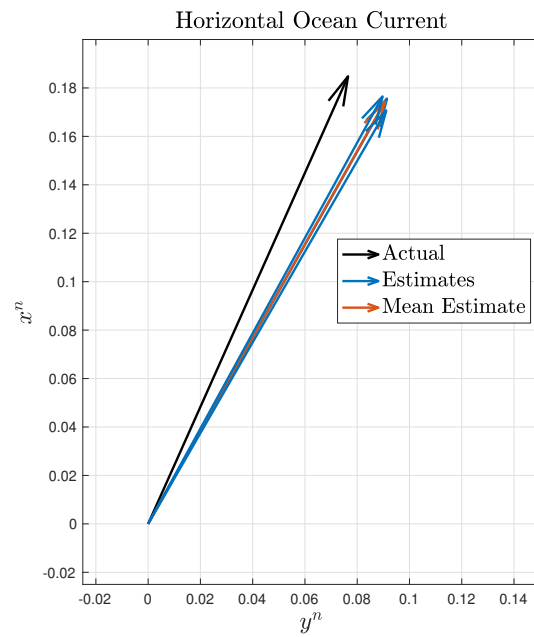


Figure 7.2: The resulting ocean current estimates

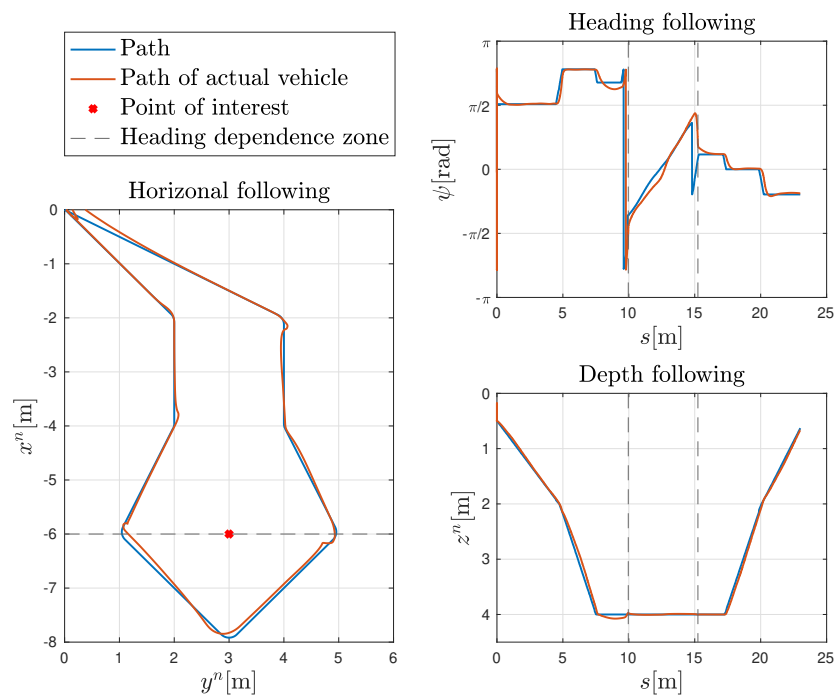


Figure 7.3: The resulting path following performance

### 7.3 Conclusion of Case Study

In this case study the entirety of the guidance and control systems considered in this thesis have been verified by computer simulation. Parametric and structural disturbances have been included, in addition to unknown ocean currents which were to be estimated. All parameters independent on the model parameters have been accounted for and described, resulting in few design parameters which all could show to intuitive properties. The current estimations were of by a small margin, to be expected considering the parametric disturbances in the hydrodynamic damping terms and actuator model. The resulting path following performance was reasonable accurate without any unexpected behaviors. Consequently, Research Question **R3** is verified, and the guidance and control system is presumably easy to adopt for fully-actuated underwater vehicles using thrusters, and with a known dynamic model consistent with a diagonal structure.

## Chapter 8

# Conclusions and Recommendation for Further Work

This chapter contains conclusions of the work of this thesis in Section 8.1, followed by recommendations for further work in Section 8.2.

### 8.1 Conclusions

This thesis addresses different modules for guidance and control system for dynamic positioning and 3D path following for a fully actuated AUV exposed to unknown ocean currents. In order to guide the thesis towards further development, particularly three research questions were formulated.

- R1** Is it possible to use steady-state integral action terms, and changes in the orientation of the vehicle, to estimate the ocean current velocity invariant of additional non-current modelling errors.

In the light of the first research question, a novel method of estimating the horizontal ocean current parameters using the hydrodynamic parameters of the vehicle, and sampling steady state integral action terms for different values of heading angle, was proposed. The method was tested in computer simulations and provided accurate estimates under some assumptions about the non-current modelling errors and constant irrotational ocean currents. The results suggest that it is possible to estimate this type of ocean current using this method, and therefore reveal a great potential for improving motion control systems of fully actuated AUVs in future applications.

- R2** Is it possible to develop a 3D path-following controller to include dynamical constraints for a specific underwater vehicle, as well as to include tuning parameters to advocate for different path following behaviors accordingly.

For the second research question, a novel 3D path following controller was developed. The solution was based on first defining a virtual target to move along the path. Then a model-based DP controller was defined in the reference model point of view to optimize the along track speed under consideration of vehicle and actuator constraints. In addition options for heading angle guidance along the path was presented. The method showed great results by being able to tune the path following behavior through the parameters of the DP-controller. Hence the second research question was successfully answered resulting in an interesting alternative for path-following applications for fully actuated AUVs, to also consider the dynamical limitations of the vehicle.

- R3** Is it possible to develop a guidance and control system where all parameters of the system have intuitive or universal properties, such as using the model parameters of the specific underwater vehicle.

Unlike the two former research questions, the final research question aims at the entirety of the guidance and control system proposed in this thesis. All the proposed modules have been designed by using model parameters of the vehicle extensively, leaving the remaining parameters with intuitive properties. Hence it has been demonstrated that it is possible to minimize parameter complexity and modularity by including the model parameters of the vehicle where it is possible. Whether this approach is sufficient for simplifying the process of parameter testing for a real application is yet to be tested, but it seems likely that this is the case.

## 8.2 Recommendations for Further Work

The systems considered in this thesis have so far only been validated through computer simulations. Even though the final case study included some parametric and structural disturbances, the obvious recommendation is to test the systems in real world experiments. It is in fact it is not a matter of course that the simulation testbed is able to capture the essential parametric and structural properties of the real world. A full scale experiment also requires a navigation system able to provide the sufficient state estimates. As a side note, it seems like research on acoustic communication and SLAM methods are highly relevant to achieve sufficient aiding measurements for the positional state estimates in the horizontal plane. More system specific recommendations for further work are given below.

### **Ocean current estimator**

It would be particularly interesting to validate the current estimator in a real application, since it relies heavily on the complex hydrodynamics of the vehicle. It is also difficult to tell whether the assumptions of the non-current modelling errors being constant in the body frame are viable. Hence real world experiments are valuable, especially if the estimator proves to perform well for real applications as well. It can also be interesting to extend the method to estimate the vertical current component as well. This can presumably be done by analyzing steady-state integral action terms for changes in roll or pitch.

### **Path-following controller**

In this thesis the design parameters to decide on the path following behavior was chosen as constant values. However, it can be interesting to look into the possibilities of adapting the path following parameters as the vehicle follows the path. Since the path following controller is based on the reference model, it is also possible to simulate ahead and evaluate the path following performance to choose the parameters that yields the best result. It is also possible to look into the advantages of including the acceleration dynamics of the virtual controller in the control design.

### **The overall guidance and control system**

The overall guidance and control system can also be further developed. Modules for path planning and obstacle avoidance are essential for improved efficiency and reducing risk during autonomous operations. Both the reference model and path following controller considered in this thesis can be used as tools in these kinds of systems.



# Bibliography

- [1] S. Petillo and H. Schmidt, 'Exploiting adaptive and collaborative auv autonomy for detection and characterization of internal waves,' *IEEE Journal of Oceanic Engineering*, vol. 39, no. 1, pp. 150–164, 2014. DOI: [10.1109/JOE.2013.2243251](https://doi.org/10.1109/JOE.2013.2243251).
- [2] P. Ridao, M. Carreras, D. Ribas, P. J. Sanz and G. Oliver, 'Intervention auvs: The next challenge,' *Annual Reviews in Control*, vol. 40, pp. 227–241, 2015, ISSN: 1367-5788. DOI: <https://doi.org/10.1016/j.arcontrol.2015.09.015>. [Online]. Available: <https://www.sciencedirect.com/science/article/pii/S1367578815000541>.
- [3] T. I. Fossen, *Handbook of marine craft hydrodynamics and motion control, 2nd edition*. John Wiley & Sons, 2021.
- [4] B. Allen, R. Stokey, T. Austin, N. Forrester, R. Goldsborough, M. Purcell and C. von Alt, 'Remus: A small, low cost auv; system description, field trials and performance results,' in *Oceans '97. MTS/IEEE Conference Proceedings*, vol. 2, 1997, 994–1000 vol.2. DOI: [10.1109/OCEANS.1997.624126](https://doi.org/10.1109/OCEANS.1997.624126).
- [5] T. Fossen, T. Johansen and P. Tristan, 'A survey of control allocation methods for underwater vehicles,' in. Jan. 2009, ISBN: 978-953-7619-49-7. DOI: [10.5772/6699](https://doi.org/10.5772/6699).
- [6] J. Kinsey, R. Eustice and L. Whitcomb, 'A survey of underwater vehicle navigation: Recent advances and new challenges,' Jan. 2006.
- [7] T. Johansen and T. Fossen, 'Control allocation - a survey,' *Autom.*, vol. 49, pp. 1087–1103, 2013.
- [8] M. Breivik and T. Fossen, 'Guidance laws for autonomous underwater vehicles,' in. Jan. 2009, ISBN: 978-953-7619-49-7. DOI: [10.5772/6696](https://doi.org/10.5772/6696).
- [9] A. J. Sørensen, 'A survey of dynamic positioning control systems,' *Annual Reviews in Control*, vol. 35, no. 1, pp. 123–136, 2011, ISSN: 1367-5788. DOI: <https://doi.org/10.1016/j.arcontrol.2011.03.008>. [Online]. Available: <https://www.sciencedirect.com/science/article/pii/S1367578811000095>.

- [10] M. Abdellatif, O. Rashed, S. Shaaban and A. Abdulaziz, 'Online ocean current estimation and mapping for autonomous underwater vehicle,' Sep. 2018.
- [11] P. Encarnacao, A. Pascoal and M. Arcaç, 'Path following for autonomous marine craft,' *IFAC Proceedings Volumes*, vol. 33, no. 21, pp. 117–122, 2000.
- [12] P. Encarnação, A. Pascoal and M. Arcaç, 'Path following for marine vehicles in the presence of unknown currents,' *IFAC Proceedings Volumes*, vol. 33, no. 27, pp. 507–512, 2000.
- [13] L. Lapierre and D. Soetanto, 'Nonlinear path-following control of an auv,' *Ocean engineering*, vol. 34, no. 11-12, pp. 1734–1744, 2007.
- [14] A. Zolich, D. Palma, K. Kansanen, K. Fjørtoft, J. Sousa, K. H. Johansson, Y. Jiang, H. Dong and T. A. Johansen, 'Survey on communication and networks for autonomous marine systems,' *Journal of Intelligent & Robotic Systems*, vol. 95, no. 3-4, pp. 789–813, 2019.
- [15] D. R. Yoerger, J. G. Cooke and J.-J. Slotine, 'The influence of thruster dynamics on underwater vehicle behavior and their incorporation into control system design,' *IEEE Journal of Oceanic Engineering*, vol. 15, no. 3, pp. 167–178, 1990.
- [16] M. Quigley, K. Conley, B. Gerkey, J. Faust, T. Foote, J. Leibs, R. Wheeler and A. Y. Ng, 'Ros: An open-source robot operating system,' in *ICRA workshop on open source software*, Kobe, Japan, vol. 3, 2009, p. 5.
- [17] *Ros documentation*, <http://wiki.ros.org/Documentation>, Accessed: 2021-01-25.
- [18] M. M. M. Manhães, S. A. Scherer, M. Voss, L. R. Douat and T. Rauschenbach, 'Uuv simulator: A gazebo-based package for underwater intervention and multi-robot simulation,' in *OCEANS 2016 MTS/IEEE Monterey*, 2016, pp. 1–8. DOI: [10.1109/OCEANS.2016.7761080](https://doi.org/10.1109/OCEANS.2016.7761080).
- [19] N. Koenig and A. Howard, 'Design and use paradigms for gazebo, an open-source multi-robot simulator,' in *2004 IEEE/RSJ International Conference on Intelligent Robots and Systems (IROS) (IEEE Cat. No.04CH37566)*, vol. 3, 2004, 2149–2154 vol.3. DOI: [10.1109/IROS.2004.1389727](https://doi.org/10.1109/IROS.2004.1389727).
- [20] R. Panish and M. Taylor, 'Achieving high navigation accuracy using inertial navigation systems in autonomous underwater vehicles,' *OCEANS 2011 IEEE - Spain*, pp. 1–7, 2011.
- [21] L. Paull, S. Saeedi, M. Seto and H. Li, 'Auv navigation and localization: A review,' *IEEE Journal of Oceanic Engineering*, vol. 39, no. 1, pp. 131–149, 2014. DOI: [10.1109/JOE.2013.2278891](https://doi.org/10.1109/JOE.2013.2278891).
- [22] A. Lekkas, A. R. Dahl, M. Breivik and T. Fossen, 'Continuous-curvature path generation using fermat's spiral,' *Modeling, Identification and Control (MIC)*, vol. 34, pp. 183–198, Oct. 2013. DOI: [10.4173/mic.2013.4.3](https://doi.org/10.4173/mic.2013.4.3).



- [23] M. Breivik and T. Fossen, 'Guidance laws for autonomous underwater vehicles,' in. Jan. 2009, ISBN: 978-953-7619-49-7. DOI: [10.5772/6696](https://doi.org/10.5772/6696).
- [24] A. Tsourdos, B. White and M. Shanmugavel, 'Cooperative path planning of unmanned aerial vehicles,' 2010.
- [25] A. Lekkas and T. Fossen, 'Line-of-sight guidance for path following of marine vehicles,' in. Jun. 2013, ISBN: 978-3659416897.
- [26] *T200 thruster*, <https://bluerobotics.com/store/thrusters/t100-t200-thrusters/t200-thruster-r2-rp/>, [Accessed: 12.03.2021].
- [27] *Scipy.optimize.minimize*, <https://docs.scipy.org/doc/scipy/reference/generated/scipy.optimize.minimize.html>, [Accessed: 08.05.2021], 2021.



## Appendix A

# Beluga NTNU Parameters

### Model Parameters

$$m = 25.4 [kg] \quad \nabla = 0.027 [m^3]$$

$$\mathbf{r}_{bg}^b = [0, 0, 0]^T [m] \quad \mathbf{r}_{bb}^b = [0, 0, -0.026]^T [m]$$

$$\mathbf{I}_g^b = \begin{bmatrix} 0.5 & 0 & 0 \\ 0 & 1.1 & 0 \\ 0 & 0 & 1.2 \end{bmatrix}$$

$$\mathbf{M}_A = - \begin{bmatrix} -20.0 & 0 & 0 & 0 & 0 & 0 \\ 0 & -40.0 & 0 & 0 & 0 & 0 \\ 0 & 0 & -50.0 & 0 & 0 & 0 \\ 0 & 0 & 0 & -0.5 & 0 & 0 \\ 0 & 0 & 0 & 0 & -2.0 & 0 \\ 0 & 0 & 0 & 0 & 0 & -2.0 \end{bmatrix}$$

$$\mathbf{D} = - \begin{bmatrix} -20.0 & 0 & 0 & 0 & 0 & 0 \\ 0 & -40.0 & 0 & 0 & 0 & 0 \\ 0 & 0 & -50.0 & 0 & 0 & 0 \\ 0 & 0 & 0 & -3.0 & 0 & 0 \\ 0 & 0 & 0 & 0 & -10.0 & 0 \\ 0 & 0 & 0 & 0 & 0 & -10.0 \end{bmatrix}$$

### Thruster Parameters

**Table A.1:** Thruster locations of Beluga NTNU w.r.t. the BODY frame.

Thruster nr.	$\mathbf{p}_{bt_i}^b$ [m]	$\Theta_{bt_i}$ [rad]
0	$[0.238, 0.220, -0.065]^\top$	$[0, 0, \frac{3\pi}{4}]^\top$
1	$[0.120, 0.220, -0.065]^\top$	$[0, \pi, 0]^\top$
2	$[-0.120, 0.220, -0.065]^\top$	$[0, \pi, 0]^\top$
3	$[-0.240, 0.220, -0.065]^\top$	$[0, 0, \frac{\pi}{4}]^\top$
4	$[-0.240, -0.220, -0.065]^\top$	$[0, 0, -\frac{\pi}{4}]^\top$
5	$[-0.120, -0.220, -0.065]^\top$	$[0, \pi, 0]^\top$
6	$[0.120, -0.220, -0.065]^\top$	$[0, \pi, 0]^\top$
7	$[0.238, -0.220, -0.065]^\top$	$[0, 0, -\frac{3\pi}{4}]^\top$

$$T_{|n|n} = 0.00000364$$

$$T = 0.2$$

$$u \in [-10.5, 10.5]$$

## Appendix B

# Model Parametric Differences for the Case Study in Section 7

This Appendix shows the parametric differences that are included in the computer simulations for the case study done in Section 7. Parameters marked in black are used in the design of the guidance and control system, while adjusted parameters with red are used in the ground truth UUV Simulator. An example of this is given in Table B.1. All parameters regarding distance are given a random offset of  $\pm 1$  cm, and all coefficients are given a random offset of  $\pm 10$  %. The mass, the volume of displaced fluid are presumably easy to measure, hence they are only given small offsets.

**Table B.1:** Representation of model parametric differences

Parameter representation	Parameter used in the GNC design	Actual parameter used for simulating the vehicle
2.0 +0.1	2.0	2.1
2.0 ·0.9	2.0	1.8

### Model Parameters

$$m = 25.4|+0.01 \text{ [kg]} \quad \nabla = 0.025|+0.002 \text{ [m}^3\text{]}$$

$$\mathbf{r}_{bg}^b = [0|+0.01, 0|+0.01, 0|+0.01]^\top \text{ [m]} \quad \mathbf{r}_{bb}^b = [0|+0.01, 0|+0.01, -0.01|+0.01]^\top \text{ [m]}$$

$$\mathbf{I}_g^b = \begin{bmatrix} 0.5|+0.1 & 0|+0.1 & 0|+0.1 \\ 0|+0.1 & 1.1|+0.1 & 0|+0.1 \\ 0|+0.1 & 0|+0.1 & 1.2|+0.1 \end{bmatrix}$$

$$M_A = - \begin{bmatrix} -20.0| \cdot 1.1 & 0 & 0 & 0 & 0 & 0 \\ 0 & -40.0| \cdot 0.9 & 0 & 0 & 0 & 0 \\ 0 & 0 & -50.0| \cdot 0.9 & 0 & 0 & 0 \\ 0 & 0 & 0 & -0.5| \cdot 0.9 & 0 & 0 \\ 0 & 0 & 0 & 0 & -2.0| \cdot 1.1 & 0 \\ 0 & 0 & 0 & 0 & 0 & -2.0| \cdot 0.9 \end{bmatrix}$$

$$D = - \begin{bmatrix} -20.0| \cdot 0.9 & 0 & 0 & 0 & 0 & 0 \\ 0 & -40.0| \cdot 1.1 & 0 & 0 & 0 & 0 \\ 0 & 0 & -50.0| \cdot 0.9 & 0 & 0 & 0 \\ 0 & 0 & 0 & -3.0| \cdot 1.1 & 0 & 0 \\ 0 & 0 & 0 & 0 & -10.0| \cdot 1.1 & 0 \\ 0 & 0 & 0 & 0 & 0 & -10.0| \cdot 0.9 \end{bmatrix}$$

$$D_N(\mathbf{v}_r) = - \begin{bmatrix} (0| -5.0)| u_r & 0 & 0 & 0 & 0 & 0 \\ 0 & (0| -10.0)| v_r & 0 & 0 & 0 & 0 \\ 0 & 0 & (0| -10.0)| w_r & 0 & 0 & 0 \\ 0 & 0 & 0 & 0 & 0 & 0 \\ 0 & 0 & 0 & 0 & 0 & 0 \\ 0 & 0 & 0 & 0 & 0 & 0 \end{bmatrix}$$

### Thruster Parameters

Table B.2: Thruster locations w.r.t. the BODY frame.

i	$\mathbf{p}_{bt_i}^b$ [m]	$\Theta_{bt_i}$ [rad]
0	$[0.238  -0.01, 0.220  -0.01, -0.065  +0.01]^\top$	$[0, 0  +0.2, \frac{3\pi}{4}  +0.2]^\top$
1	$[0.120  +0.01, 0.220  +0.01, -0.065  -0.01]^\top$	$[0, \pi  +0.2, 0  +0.2]^\top$
2	$[-0.120  +0.01, 0.220  -0.01, -0.065  -0.01]^\top$	$[0, \pi  -0.2, 0  -0.2]^\top$
3	$[-0.240  -0.01, 0.220  -0.01, -0.065  +0.01]^\top$	$[0, 0  -0.2, \frac{\pi}{4}  -0.2]^\top$
4	$[-0.240  +0.01, -0.220  -0.01, -0.065  +0.01]^\top$	$[0, 0  -0.2, -\frac{\pi}{4}  +0.2]^\top$
5	$[-0.120  -0.01, -0.220  +0.01, -0.065  -0.01]^\top$	$[0, \pi  +0.2, 0  +0.2]^\top$
6	$[0.120  +0.01, -0.220  +0.01, -0.065  +0.01]^\top$	$[0, \pi  -0.2, 0  -0.2]^\top$
7	$[0.238  -0.01, -0.220  +0.01, -0.065  +0.01]^\top$	$[0, 0  +0.2, -\frac{3\pi}{4}  +0.2]^\top$

$$T_{|n|n} = 0.00000364| \cdot 0.9$$

$$T = 0.2| +0.5$$

$$u \in [-10.5| \cdot 0.9, 10.5| \cdot 0.9]$$

## **Appendix C**

# **Master's Thesis Project Description**



## MASTER'S THESIS PROJECT DESCRIPTION

**Name:** Aksel Kristoffersen  
**Department:** Engineering Cybernetics  
**Thesis title:** Guidance and Control System for Dynamic Positioning and Path Following of an AUV exposed to Ocean Currents

### Thesis Description:

The main purpose of the project is to develop a model-based guidance and control system for a fully actuated low-speed maneuvering autonomous underwater vehicle (AUV) exposed to constant irrotational ocean currents. This includes modules for motion control, reference models and path-following control in 3D.

The following topics and challenges should be considered in more detail:

1. Literature study on dynamic positioning and path-following control. Appropriate research questions and requirement specifications should be formulated in order to solve the problem.
2. Model a low-level actuator control system and include the model in the UUV simulator by Marcusso et al. (2016).
3. Develop a method for estimating ocean currents to improve the performance of the guidance and control systems.
4. Develop control algorithms for dynamic positioning and 3D path following including ocean current estimates.
5. Simulate the guidance and control system and conclude your findings.

**Thesis performed at:** Department of Engineering Cybernetics, NTNU  
**Supervisor:** Professor Thor I. Fossen, Dept. of Eng. Cybernetics, NTNU



